



**REVIEW**

# Hysteresis-Loop Criticality in Disordered Ferromagnets—A Comprehensive Review of Computational Techniques

Djordje Spasojević<sup>1,\*</sup>, Sanja Janičević<sup>2</sup>, Svetislav Mijatović<sup>1</sup> and Bosiljka Tadić<sup>3,4</sup>

<sup>1</sup>Faculty of Physics, University of Belgrade, Belgrade, 11001, Serbia

<sup>2</sup>Faculty of Science, University of Kragujevac, Kragujevac, 34000, Serbia

<sup>3</sup>Department for Theoretical Physics, Jožef Stefan Institute, Ljubljana, SI-1001, Slovenia

<sup>4</sup>Complexity Science Hub, Josephstaedterstrasse 39, Vienna, 1080, Austria

\*Corresponding Author: Djordje Spasojević. Email: djordjes@ff.bg.ac.rs

Received: 30 August 2024 Accepted: 18 November 2024 Published: 27 January 2025

## ABSTRACT

Disordered ferromagnets with a domain structure that exhibit a hysteresis loop when driven by the external magnetic field are essential materials for modern technological applications. Therefore, the understanding and potential for controlling the hysteresis phenomenon in these materials, especially concerning the disorder-induced critical behavior on the hysteresis loop, have attracted significant experimental, theoretical, and numerical research efforts. We review the challenges of the numerical modeling of physical phenomena behind the hysteresis loop critical behavior in disordered ferromagnetic systems related to the non-equilibrium stochastic dynamics of domain walls driven by external fields. Specifically, using the extended Random Field Ising Model, we present different simulation approaches and advanced numerical techniques that adequately describe the hysteresis loop shapes and the collective nature of the magnetization fluctuations associated with the criticality of the hysteresis loop for different sample shapes and varied parameters of disorder and rate of change of the external field, as well as the influence of thermal fluctuations and demagnetizing fields. The studied examples demonstrate how these numerical approaches reveal new physical insights, providing quantitative measures of pertinent variables extracted from the systems' simulated or experimentally measured Barkhausen noise signals. The described computational techniques using inherent scale-invariance can be applied to the analysis of various complex systems, both quantum and classical, exhibiting non-equilibrium dynamical critical point or self-organized criticality.

## KEYWORDS

Disordered ferromagnets; hysteresis-loop criticality; magnetization-reversal avalanches in simulations and experiments; zero-temperature and thermal Random Field Ising Model simulations; computational techniques for multiparameter scaling analysis; multifractal Barkhausen noise; finite driving rates; demagnetizing effects; nonequilibrium critical dynamics

## Nomenclature

$L$	Linear lattice size
$l$	Thickness



$d$	Dimensionality
$R$	Disorder
$R_c$	Critical disorder
$R_c^{\text{eff}}$	The effective critical disorder
$r$	Reduced disorder, $r = (R - R_c)/R$
$H$	External magnetic field
$H_c$	Critical magnetic field
$H_c^{\text{eff}}$	The effective critical magnetic field
$h$	Reduced magnetic field
$h_i$	Random magnetic field
$\rho(h_i)$	Distribution of random magnetic field
$h_i^{\text{eff}}$	Local effective magnetic field
$s_i$	Spin at a lattice site $i$
$z_{nn}$	Lattice coordination number
$\mathcal{H}$	Hamiltonian
$\Theta$	Temperature
$c$	Fraction of thermally flippable spins
$\Omega$	Driving rate
$J_{ij}, J$	Exchange coupling constant
$J_{\text{dipole}}$	Dipole-dipole interaction constant
$J_D$	Demagnetizing coefficient
$t$	Time
$V(t)$	Response signal
$V_{\text{th}}$	Threshold imposed on $V(t)$
$M$	Magnetization
$M_c$	Critical magnetization
$M_c^{\text{eff}}$	Effective critical magnetization
$\chi$	Susceptibility
$X = S, T, E, A$	$X =$ size $S$ , duration $T$ , energy $E$ , amplitude $A$
$D_X^{(\text{int})}(X)$	Integrated distribution of avalanche parameter $X$
$D_X^{(\text{w})}(X)$	Windowed distribution of avalanche parameter $X$
$\tau, \alpha, \varepsilon, \mu, \nu, \eta, \zeta$	RFIM critical exponents
$\sigma, \beta, \gamma_{x/y}, \delta, \theta, z, \phi$	RFIM critical exponents (cont.)
$T_w$	Waiting time
$P(f)$	Power spectrum density at frequency $f$
$G_R(x)$	Correlation function at inter-spin distance $x$
$\xi$	Correlation length
$D_f$	Fractal dimension
$H_q$	Generalized Hurst exponent
$F_q$	Fluctuation function
erfc	The complementary error function $\text{erfc}(x) = (2/\sqrt{\pi}) \int_x^\infty e^{-t^2} dt$

### Acronyms

<i>RFIM</i>	Random Field Ising Model
<i>NEQ</i>	Nonequilibrium
<i>EQ</i>	Equilibrium

<i>ZT</i>	Zero-temperature
<i>BHN</i>	Barkhausen noise
<i>HL</i>	Hysteresis loop
<i>HLC</i>	Central part of the hysteresis loop
<i>RFC</i>	Random field configuration
<i>AE</i>	Activity event
<i>FDR</i>	Finite-driving rate
<i>MFR</i>	Multifractality
<i>AAS</i>	Average avalanche shape
<i>UWN</i>	Uniform white noise
<i>GWN</i>	Gaussian white noise

## 1 Introduction

Disordered ferromagnetic materials are the subject of intense theoretical and experimental research due to their physical characteristics associated with the domain structure [1–3]. Recent research surveys [4–7] elucidate that these materials, especially low dimensional samples and ferromagnetic-antiferromagnetic heterostructures, are considered promising materials for modern technology applications. Disordered ferromagnets possess intricate domain structure leading to the hysteresis behavior [8,9] in the external magnetic field; see also recent review [10] and references therein. Hysteresis behavior is vital for various applications of magnetic materials [11]. Therefore more attention is devoted to predicting and optimizing hysteresis properties using different numerical tools [12]. During the reversal processes by slow ramping of the external field over the hysteresis loop, the moving domain walls interact with the structural and magnetic disorder [13], leading to stochastic changes of the magnetization. The magnetization fluctuations are experimentally measured as Barkhausen noise (BHN), for example, in bulk materials [14–17] and thin films [18–21], as well as in samples with varied thickness [22,23]. Considering the Ising model, one of central pillars of statistical physics [24], theoretical investigations focusing to the dynamic phenomena on hysteresis use the field-driven spin models with random bond [25] or random field disorder [26–28]. These investigations revealed that the collective nature of the magnetization changes with avalanche-like behavior on the hysteresis are associated with a disorder-induced critical point [29–32].

This out-of-equilibrium critical dynamics is characterized by long-range temporal correlations and multifractal features of the BHN [33]. Among different types of models of disordered systems, the Ising model with random fields [34–37] appeared as the most attractive for theoretical investigations of the in- and out-of-equilibrium criticality. It was also recognized as an appropriate model for weakly disordered antiferromagnetic materials in an external field, where structural disorder induces local random fields [38–40]. For more details regarding recent studies on antiferromagnetic systems, see [41–44]. It should be noted that the 100 years of the Ising model, celebrated this year, have shown its relevance to many different phenomena in complex systems [45]. However, certain limitations of the model in describing the magnetism of solid materials are evident, for example, taking into account more complex domain walls in domain structures that are associated with hysteresis phenomena, distinguishing hysteresis properties along different easy axes and the influence of other types of disorder that do not break the local rotational symmetry. In addition to the theoretical interpretation of the behavior of disordered ferromagnetic systems, using the random-field Ising model in interpreting experimental Barkhausen noise proved crucial for some systems [17,46]. In a more general context, statistical physics and random field theory were recently applied for spatial data modelling, as described in the book [47].

The model treats a system of Ising spins located at lattice sites and quenched impurities interpreted by randomly distributed magnetic fields. Among the nearest neighboring spins the ferromagnetic interaction occurs, in addition to the interaction with the external magnetic and a quenched random field. The zero-temperature variant of the model proposed in [48] captures the essential features of avalanching dynamics while neglecting thermal effects. Triggered by the external magnetic field changes, the system relaxes in spin-flipping avalanches, reflected by the magnetization jumps. The stochastic process of magnetization reversal occurs along the hysteresis loop, characterizing the collective response of the system. The occurrence of the out-of-equilibrium critical dynamics on the hysteresis loop together with its dependence on pertinent physical parameters, system's spatial dimensionality and shape, represent essential challenges for controlling and predicting the reversal processes in these materials.

Recently, it has been recognized that besides hysteresis-loop criticality in disordered ferromagnets, numerous other complex systems exhibit a similar avalanche-like response to the external driving forces. Further examples of such systems span from earthquakes [49–53] and propagation of interfaces in various kinds of random media [54–58] to brain networks and neuronal activity [59–62], dislocations in crystal structures [63–66], invading imbibition fronts in porous media [67,68], response of the mechanically pressured wooden materials [69] to financial booms [70] and epidemics [71], all having in common that the underlying systems evolve through the metastable states due to an avalanche type of relaxation. Despite being different at a microscopic level, these systems have some universal features of their critical states in common. This universality implies the possibility of extending the findings and methodologies developed on the systems that are tractable for experimental realizations, such as disordered ferromagnets, to characterize such phenomena in systems that are elusive to controlled experiments.

Here, we provide a comprehensive review of numerical approaches to model the criticality of the hysteresis loop in disordered ferromagnets based on extended nonequilibrium (NEQ) Random Field Ising Model (RFIM) with different physical parameters and driving regimes inspired by experimentally achievable conditions. The presented overview of the results shows how these modeling approaches, supported by advanced computational techniques using the inherent scale invariance of the dynamics, adequately describe the experimentally observed hysteresis behavior and provide new physical insights into the dynamic critical phenomena of disordered ferromagnetic systems. The developed computational techniques can be adjusted to analyze nonequilibrium critical dynamics of ferromagnetic/antiferromagnetic bilayers [72,73] and various quantum [74–76] and classical complex systems, in particular, nanonetworks [77] and higher-order self-assembled nanostructures [78–82] that are increasingly interesting to modern technology.

### ***Challenges in Numerical Modeling of Disordered Ferromagnets Hysteresis Behaviour***

Occurrence of extreme events such as infinite or system-spanning avalanches underpins the system criticality, characterized by the scale invariance of the created events whose features are power-law distributed and diverging correlation length [34]. Over time, several models were developed to describe this complex phenomenon and answer whether the model under study exhibits a critical behavior [83]. Unraveling this is not an easy task due to the multitude of mutually intertwined factors to which the underlying systems are sensitive, such as the degree of disorder or the type and rate of driving, presence of the demagnetizing fields and thermal effects, sample geometry, which is of particular relevance for applications, and other. In the following, we briefly describe these factors that represent challenges for computational modeling of the hysteresis-loop critical phenomena.

As the extensive studies [28] have shown, the critical behavior of the zero-temperature (ZT) RFIM depends on the dimension  $d$  of the studied system [31,84]. In the range of dimensions  $2 \leq d < 6$ , ZT NEQ RFIM displays a nontrivial critical behavior [31], while for  $d \geq 6$ , the behavior of the system is described by mean-field approximation [35,84,85]. In the nonequilibrium field-driven version, the system evolves through metastable states that represent local, and not global energy minima, in contrast to the equilibrium critical behaviour studied by the RFIM [86–88].

Criticality of the equilibrium and nonequilibrium version of the model for systems with dimension  $d \geq 3$ , displayed in the matching of many avalanche properties, lead to the presumption that they share the same universality class [37,87,88]. However, that is not the case for the 2D model since the ferromagnetic phase, whose existence is demonstrated in the case of nonequilibrium model [89,90], is not possible in the thermodynamic limit of the equilibrium version [91]. In an attempt to describe this nontrivial critical behavior, both perturbative [92–94] and nonperturbative renormalization group approaches [95,96] were used. Recently some advances have been made on understanding the principles of universality [36,97], dimensional reduction [98] and supersymmetry [99] in the equilibrium version of the model. On the other hand, dimension and geometry influence of underlying lattice are shown to have different impact on the nonequilibrium critical behavior [100–103].

Particular attention in the recent studies of nonequilibrium systems is devoted to the extreme, catastrophic events in which most of the system's constituents change their state [104,105]. Understanding the particular conditions under which these events occur would reveal essential details regarding the mechanism of some natural phenomena such as earthquakes, snow avalanches, cracks in materials, etc. [27,106–108], that are of immense importance due to the possible significant consequences they might cause.

In recent years, due to the increased interest in the practical applications of thin ferromagnetic materials, studies of nonequilateral systems with different geometry aspects [109] and thin systems [110–114] emerged, with some aspects in resemblance to the criticality of spin systems situated on a complex network topology [115–118]. Disordered ferromagnetics are mainly used as memory materials in the form of thin films [119–122] and nanowires [123–126], putting forward the experimental investigations of critical dynamics of BHN [127–129]. The ZT NEQ version of the RFIM was very suitable for interpreting actual experiments since the thermal fluctuations are negligible in most of them, and the underlying dynamics is closer to the one in externally driven ferromagnets. Driving these systems by the external magnetic field at finite rates [130] provides a more realistic framework for the numerical interpretation of experimental measurements conducted on ferromagnetic strips and ribbons [21,131,132] and has been of increasing interest in recent experimental studies [17,22,114,133].

Besides dimensionality, one may ask to which extent the model describes the influence of a variation of the geometry of the underlying lattice [109], including the reconsideration of the universality classes within the RFIM [100,134]. Recently, a competitive conjecture was put forward that the universality classes in the NEQ model are determined by the topology of the lattice emphasizing the role of its coordination number in addition to its spatial dimensionality [102,134–136]. This conjecture was to some extent confirmed by contrasting the criticality of the model on triangular [100], quadratic [89] and hexagonal (i.e., honeycomb) [103] 2D lattices. The absence of critical behavior for the latter lattice introduced doubt in the presumed existence of a single universality class for all periodic 2D lattices in the case of ZT NEQ RFIM.

Another significant aspect, particularly for experimental studies, is the presence of unwanted external noise in the recorded data requiring the inevitable procedure of using the discrimination threshold. In the experimentally obtained signals, avalanches are identified as signal parts outside

the imposed threshold region (i.e., the region between lower and upper threshold levels). Recent experimental [137] and theoretical [138–141] studies delivered some relevant results regarding the consequences of the implementation of the finite detection threshold when analyzing the original signal, which leads to correlated bursts of activity by separating the avalanche events into subavalanches. Effects of thresholding have also been considered in some other types of signals, e.g., in the context of fracture [142–144], and argued to be of importance in seismicity [145,146].

Driving mode represents one of the essential factors influencing the avalanche-like response. Theoretically, the three types of driving are recognized: *adiabatic*, in which the external magnetic field is increased for the exact amount needed to trigger the least stable spin and kept unchanged until the avalanche stops; *quasistatic*, in which the incrementing of the external magnetic field is performed in fixed steps until the conditions for the initiation of the avalanche are met, from which moment is kept constant as long as the avalanche propagates; and a *finite rate driving* during which, throughout the whole simulation time, the external magnetic field is increased at a constant rate. According to the value of the driving rate, the regimes of slow, intermediate and fast driving are identified [130]. The underlying dynamics in the finite driving regime is profoundly influenced by the interplay of the system's disorder and the driving rate at which the magnetic field is incremented. In this type of driving, multiple avalanches may simultaneously propagate, making the analysis and interpretation of the obtained data of the avalanching dynamics far more complex.

The different ways of driving have a significant impact on the system's behavior, with one of the most noticeable effects being the time/space profile of avalanche evolution. Adiabatic driving, during which only one avalanche is active at a time, is conducted under precisely defined conditions realizable in the numerical simulations but not in the actual experiments. A little bit closer to realistic is the quasistatic driving type, in which the regimes with small (adiabatic-like) and large field increments can be identified, promoting the temporal and occasionally spatial merging of avalanches [147]. This amalgamation of avalanches is expressed the most at the fast regime of finite rate driving protocol, comprising an overall system-spreading activity [148] without the possibility of distinguishing the contribution of individual avalanches [130,147–149]. This type of driving is even more realistic and comparable to the experimental situations. In one of the previous studies [150], it has been shown that due to the merging of avalanches (*swelling*) the overall duration of avalanches can be extended; at the same time, the merged avalanche will appear in the distribution while the merging avalanches vanish (*merging absorption*). Similarly, for the avalanches overlapped in time (and spatially separated), the overlapped avalanche appears, whereas the overlapping avalanches disappear from the distribution (*temporal absorption*). Until now, many experiments have been conducted on disordered ferromagnetic materials using the finite driving rate protocol for example, in [14–16,133]. Works in [26,150–153] attempt to describe theoretically the observed critical dynamics phenomena with the finite driving rate and its impact on the hysteresis loop and coercive field was considered in [18,19,154–156].

The study of the effects that the type of driving inflicts on the system is further augmented by employing the newly proposed *stochastic driving*, realized by stochastic increments of the external magnetic field in each time step of the system's evolution, regardless of the current state of the ongoing system's activity. This type of driving opens the possibility to extend the findings and perform the more realistic interpretation of seismic activity [50], owing to its importance due to the unwanted ramifications. In some recently conducted experiments on the propagation of a crack line in a random environment [57,142,157,158], a seismic-like behavior has been demonstrated, also found in the studies of compressional fracture [159]. Stochastic driving represents so far the most realistic scenario, allowing much closer benchmarking with the results of the experimental studies and the possibility

to extend to the numerous models developed in an attempt to explain and interpret this complex avalanche dynamics [143,160–163].

Another aspect concerns the thermal effects and the presence of the demagnetization fields in the system. These physical factors bring challenges, especially in understanding the intricate interplay of various parameters, interpreting and implementing the solution numerically, and comparing the numerical results with experiments. As shown in [164], the extended form of RFIM can be an excellent alternative for the micromagnetic modeling, which is particularly relevant for applications. The stochastic nature of the thermally triggered spin flips tends to impede accurate avalanche detection by contaminating the signal, producing an excess of minor activity events, and limiting the spread of large avalanches. Nonetheless, the demagnetizing field limits the amount of underlying spin activity events, and the maximum length of magnetization jumps by counteracting the external field and introducing non-local interactions. In a recent study [164], an appropriate algorithm to study these combined effects was developed. Notably, it demonstrates that the non-zero temperature modifies the remanent magnetization and coercive field, leading to the shrinkage of the hysteresis loop and the amplification of minor activity events. By introducing extended linear segments, the higher demagnetizing coefficient modifies the loop shape and changes the multifractal nature of the magnetization fluctuations. Similar to the analogous ZT dynamics, the statistics of well-identified intermediate-range activity events are controlled by the same scaling exponents.

In the next section, we describe the most general version of the NEQ RFIM to study the critical behavior on the hysteresis loop of disordered ferromagnetic systems, assuming different driving conditions and the aforementioned physical factors, followed by the section presenting the appropriate computational techniques. The rest of the review is structured so that each section presents the results obtained in numerical studies of particular hysteresis phenomena, emphasizing the influence of specific physical factors.

## 2 Random Field Ising Model (RFIM): Definition, Parameters and Simulation Approaches

The Random Field Ising Model describes systems of  $N_s$  mutually interacting classical Ising spins  $s_i = \pm 1$  exposed to external magnetic field  $H$  and a quenched local random magnetic field  $h_i$ . The spins are situated at the sites  $i$  of some underlying finite lattice with space dimensionality  $d$ , shape and size specified in each model realization. Mostly employed are the two-dimensional (2D), and three-dimensional (3D) lattices, however lattices of other dimensions are also used (for  $d > 3$ , see, e.g., [31]). Frequently utilized are finite lattices cut out of a corresponding infinite lattice with translation symmetry like the quadratic lattice of size  $(L_x, L_y)$  in 2D, cubic lattice of size  $(L_x, L_y, L_z)$  in 3D, and analogously hypercubic lattice for  $d > 3$ . In all three of the foregoing lattice examples the number  $z_m$  of nearest neighbors for each site equals  $2d$ , however, this number can be different for other types of lattice elementary cell, like  $z_m = 6$  for the triangular [100], and  $z_m = 3$  for the honeycomb [103] 2D lattices. Finally, the model can be situated on a lattice without translation symmetry, such as Bethe lattice, and/or translation symmetry may be absent due to the presence of irregularly distributed vacancies (lattice sites not ‘occupied’ by a spin), and/or irregular interfaces consisting of spins with fixed value.

In general, the interaction of each spin  $\vec{s}_i$  with the external magnetic field is accomplished through the coupling  $-\mu_0 \vec{m}_i \cdot \vec{H}_i(t)$  between the magnetic dipole moment  $\vec{m}_i = \gamma_i^{(s)} \hbar \vec{s}_i$  associated with  $\vec{s}_i$ , and the external magnetic field  $\vec{H}_i(t)$  at the spin’s site  $i$  at the current moment (of time)  $t$ ; here,  $\gamma_i^{(s)}$  is the gyromagnetic ratio for the spin  $\vec{s}_i$ , usually taken to be the same for all spins in the model,  $\gamma_i^{(s)} = \gamma^{(s)}$ . Because the RFIM is not a vector spin model, one can assume here that some (arbitrary) direction is chosen in space such that for all spins the projection  $\vec{s}_i \cdot \vec{u}_0$  of  $\vec{s}_i$  onto the unit vector  $\vec{u}_0$  of this

direction equals  $s_i$  enabling in the RFIM the incorporation of the coupling between spins and the external magnetic field as  $-H_i(t)s_i$ ; here,  $H_i(t) = \vec{H}(t) \cdot \vec{u}_0$  is the projection of  $\vec{H}$  onto  $\vec{u}_0$ , and the units are appropriately rescaled for simplicity (which is allowed in models).

Analogous form  $-h_i s_i$  is taken for the coupling between the spin  $s_i$  and the random field  $h_i$  at the spin's site  $i$ . This local random field  $\{h_i\}_{i=1}^{N_s}$  is postulated as quenched (meaning that its values are fixed in time), and could be considered to originate from various types of real systems' imperfections not specified in the RFIM. Besides, this field is random, meaning that its values  $h_i$  at different lattice sites are chosen out of some type of zero-mean random distribution  $\rho(h)$  with finite standard deviation  $R$  measuring *disorder* in the RFIM systems, which could be site-dependent. Here, the common approach is to use Gaussian distribution,  $\rho(h) = \frac{1}{R\sqrt{2\pi}} \exp(-h^2/2R^2)$ , with the same disorder  $R$  for all sites. The RFIM studies, performed with another choice of the random field distribution  $\rho(h)$ , exist but are relatively rare-see, e.g., the case of parabolic and uniform distributions in [87], Laplace and double Gaussian distribution in [97], and the case of Gaussian distribution with  $R$  modulated by the presence of crystal grains [165].

Independent on the choice of the distribution  $\rho(h)$  is the question whether there is some correlation between the values of random field at different lattice sites. When the values are uncorrelated, then  $\langle h_i h_j \rangle = R_i^2 \delta_{ij}$ , where  $\delta_{ij}$  is the Kronecker delta function and  $R_i$  is the value of disorder at the site  $i$ . This is the case in majority of past RFIM studies although the model itself doesn't exclude possible correlations.

Besides the interaction of spins with magnetic fields (external and random), the spins also mutually interact. The strongest type of interaction between the spins is the (electrostatic in nature) exchange interaction between pairs of spins, giving the contribution  $-J_{ij} s_i s_j$  from each pair  $s_i$  and  $s_j$ , to the overall system Hamiltonian through the coupling constant  $J_{ij}$ . When  $J_{ij} > 0$  the coupling is ferromagnetic, for  $J_{ij} < 0$  the coupling is antiferromagnetic, while for  $J_{ij} = 0$  the spins  $s_i$  and  $s_j$  are exchange decoupled. The exchange interaction is typically considered as short-ranged, meaning that it is the most prominent for the nearest neighbor spins and significantly weaker for further neighbors (e.g., exponentially decaying with the inter-site distance). On this ground, frequently used is the nearest-neighbor approximation in which all pairs of spins except nearest neighbors are considered as exchange decoupled.

Another type of spin-spin interaction is the dipole-dipole interaction between the magnetic dipole moments  $\vec{m}_i$  and  $\vec{m}_j$  associated with pair of spins  $\vec{s}_i$  and  $\vec{s}_j$ . In general, the dipole-dipole interaction is of the form

$$-\frac{\mu_0(\gamma^{(s)})^2 \hbar^2}{4\pi r_{ij}^5} [3(\vec{s}_i \cdot \vec{r}_{ij})(\vec{s}_j \cdot \vec{r}_{ij}) - \vec{s}_i \cdot \vec{s}_j r_{ij}^2],$$

where  $\vec{r}_{ij} = \vec{r}_i - \vec{r}_j$  is the position vector of site  $i$  relative to site  $j$ . In the RFIM this expression is simplified to

$$-J_{\text{dipole}} \frac{3\cos^2\theta_{ij} - 1}{r_{ij}^3} s_i s_j,$$

where  $J_{\text{dipole}} = \mu_0(\gamma^{(s)})^2 \hbar^2 / 4\pi$ , and  $\theta_{ij}$  is the angle between  $\vec{r}_{ij}$  and  $\vec{u}_0$ . Being inversely proportional to the cube of inter-site distance  $r_{ij}$ , the dipole-dipole interaction is not (like the exchange interaction) limited to near spins, but instead, it affects all pairs of spins, i.e., it is long-ranged. Yet, it is typically weaker than the exchange interaction, and therefore often omitted in the model analysis.

Besides, the spins located at the boundaries of finite lattices generate inside the sample a long-range (effective) demagnetizing magnetic field which acts against the external field. In the RFIM, this field is taken as a homogeneous field  $-J_D M$  and its coupling with individual spins as  $J_D M s_i$ , where  $M = (\sum_i s_i)/N$  is the actual magnetization of the system and  $J_D \geq 0$  is the demagnetization coefficient (factor). The adopted form of demagnetizing field is by all means approximate, so in simulations and analyses it is most appropriate to assign such values to  $J_D$  that conform to the values theoretically found for the homogeneously magnetized samples (e.g.,  $J_D = 1/3$  for cubic and spheroidal samples).

Therefore, the most general form of Hamiltonian for the RFIM spin systems in the external magnetic field with a time profile  $H_i(t)$  reads

$$\mathcal{H} = - \sum_{\langle ij \rangle} \left( J_{ij} + J_{\text{dipole}} \frac{3 \cos^2 \theta_{ij} - 1}{r_{ij}^3} \right) s_i s_j - \sum_{i=1}^{N_s} (H_i(t) + h_i - J_D M) s_i, \quad (1)$$

where the summation in the first term is performed over all pairs of distinct spins, so that each spin  $s_i$  is under the influence of the *effective magnetic field*

$$h_i^{\text{eff}}(t) = \sum_{j \neq i} \left( J_{ij} + J_{\text{dipole}} \frac{3 \cos^2 \theta_{ij} - 1}{r_{ij}^3} \right) s_j + H_i(t) + h_i - J_D M, \quad (2)$$

giving contribution  $-s_i(t)h_i^{\text{eff}}(t)$  to Hamiltonian (1). If  $s_i(t)h_i^{\text{eff}}(t) \leq 0$ , the spin  $s_i(t)$  is *field-unstable* at the moment  $t$ , and the value of Hamiltonian (1), henceforth simply the system energy, will be reduced by flipping of  $s_i$  (i.e., change of  $s_i$  to the opposite value  $-s_i$ ). Otherwise, if  $s_i(t)h_i^{\text{eff}}(t) > 0$ , the spin  $s_i(t)$  is *field-stable*, so its flipping would increase the system energy.

Although absent in Hamiltonian (1), the lattice-spin interactions are indirectly present in the RFIM through the thermal fluctuations of spins manifested when the system temperature  $\Theta > 0$  in which case the model is called *thermal*. Otherwise, when  $\Theta = 0$ , the thermal fluctuations of spins are absent and the model is *athermal* or zero-temperature. This  $\Theta = 0$  version of RFIM is of twofold importance because in many real-world systems, to which the RFIM can be applied, the thermal fluctuations are negligible in the relevant range of temperatures, and also because the athermal RFIM version is much simpler than the thermal, both for simulations and analyses.

In the RFIM, the state  $\{s_i\}_{i=1}^{N_s}$  of the spin system changes through the flipping of individual spins. In the nonequilibrium (NEQ) model version, which is the subject of this review article, the individual spins flip due to appropriate change of their effective magnetic field and/or thermally if  $\Theta > 0$ . Thus, in the athermal NEQ RFIM version, only the first cause applies, and this is usually done by *parallel updating* of orientation of spins, meaning that all spins which are field-stable at the moment  $t$  will remain unchanged and the field-unstable spins will be flipped at the next moment  $t + \Delta t$  (in simulations, both  $t$  and its increment  $\Delta t$  are discrete, usually with  $\Delta t = 1$ ). Due to such local dynamical rule and parallel updating, the system evolves deterministically, traversing (almost exclusively) through the nonequilibrium states in a tendency to reduce its energy. Other (and less used) way, employed in the athermal model version, is to perform sequential field-stability testing and flipping of spins one by one, in which case the system's evolution depends on the random order in which the spins are tested.

Flipping of spins, together with a possible change of the external magnetic field, modifies the effective magnetic field  $h_i^{\text{eff}}$  of the system's spins. Thus, when  $J_D > 0$ , the magnetization  $M$  is (typically) altered due to spin flipping which causes a change in  $h_i^{\text{eff}}$  for all spins through the term  $-J_D M$  in (2). Also, the dipole-dipole interaction term in (2) becomes different for all (especially near) spins, provided that this type of interaction is included in the model. However, the contribution coming from the

change in the exchange-coupling term in (2) is the most prominent, or the only one when  $J_D = 0$ ,  $J_{\text{dipole}} = 0$ , and constant  $H$  at the next moment  $t + \Delta t$ .

In thermal (i.e.,  $\Theta > 0$ ) model, together with the preceding field-stability testing, the spins are also checked for *thermal flipping*. Thus, in [166], the changes  $\Delta H$  of the external magnetic field are sandwiched between a preselected number  $N_{\text{th}}$  of Monte-Carlo sweeps sequentially applied, so that in each sweep a spin  $s_i$  is randomly chosen and flipped with the probability  $\min(1, e^{-\Delta E_i/\Theta})$ , where  $\Theta > 0$  is the temperature, and  $\Delta E_i$  is the change in energy proposed by flipping of  $s_i$ . By this rule, the selected spin  $s_i$  is certainly flipped if it is field-unstable ( $\Delta E_i < 0$ ), however, if it is field-stable ( $\Delta E_i > 0$ ), it may be also flipped with probability  $e^{-\Delta E_i/\Theta}$ . As a consequence, the central role is played by the time-scale of thermal flipping, set by the number  $N_{\text{th}}$  regardless of the system size, while the time-scale for the field changes is introduced indirectly, relative to the thermal flipping time-scale.

To check the stability at the current moment for all (and not only selected) spins, a different approach is proposed in [164]. There, the thermal flipping is tested on a set of spins, randomly selected at each moment  $t$  and containing a preselected fraction  $c = \Delta N_s/N_s$  of spins. At the next moment  $t + \Delta t$ , each spin outside this set will be flipped if it is field-unstable, while each spin  $s_i$  from the set will be flipped with the (Boltzmann-type) probability of thermal flipping probability

$$P_i^{(\text{th})} = \frac{\exp(-s_i h_i^{\text{eff}}/T_r)}{\exp(-s_i h_i^{\text{eff}}/T_r) + \exp(s_i h_i^{\text{eff}}/T_r)}, \quad (3)$$

where the parameter  $T_r = \Theta/T_c$  stands for the temperature relative to some temperature  $T_c$  that is characteristic in the model for the underlying system (e.g.,  $T_c = J$  for the system of purely ferromagnetic spins with  $J_{ij} = J$ ). Hence, for  $s_i h_i^{\text{eff}} < 0$  (i.e., if the selected spin  $s_i$  is field-unstable) it is likely (but not certain) that it will be flipped, whereas for  $s_i h_i^{\text{eff}} > 0$ , the selected spin  $s_i$  has a small nonzero chance for flipping.

As stated, the external magnetic field varies in time in the NEQ RFIM. This is realized either in some deterministic variation pattern (e.g., adiabatic, quasistatic, finite driving rate), or by stochastic external field increments (see, e.g., Reference [149]). In the adiabatic and quasistatic driving protocols, employed in the athermal model versions, the external field is changed only if all spins in the system are field-stable. In the adiabatic case the field is changed in the exact amount that destabilizes the least stable spin (and flips it at the next moment), while in the quasistatic driving the field increment is constant,  $\Delta H = \text{const}$ , possibly causing flipping of one or more spins, especially for the large systems. Flipping of spin(s) may destabilize some spins (most often the nearest neighbors of the flipped spin); their flipping may further destabilize other spins, and so on, leading to a time-series of flipping in the form of an *avalanche*. In the case of adiabatic models with  $J_D = 0$ ,  $J_{\text{dipole}} = 0$ , and the exchange coupling limited only to the nearest neighbors, each avalanche is nucleated by flipping of a single spin and afterward spread over a cluster of (connected) spins. In other adiabatic cases, or when the driving is quasistatic, multiple avalanche nucleations at spatially distant locations may happen. This leads to the onset of avalanches that simultaneously propagate over several spin clusters initially space-separated and later possibly merging in space. Whether due to such, or to individual avalanches, the system response is expressed in terms of the numbers  $n_+(t)$  and  $n_-(t)$  of spins that flip up and down at the moment  $t$ , giving the *response signal* of the system,  $V(t) = n_+(t) - n_-(t)$ , and the corresponding change in magnetization  $\Delta M(t) = 2V(t)$  during one time-step at the moment  $t$ . Each subsequence of the  $V(t)$  sequence, consisting of consecutive terms such that the underlying  $n_+(t)$  and  $n_-(t)$  satisfy  $n_+(t) + n_-(t) > 0$ , represents a system *activity event*, which is a generalization of an individual avalanche.

In addition to adiabatic and quasistatic driving (which tends to adiabatic when  $\Delta H \rightarrow 0$  for any finite system), there is the finite rate driving protocol in which the external magnetic field, regardless of the system activity, increases/decreases along the rising/falling part of the magnetization curve at some constant driving rate  $\Omega = \Delta H/\Delta t$  (given by the field increment/decrement  $\Delta H$  when  $\Delta t = 1$  and also tending to adiabatic when  $\Omega \rightarrow 0$ ). This type of driving, enhancing spin flipping and thus facilitating activity propagation due to perpetual modifications of spins effective magnetic field, is of considerable importance because it is encountered in a large number of experiments performed on magnetic systems.

Compared to athermal model, the system response is essentially different in the thermal model regarding events duration. Thus, while all events in athermal model are of finite duration this is almost never the case in the thermal model due to the thermal flipping of spins. For this reason, unless some threshold is introduced, the decomposition of system response into activity events separated in time is impossible, making the adiabatic and quasistatic driving unrealistic. So, in [164], the external magnetic field is incremented in each step, whereas in [166] the field is incremented after  $N_{\text{th}}$  (elemental) time-steps, while meanwhile the thermal flipping of spins is performed. Note that in pure ferromagnetic case, due to thermal flipping and other factors influencing the effective magnetic field, some spins may be back-flipped, i.e., changed from  $+1$  to  $-1$  on the rising part of magnetization curve (and opposite on the falling part). Such back-flipping is possible when  $J_D > 0$  even in athermal model and impossible when  $J_D = 0$  and  $J_{\text{dipole}} = 0$ .

The analysis of RFIM systems evolution is commonly performed on their response signal decomposed into events; the exception is the analysis of power spectra  $P(f)$  [167] giving the variation with frequency  $f$  of the released power frequency density which is performed without any decomposition on the entire selected part or on the whole response signal. In the athermal version of ferromagnetic systems each activity event gives a part of consecutive non-zero values in the response signal,  $V(t) > 0$  along the rising part of the magnetization curve (and  $V(t) < 0$  along the falling part). These parts are taken as events which are the subject of further statistical analysis. In other cases, such simple decomposition is impossible, and the decomposition of the response signal into events is accomplished with the aid of some (suitably chosen) discrimination threshold  $V_{\text{th}}$ . Provided that  $V_{\text{th}} \geq 0$  is selected, the response signal is decomposed into longest subsequences  $\{V(t_i), V(t_{i+1}), \dots, V(t_e)\}$  consisting of signal values  $|V(t)| > V_{\text{th}}$ , all positive (or all negative), and registered in consecutive moments between the initial moment  $t_i$  and ending moment  $t_e$  of the subsequence in question. Each such subsequence is considered as an *event*, and for any moment  $t$  that is outside all events  $|V(t)| \leq V_{\text{th}}$ . Each event can be characterized by several parameters like its duration  $T = t_e - t_i + 1$ , size  $S = \sum_{t_e \leq t \leq t_i} V(t)\Delta t$ , energy  $E = \sum_{t_e \leq t \leq t_i} V^2(t)\Delta t$ , and amplitude  $A = \max\{|V(t_i)|, |V(t_{i+1})|, \dots, |V(t_e)|\}$ , and for each such parameter  $X$  the corresponding distribution  $D_X(X)$  is collected. These distributions can be either *integrated* (i.e., collected from the entire signal), or *windowed* (i.e., collected in a selected window  $(H_{\text{min}}, H_{\text{max}})$  of the external magnetic field). Besides, the distributions can be classified according to the event's type (e.g., nonspanning and different types of spanning events). Among possible distribution shapes, of particular importance are those of the type

$$D_X(X) = X^{-a} \mathcal{D}_X(X), \quad (4)$$

representing a power-law with cutoff specified by the *power-law exponent*  $a$  and the so-called *cutoff* function  $\mathcal{D}_X(X)$  which (beside  $X$ ) depends on some parameters for simplicity not shown in notation. The analytic form (4) describes a pure power-law,  $D_X(X) \propto X^{-a}$ , only in some limits of the cutoff function parameters leading to  $\mathcal{D}_X(X) \rightarrow \text{const}$ . Outside such limits the cutoff function rapidly tends

to zero for large  $X$  (and possibly for very small  $X$ ), while in between, a region of moderate  $X$ -values may exist such that  $\mathcal{D}_X(X) \approx \text{const}$ . If so, this region is called the *scaling region*, and it could be used for determination of the value of the power-law exponent as  $a$  equals the gradient (i.e., slope) of the scaling region data presented in a log-log plot; other (and preferred) method is by the collapsing of data which can be applied when the cutoff function has universal scaling properties as will be demonstrated in the Results sections. For the later convenience, here we quote the common RFIM exponents:  $\tau$ ,  $\alpha$ ,  $\varepsilon$ , and  $\mu$  for the windowed distributions of event's size, duration, energy, and amplitude, respectively; additional NEQ RFIM exponents will be introduced in the Results sections.

Besides, other quantifiers of response signal can be defined, like the magnetization as a function of the external magnetic field,  $M = M(H)$ , and analogously the susceptibility  $dM/dH$ , the correlation functions, average event shape, and the distributions of various types of waiting time, like the external waiting time  $T_{\text{ext}}$  measuring the separation in time of consecutive events.

Integral part of model is the specification of boundary conditions which are either closed or open on each system boundary. Closed conditions mean that the spin values are periodic along the corresponding direction, e.g.,  $s_{(i_x, i_y, i_z)} = s_{(i_x+L_x, i_y, i_z)}$  in the case of  $(L_x, L_y, L_z)$  3D cubic lattice and closed boundary condition along  $x$ - direction. Closed boundary conditions are important because they enable faster convergence towards the infinite systems. On the other hand, they are less realistic than the open boundary conditions for which there are no spins outside considered lattice.

When studying system evolution, initial conditions have to be specified that include the initial state for all spins and the external magnetic field. If suitable, terminal conditions are specified as well.

Finally, let us explain the role of averaging. Averaging is performed in order to collect more reliable statistics of system response. However, for fully deterministic variants of the model repeating the simulation under identical conditions is useless because it gives exactly the same results. In such cases, the so-called *quenched averaging* is performed in which the simulation is repeated using different configurations of the random field corresponding to the same choice of disorder and the same values of the remaining model parameters. Otherwise, the simulations may be repeated using the same configuration of the random field but with randomized other thermal ingredients, e.g., the different sets of spins tested for thermal flipping.

The theoretical analyses of the NEQ RFIM was focused so far on the possible critical behavior of this model. Thus, for the adiabatically driven ZT model situated on the (hyper)cubic lattices, the renormalization group (RG) analyses [28,37,84] have revealed a mean-field behavior for dimensions  $d \geq 6$  and a nontrivial critical behavior for  $3 \leq d < 6$ , but without the final RG conclusions about the 2D case.

Having explained the main features of various versions of the NEQ RFIM, let us briefly state the main characteristics of the equilibrium model. In this RFIM version at each external (commonly homogeneous) magnetic field of interest is only the ground spin state (or states in the case of frustration when more than one state have minimal energy) at  $\Theta = 0$ , whereas for  $\Theta > 0$ , the corresponding thermal distribution of spin states is analyzed. Hence, the temporal evolution of the underlying spin system remains out of the scope together with all associated features (events, power-spectrum, waiting times, etc.). For this reason, the equilibrium version is less informative than the nonequilibrium version, especially for the analyses of response of the real-world systems. Nevertheless, the equilibrium version is very important in theoretical studies revealing many conclusions that are not attainable within the nonequilibrium version.

As mentioned in the Introduction, the focus of this review is on extensive computational techniques and simulations of the field-driven spin reversal dynamics, avalanches statistics, finite-size scaling, correlations and multifractal analysis of Barkhausen noise signals, that are developed to study the nonequilibrium criticality of the hysteresis loop. They are detailed throughout the results presented in different sections. More precisely, in the following section, we give the fundamental aspects of the simulations, which are then adapted and elaborated in each section to analyze different driving modes, dimensionality and sample shapes, athermal and thermal fluctuations and demagnetizing effects. See also the program flow in [Section 6.1](#), which refers to the model with demagnetizing fields. In addition, a systematic comparison of the analysis of simulated data and data collected in the experiment with the nanocrystalline sample in [168] is presented; see [Section 7.1](#). It demonstrates the advantages and disadvantages of presented numerical experiments compared to laboratory experimental data.

### 3 Simulational Methods in the RFIM

Even in the simplest model version, the RFIM simulations are computationally very challenging. Realization of the finite-size scaling analysis, and avoiding the finite-size effects, demand simulations of very big systems (e.g., with  $10^9$  spins) which require large amounts of computer memory and long running time even for a single run, let alone for repeated simulations with different realizations of the random magnetic field necessary for quenched averaging. Efficient algorithms are therefore a must regarding both memory (RAM and storage) space and execution time.

An essential breakthrough in simulations is achieved by the *sorted-list* algorithm and *bit-per-spin* algorithm detailed in [169] for the adiabatically driven athermal NEQ RFIM (with  $J_{ij} = J > 0$  for nearest neighbors and zero otherwise,  $J_{\text{dipole}} = J_D = 0$ , and homogeneous  $H$ ). In this case, the external magnetic field  $H$  is to be increased only after all spins become stable and that by the amount triggering the least stable spin. To find it, the easiest tactic is to check the values of the effective magnetic field  $h_i^{\text{eff}}$  at all lattice sites  $i$ , find the site  $i_0$  with the least negative value of  $h_i^{\text{eff}}$ , increase  $H$  by  $\Delta H = -h_{i_0}^{\text{eff}}$ , and flip the spin  $s_{i_0}$ . Then, iteratively until the system becomes stable, for all spins flipped at the previous moment, flip at the next moment their nearest neighbors that became unstable. Despite being simple, the preceding algorithm, named the *brute-force* method, is extremely slow because its total running time scales as  $O(N_s^2)$ ; therefore it is not used in simulations of larger systems (with, e.g., more than  $10^5$  spins) even by modern (sequential) computers.

Traversing the whole lattice in search for the least stable spin is avoided in the sorted-list algorithm. To this end, the array  $\{h_i\}_{i=1}^{N_s}$  of the random field values, generated before the start of the simulation, are sorted in descending order,  $\{h_{\pi(1)} > h_{\pi(2)} > \dots > h_{\pi(N_s)}\}$ , where  $\pi : \{1, \dots, N_s\} \rightarrow \{1, \dots, N_s\}$  is the permutation such that  $\pi(k)$  points to the index of the element in the original array occupying  $k$ -th position in the sorted array  $h \circ \pi$ . Also is introduced a pointer (integer) array  $\{P_{n_\uparrow}\}_{n_\uparrow=0}^{z_{mn}}$  and all its elements initially set to 1. After the system becomes stable at the current value of  $H$ , each element  $P_{n_\uparrow}$  of this (nondecreasing) array is updated (increased) so to point to the smallest index  $k$  in the sorted array, i.e., to the largest element in the sorted array  $h \circ \pi$ , such that  $s_{\pi(k)}$  would flip if it had  $n_\uparrow$  upward oriented nearest neighbors, and the external field for that  $n_\uparrow$  set to  $H_{\text{new}}(n_\uparrow) > H$  equal to  $H_{\text{new}}(n_\uparrow) = -[(2n_\uparrow - z_{mn})J + h_{\pi(k)}]$ . Thereupon, the external magnetic field is updated to the new value  $H_{\text{new}} = \min\{H_{\text{new}}(n_\uparrow) : n_\uparrow = 0, 1, \dots, z_{mn}\}$ , and the new avalanche nucleated by flipping the least stable spin caused by  $H \rightarrow H_{\text{new}}$ .

Having the total running time that scales as  $O(N_s \log N_s)$ , the sorted-list algorithm is, so far as is known, the fastest algorithm used for simulations of the adiabatically driven athermal NEQ RFIM. However, the algorithm is memory-hungry because, besides the arrays used for storing the spins and

the random magnetic field, it requires an additional integer array  $\{\pi_i\}_{i=1}^{N_s}$  keeping track about the permutation used in sorting the original array  $\{h_i\}_{i=1}^{N_s}$ , requiring for storage at least 64 bits of memory per each element.

The bit-per-spin algorithm greatly reduces memory demands because it eliminates the need for the array  $\{h_i\}_{i=1}^{N_s}$ . Besides this, memory is additionally saved by storing each spin in only one bit of memory, also possible in any other algorithm regarding the storage of Ising spins. Although the algorithm's historical name refers to bit-per-spin memory storage, the main aspect of its optimization is generating the random field values on the fly, resulting in at least 96 times reduced memory demands, but at the cost of approximately two-fold increase in the execution time. Thus, the array  $\{h_i\}_{i=1}^{N_s}$  is not generated before the start of the simulation, nor the memory for its storage is reserved. Instead, provided that the system is stable at the external field  $H_{old}$ , a new value of the external field,  $H_{new}$  is found. To this end, using the complementary error function  $\text{erfc} = (2/\sqrt{\pi}) \int_x^\infty \exp(-t^2) dt$ , one firstly calculates the probabilities

$$P_\downarrow(n_\uparrow, H) = \frac{1}{2} \text{erfc} \left( \frac{H + (2n_\uparrow - z_{nn})J}{R\sqrt{2}} \right), \quad (5)$$

that at the value  $H$  of the external field a spin with  $n_\uparrow$  up neighbors is pointing down, and consequently the probability

$$P^{\text{none}}(H_{old}; H_{new}) = \prod_{n_\uparrow=0}^{z_{nn}} \left[ \frac{P_\downarrow(n_\uparrow, H_{new})}{P_\downarrow(n_\uparrow, H_{old})} \right]^{N_{n_\uparrow}}, \quad (6)$$

that no spin has flipped between  $H_{old}$  and  $H_{new}$ . After that, the equation

$$r_n = P^{\text{none}}(H_{old}; H_{new}), \quad (7)$$

is numerically solved for a chosen random number  $r_n$  (uniformly distributed between zero and one), using in this solving the recipe from [169], for example. In the next step, the rates for spin flipping for each  $n_\uparrow$  at the  $H_{new}$  are calculated according to

$$\Gamma(n_\uparrow, H_{new}) = N_{n_\uparrow} \frac{\rho(H_{nr}(n_\uparrow, H_{new}))}{P_\downarrow(n_\uparrow, H_{new})}, \quad (8)$$

where  $N_{n_\uparrow}$  is the number of spins with  $n_\uparrow$  up neighbors (taken before  $H$  is set to  $H_{new}$ ), and  $\rho(H_{nr}(n_\uparrow, H_{new}))$  stands for the Gaussian distribution  $\rho(h) = \exp(-h^2/2R^2)/R\sqrt{2}$  of the random field at  $h = H_{nr}(n_\uparrow, H_{new})$ , where  $H_{nr}(n_\uparrow, H_{new}) = H_{new} + (2n_\uparrow - z_{nn})J$ . For these rates  $\Gamma(n_\uparrow, H_{new})$ , the total rate

$$\Gamma(H_{new}) = \sum_{n_\uparrow=0}^{z_{nn}} \Gamma(n_\uparrow, H_{new}) \quad (9)$$

is calculated and  $n_\uparrow$  selected using another random number uniformly distributed between zero and  $\Gamma(H_{new})$ . Finally, randomly searching the lattice, a down spin with  $n_\uparrow$  up neighbors is found and flipped. This way a new avalanche is nucleated and its propagation at  $H_{new}$  is followed like in the brute force method until the ongoing new avalanche dies. The whole preceding procedure (for finding  $H_{new}$  and propagating the emerged avalanche) is iteratively repeated, until all spins become stable in the up state.

The bit-per-spin algorithm enabled large-scale simulations in the last decade of the XX century standing as a breakthrough in the numerical studies of the model [31,170]. Together with the sorted-list algorithm, it was later extended to be applicable for the quasistatic [147], finite-rate [130,148,171,172],

and stochastic driving [149] along the entire hysteresis loop. Nevertheless, their extension was impossible for the RFIM versions modelling the systems at finite temperatures and/or systems having a more complex inter-spin interaction (e.g., nonhomogenous exchange interaction, combined ferromagnetic-antiferromagnetic layers, vacancies, interfaces, etc.). In these cases, the single run execution time is possible to be reduced by converting the brute-force method from the sequential to parallel code, which is particularly convenient for the shared-memory systems using Message Passing Interface (MPI)—a standard designed to function on parallel computing architectures. Note, however, that the sequential code provides the shortest run-time per thread, and that the run-time acceleration usually rapidly saturates with the number of involved parallel threads. This, together with the repetition of simulations with different random field configurations requested for the quenched averaging, means that the number of involved parallel threads has to be compromised to achieve the least overall execution time of the whole set of simulations. An example of the flowchart of a parallel algorithm is given in [Section 6.1](#).

Besides sophisticated simulation algorithms, the RFIM studies also have computational challenges regarding the extraction of the relevant statistics and their subsequent analysis. As an illustrative example, let us describe the algorithm proposed in [89] for the collapsing of the suitably scaled distributions. These distributions are of the power-law type and are represented by their histograms collected in the logarithmic bins which reduces the random scattering at the side of large events. Thus, for a given set of discrete histograms, one firstly finds the union set  $X$  of all their ordinates, next for each  $x$  in  $X$  the (weighted) mean of the interpolated curves, and then the width around this mean curve, resulting in a merit function (i.e., width  $w$ ). Various types of interpolation and weighted widths can be used, which is important for noisy data having different uncertainties. The simplest choice is the linear interpolation, no weights, and width  $w = \sqrt{D_2/N_p}$ , where  $D_2$  is the sum of squared distances from the mean curve, and  $N_p$  is the number of degrees of freedom (crudely equal to the number of points in  $X$ ).

## 4 Adiabatic Collective RFIM Dynamics with Spin-Flipping Avalanches

### 4.1 Zero-Temperature (ZT) Nonequilibrium (NEQ) RFIM on Three-Dimensional (3D) Simple Cubic Lattice

Previous theoretical and numerical studies [28,35,84,89] have shown that the adiabatically driven ZT NEQ RFIM systems, situated at the equilateral (hyper)cubic lattices with dimension  $d \geq 2$ , exhibit in the thermodynamic limit ( $L \rightarrow \infty$ ) a dynamical critical behavior at the ( $d$ -dependent) value of *critical disorder*  $R_c(d)$ , discriminating two domains of disorder. This value, denoted as  $R_c$  in what follows, separates the ferromagnetic phase that exists for low disorders  $R < R_c$ , at which the infinite avalanche appears causing a jump in magnetization, from the paramagnetic phase occurring for high disorders  $R > R_c$ , in which no infinite avalanche is created, so the magnetization curve is smooth.

In finite systems, the role of infinite avalanches is played by the spanning avalanches [27] spreading along at least one of the system's spatial dimensions and, therefore, classified according to the number of dimensions they span as 1d, 2d, and 3d spanning avalanches (further classified in [27] into critical and subcritical 3d spanning avalanches [173]). As shown in the comprehensive work investigating the ZT NEQ RFIM on finite equilateral 3D cubic lattices [108], the distributions of the number  $N_s(R; L)$  of all spanning avalanches per single run in the systems of size  $L$ , illustrated in the main part of [Fig. 1a](#), scale as

$$N_s(R; L) = L^\theta \tilde{N}_s(rL^{1/\nu}), \quad (10)$$

see in the inset of [Fig. 1a](#), where  $\tilde{N}_s(rL^{1/\nu})$  is the universal scaling function employing the reduced disorder  $r = (R - R_c)/R$ , and  $\theta$  is the exponent whose value is, after considering the significantly

wider range of the employed values of  $L$ , with great accuracy refined in [108] to  $\theta = 0$ . Additionally, it was shown in [108] that the distributions  $N_s(R; L)$  are well-described by the model function

$$N_s^{\text{mod}}(R; L) = H \exp \left\{ -\left[ \frac{R - R_c^{\text{eff}}(L)}{W(L)} \right]^2 / 2 \right\} + 0.5 \operatorname{erfc} \left\{ \left[ \frac{R - R_c^{\text{eff}}(L)}{W(L)} \right] \right\}, \quad (11)$$

depending on parameters  $H$ ,  $R_c^{\text{eff}}(L) > R_c$ , and  $W(L)$  which specify height, center, and width of the Gaussian in the first addend of the Eq. (11). Besides,  $R_c^{\text{eff}}(L)$  and  $W(L)$  in the second addend specify the inflection point and the width of the complementary error function taking values 0.75 and 0.25 for  $R = R_c^{\text{eff}}(L) - W(L)$  and  $R = R_c^{\text{eff}}(L) + W(L)$ , and 0.5 at the inflection point  $R = R_c^{\text{eff}}(L)$ . For large  $L$ , the width becomes very small tending to zero as  $W(L) \sim L^{-1/\nu}$ , while  $R_c^{\text{eff}}(L) \rightarrow R_c$  according to  $[R_c^{\text{eff}}(L) - R_c]/R_c^{\text{eff}}(L) \sim L^{-1/\nu}$ . As long as  $R$  is significantly below  $R_c^{\text{eff}}(L) - W(L)$  only one (3d) spanning avalanche appears per run, so that  $N_s(R; L) \approx 1$ . Therefrom, the number  $N_s(R; L)$  increases when  $R$  grows and reaches its maximum at  $R = R_c^{\text{eff}}(L)$ , followed by a rapid decrease towards zero as  $W(L)$  is small when  $L$  is large. Owing to such behavior,  $R_c^{\text{eff}}(L)$  is singled out as a characteristic value of disorder that can be considered as the *effective critical disorder* for the systems of size  $L$  such that (in simplified terms) the spanning avalanches are absent for  $R > R_c^{\text{eff}}(L)$  or (more precisely) unlikely for  $R$  surpassing  $R_c^{\text{eff}}(L) + W(L)$ . As a consequence, three domains of disorder with distinct scaling exist for finite systems with negligible  $W(L)$ , namely the domain of low (or subcritical) disorders for  $R < R_c$ , the domain of transitional disorders for  $R_c < R < R_c^{\text{eff}}(L)$ , and the domain of high (or supercritical) disorders for  $R > R_c^{\text{eff}}(L)$ , taking into account that for smaller systems the borders of the domains are not very sharp due to finite  $W(L)$ .

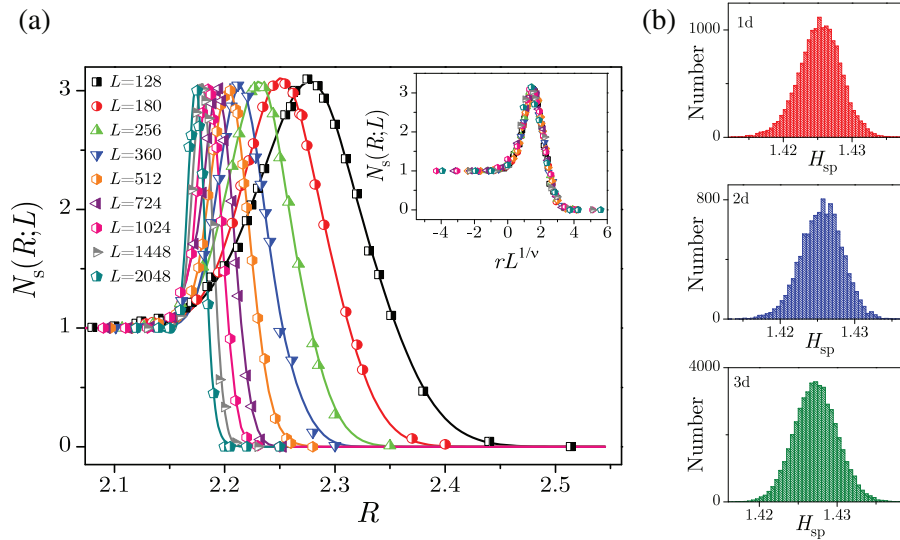


**Figure 1:** The total number of spanning avalanches per single run,  $N_s(R; L)$ , and their scaling collapse (10) are displayed by symbols in the panel (a) and its inset. The model curves (11) that best fit the  $N_s(R; L)$  data are shown by the full lines in the main part of this panel. (b) The histograms of spanning field  $H_{\text{sp}}$  for 1d, 2d and 3d spanning avalanches obtained for system with size  $L = 128$  and disorder  $R = 2.22$ . Presented data are averaged over 40,000 different realizations of the random field. Figure is replotted from Reference [108], combining parts of Figs. 1 and 2

Results published in [108] are obtained in by-all-means extensive numerical simulations, averaged across up to 200,000 distinct realizations of the random magnetic field for up to 36 various values of disorder on the systems with lattice size up to  $L = 2048$  containing almost  $10^{10}$  spins. These results

showcase that for disorders  $R > R_c^{\text{eff}}(L) + W(L)$ , surpassing the effective critical disorder, the systems' properties are almost independent on the lattice size  $L$ , practically obeying the scaling predictions that hold in the thermodynamic limit. However, significant size-dependence is documented in the other two disorder domains, subcritical and transitional, evident in all characteristic features of systems' behavior.

In the subcritical and transitional domains of disorder, the single-run magnetization curves have jump(s) that appear at the *spanning field*  $H_{\text{sp}}$  (i.e., the value of the external field at which a spanning avalanche is triggered) whose values are determined by the chosen RFC. As the distribution of  $H_{\text{sp}}$  values (due to varying employed RFCs) is not sharp but of finite width, see Fig. 1b, the positions of magnetization jumps are smeared, cf. bottom-right inset in Fig. 2b. Therefore, the corresponding part of the averaged magnetization curve is slanted, see top-right inset in Fig. 2b, gradually turning into vertical when  $L \rightarrow \infty$ , cf. right inset in Fig. 2a. On the other hand, for finite systems in the supercritical domain of disorder, both single-run magnetization curves and their averaged counterparts, exemplified in the right inset of Fig. 2c, are smooth functions of the external field  $H$ .

Averaged magnetizations and magnetic susceptibility curves for finite systems of lattice size  $L$ , according to [27,108], follow the scaling forms

$$M_{R,L}(H) = |r|^\beta \widetilde{\mathcal{M}}(\hat{h}_R^{\text{eff}}/|r|^{\beta\delta}, 1/L|r|^\nu), \quad (12)$$

$$\chi_{R,L}(H) = |r|^{\beta-\beta\delta} \widetilde{\mathcal{X}}(\hat{h}_R^{\text{eff}}/|r|^{\beta\delta}, 1/L|r|^\nu), \quad (13)$$

where  $\hat{h}_R^{\text{eff}} = H - H_c^{\text{eff}}(R)$  is the effective reduced magnetic field, measuring the shift of the data along the  $H$ -axis by the value of the effective critical field  $H_c^{\text{eff}}(R)$  pinpointing the pertinent susceptibility maxima;  $M_c^{\text{eff}}(R) = M(H_c^{\text{eff}}(R))$  is the effective critical magnetization,  $\widetilde{\mathcal{M}}$  and  $\widetilde{\mathcal{X}}$  stand for the universal scaling function, different in each of the disorder domains, and  $\beta$ ,  $\beta\delta$  and  $\nu$  are the standard RFIM exponents [28]. Scaling collapses of averaged magnetizations and susceptibilities in all three domains of disorder, each having parameters  $L$ ,  $R$  chosen so that the value of  $L|r|^\nu$  is constant and allowing for the estimation of critical parameters and exponents as the best collapsing values (shown in Table 1), are presented in Fig. 2.

**Table 1:** Values of the universal critical exponents (first two rows) and the non-universal critical parameters (bottom row) for the adiabatically driven ZT NEQ RFIM at the equilateral cubic 3D lattices. The data is from Table 1, Reference [108]

$\beta$	$\beta\delta$	$\tau + \sigma\beta\delta$	$\sigma$	$\theta$	$\eta$	$1/\sigma\nu z$
$0.04 \pm 0.03$	$2.0 \pm 0.2$	$2.02 \pm 0.02$	$0.24 \pm 0.02$	$0.000 \pm 0.016$	$0.53 \pm 0.05$	$1.78 \pm 0.04$
$1/\nu$	$1/\sigma\nu$	$d + \beta/\nu$	$z$	$\alpha + \beta\delta/\nu z$	$\nu z$	$\zeta$
$0.70 \pm 0.02$	$2.99 \pm 0.05$	$3.05 \pm 0.01$	$1.70 \pm 0.05$	$2.75 \pm 0.10$	$2.4 \pm 0.1$	$1.4 \pm 0.1$
$R_c$	$H_c$	$M_c$	$b$	$b_h$	$c_h$	$c_m$
$2.16 \pm 0.02$	$1.435 \pm 0.003$	$0.30 \pm 0.12$	$0.30 \pm 0.06$	$0.867 \pm 0.006$	$1.255 \pm 0.007$	$20 \pm 2$

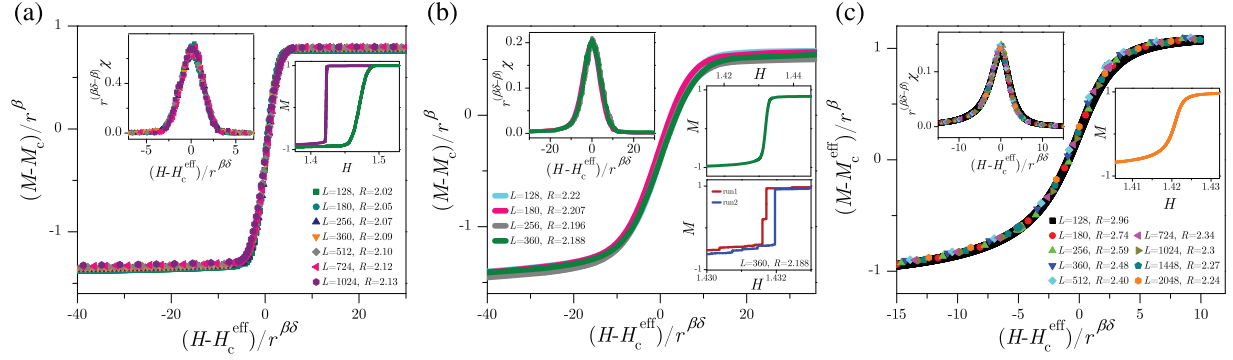


**Figure 2:** Main panels show the scaling collapses (12) of the averaged magnetization curves in the domains of disorder: (a) below critical, (b) transitional, between the critical and the effective critical, and (c) above the effective critical disorder, for a constant value of  $L|r|^\nu$  and the values of critical exponents and parameters presented in Table 1. The corresponding left insets show the collapses (13) of the averaged magnetic susceptibility curves, while the right insets show examples of the averaged magnetization curves. Bottom-right inset of panel (b) shows magnetization jumps in the two single-run magnetization curves, illustrating that more than one spanning avalanche (together with the associated  $H_{sp}$ -values) may appear in a single run. Presented data are replotted from Reference [108], combining parts of Figs. 6, 8 and 9

The distributions of avalanche parameters are cutoff-ending power-laws of the distributed parameter which depend on the underlying values of disorder  $R$  and lattice size  $L$ . Considered as the generalized homogeneous functions of their arguments, these distributions should follow finite-size scaling predictions in three equivalent forms, two of which, for the integrated size distributions and according to [27,108], read

$$D_S^{(\text{int})}(S; R, L) = L^{-\tau'/\sigma\nu} \tilde{D}_{S\pm}(S/L^{1/\sigma\nu}, 1/L|r|^\nu), \quad (14)$$

and

$$D_S^{(\text{int})}(S; R, L) = S^{-\tau'} \mathcal{D}_{S\pm}(S^\sigma|r|, 1/L^{1/\nu}|r|), \quad (15)$$

where  $\tau'$  is the pertinent critical exponent of the integrated distribution of avalanche size,  $\tau' = \tau + \sigma\beta\delta$ , and  $\sigma$  is the cutoff exponent describing the scaling  $S_{\max} \propto |r|^{-1/\sigma}$  [28]. These forms should hold in all domains of disorder, with the domain-specific universal scaling functions  $\tilde{D}_{S\pm}$  and  $\mathcal{D}_{S\pm}$ , predicting data collapsing for any set of size distributions satisfying the condition  $L^{1/\nu}r = \text{const}$ . The results of numerical simulations [108] supported the preceding scaling conjectures in the supercritical domain of disorder, as is illustrated in Fig. 3a by the data collapsing (14) in the left, and (15) in the right inset. Additionally, these simulations also showed that the  $D_S^{(\text{int})}(S; R, L)$  distributions become almost  $L$ -independent for  $R > R_c^{\text{eff}}(L) + W(L)$ , see Fig. 3b, meaning that they obey the scaling

$$D_S^{(\text{int})}(S; R) = S^{-\tau'} \mathcal{D}_\infty(S^\sigma|r|), \quad (16)$$

for infinite systems, following from (15) in the  $L \rightarrow \infty$  limit, and similarly for magnetization and susceptibility

$$M_R(H) = |r|^\beta \tilde{\mathcal{M}}_\infty(\hat{h}_R^{\text{eff}}/|r|^{\beta\delta}), \quad (17)$$

$$\chi_R(H) = |r|^{\beta-\beta\delta} \tilde{\mathcal{X}}_\infty(\hat{h}_R^{\text{eff}}/|r|^{\beta\delta}), \quad (18)$$

following from (12) and (13).

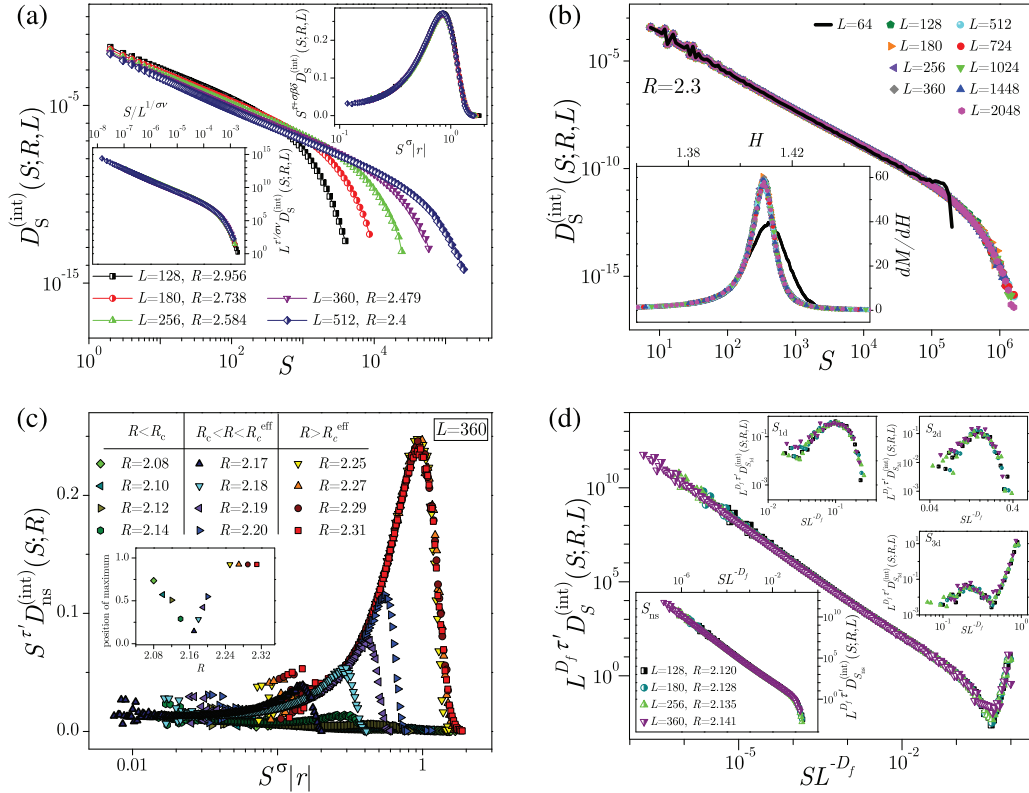


**Figure 3:** (a) Presented integrated size distributions are all from the supercritical domain of disorder and correspond to the  $(L, R)$  pairs from the legend satisfying the condition  $Lr^\nu = \text{const}$ . While the main part of this panel shows the original distributions, the left inset shows their scaling collapse according to (14), and right inset according to (15). (b) Integrated distributions  $D_S^{(\text{int})}(S; R, L)$  of avalanche size  $S$  in the main panel are obtained for several values of  $L$  quoted in legend and the same disorder  $R = 2.3$  surpassing  $R^{\text{eff}}(L) + W(L)$  for  $L \geq 128$ , except for  $L = 64$ . Thus, being in the supercritical domain, all  $L \geq 128$  distributions mutually overlap, while the case  $L = 64$  manifests a bump before the large- $S$  cutoff due to the presence of spanning avalanches. Inset illustrates the same effect for the susceptibility curves  $dM/dH$ . (c) Attempts to collapse the integrated size distributions of nonspanning avalanches using (16) for the system with size  $L = 360$  in a broad disorder range encompassing all three domains. Collapsing is successful only in the supercritical domain, while in the remaining two domains it is possible only for the  $(L, R)$  parameters satisfying  $L|r|^\nu = \text{const}$ . The pertinent inset illustrates that the  $R$ -dependent position on the  $S^\sigma|r|$ -scale of the maximum of the scaled distribution  $S^\tau D_{\text{ns}}^{(\text{int})}(S; R)$  attains its minimum value at  $R = R_c$  and saturates to 1 in the supercritical domain. (d) The main panel shows the collapsing (14) of the integrated size distributions  $D_{S_{\text{all}}}^{(\text{int})}$  of all avalanches for disorders from the subcritical domain, left inset shows the collapsing (19) of  $D_{S_{\text{ns}}}^{(\text{int})}$  for the nonspanning avalanches, and right insets the collapsing (20) of various types of integrated size distributions  $D_{S_{1d}}^{(\text{int})}$ ,  $D_{S_{2d}}^{(\text{int})}$ , and  $D_{S_{3d}}^{(\text{int})}$  for the spanning avalanches of type  $S_{1d}$ ,  $S_{2d}$ , and  $S_{3d}$ , respectively; the distributions correspond to the  $(L, R)$  pairs from the legend satisfying  $Lr^\nu = \text{const}$ , and all collapses are obtained for  $\tau' = \tau + \sigma\beta\delta = 2.03$  and fractal dimension  $D_f = 2.98$ . Presented data are replotted from Reference [108], combining parts of Figs. 3, 10, 12 and 14

On the other hand, according to the same Reference [108], in the subcritical and transitional domains of disorder, the  $L$ -independent scaling (16) is violated, while the  $L$ -dependent scaling conjectures (14) and (15) remain in effect, see Fig. 3c. In the main part of Fig. 3d we illustrate the collapsing (14) in the subcritical disorder domain of the integrated size distribution of all avalanches  $D_{S_{\text{all}}}^{(\text{int})} = D_{S_{\text{ns}}}^{(\text{int})} + \sum_{\alpha_{\text{sp}}=1}^3 D_{S_{\alpha_{\text{sp}}}}^{(\text{int})}$ , where  $D_{S_{\text{ns}}}^{(\text{int})}(S; R, L)$  is the integrated size distribution of nonspanning avalanches, and  $D_{S_{\alpha_{\text{sp}}}}^{(\text{int})}(S; R, L)$  are the integrated size distributions of 1d, 2d, and 3d types of spanning avalanches (i.e.,  $\alpha_{\text{sp}} = 1, 2, 3$ ). These distributions follow the scaling

$$D_{S_{\text{ns}}}^{(\text{int})}(S; R, L) = L^{-D_f \tau'} \tilde{\mathcal{G}}_{S_{\text{ns}}}^{(\text{int})}(SL^{-D_f}, |r|L^{1/\nu}), \quad (19)$$

and

$$D_{S_{\alpha_{\text{sp}}}}^{(\text{int})}(S; R, L) = L^{-D_f \tau'} \tilde{\mathcal{G}}_{S_{\alpha_{\text{sp}}}}^{(\text{int})}(SL^{-D_f}, |r|L^{1/\nu}), \quad (20)$$

predicting their collapsing when  $L^{1/\nu}|r| = \text{const}$ ; here,  $D_f = 2.98$  is the common value of fractal dimension providing the best distributions' collapsing for all spanning and nonspanning avalanches [108], predicted in [48] to be  $D_f = 1/\sigma\nu$ . Qualitatively similar behavior holds for the distributions of the remaining avalanche parameters (duration, energy and amplitude).

The integrated correlation functions, measuring the probability per spin that flipping of the spin initiating the avalanche will cause the flipping of spins at the distance  $x$  away within the same avalanche, scale as [28,31].

$$G_R^{(\text{int})}(x) \sim \frac{1}{x^{d+\beta/\nu}} \tilde{\mathcal{G}}_{\pm}(x|r|^{\nu}). \quad (21)$$

Here  $d$  is the system dimension, and  $\nu$  stands for the correlation length exponent describing the divergence of the correlation length  $\xi \sim |r|^{-\nu}$  when  $r \rightarrow 0$ , presented in panel (d) of Fig. 4. In the supercritical disorder domain, correlation functions are monotonically decreasing with the inter-spin distance  $x$  in the cutoff region, while in the remaining domains, the onset of spanning avalanches causes the occurrence of characteristic bumps, as is displayed in the main panels (a)–(c) of Fig. 4. Scaling collapses of integrated correlation functions, satisfying the condition  $|r|L^{1/\nu} = \text{const}$ , are shown in pertinent insets.

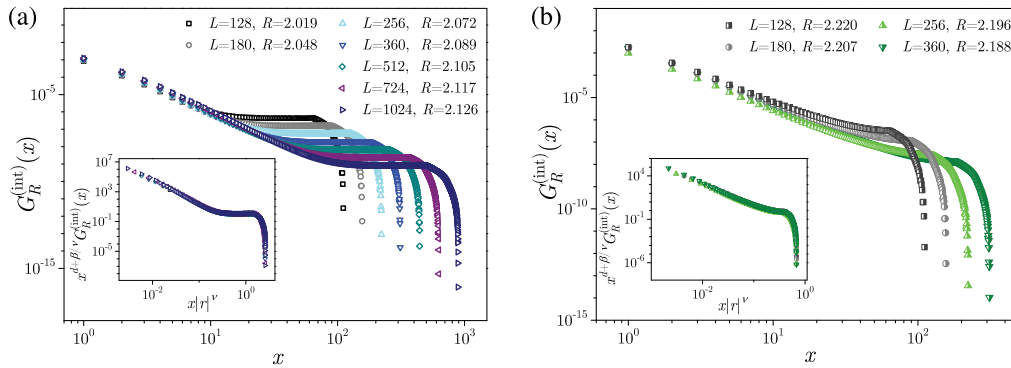
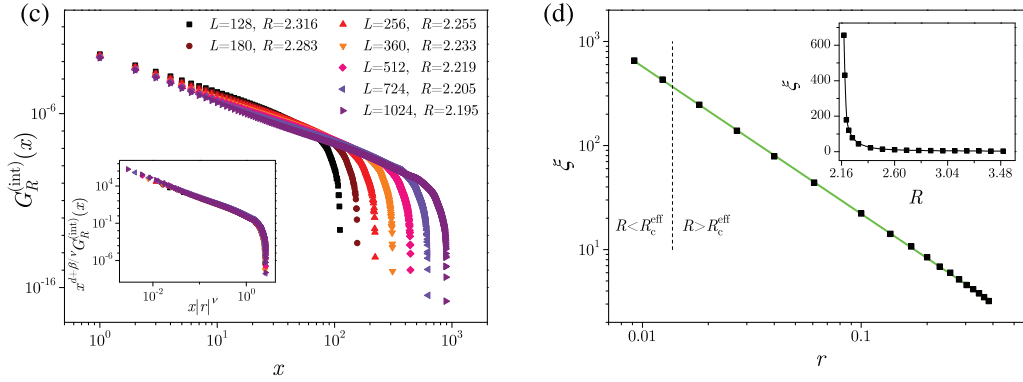


Figure 4: (Continued)



**Figure 4:** Integrated correlation functions  $G_R^{(int)}(x)$  vs. inter-spin distance  $x$  shown in the main panels, and the pertinent collapses (21) shown in the insets in all three disorder domains, subcritical in (a), transitional in (b), and supercritical in (c). Divergence of the correlation length  $\xi$  when  $r \rightarrow 0$ , that is when  $R \rightarrow (R_c)^+$ , is displayed in panel (d) on the log-log scale in the main panel part, and on the lin-lin scale in the inset. Presented data are replotted from Reference [108], combining part of Fig. 15 and Fig. 17

#### 4.2 Adiabatically Driven ZT NEQ RFIM on Two-Dimensional (2D) Lattices

The question of whether the adiabatically driven ZT NEQ RFIM on 2D quadratic lattices exhibits nontrivial critical behavior remained open for almost 20 years. This puzzle was initiated by the Mermin-Wagner theorem [174] which proved the absence of coexistence of two ferromagnetically ordered phases in isotropic Heisenberg models [175] in  $d \leq 2$  dimensions. After that, the existence of two phases at low temperatures in 3D RFIM has been established in [92] using an exact renormalization-group (RG) flow down to the zero-temperature zero-field fixed point. Next, in 1989 the existence of an ordered phase at finite temperatures and weak fields for EQ RFIM in 3D was demonstrated, while in 2D it was rigorously proved that the ferromagnetic ordering is absent in the thermodynamic limit [91, 176]. Additionally, many similarities between the EQ [86, 177–179] and NEQ ZT RFIM [27, 106] were observed regarding their criticality (matching of exponents, scaling functions, and spatial structures of avalanches), including the studies of four-dimensional systems [180] and at and beyond the upper critical dimension [181, 182], leading to the conclusion that both models are rather likely to be in the same universality class for  $d \geq 3$  dimensions [87, 88]. Although not obtained for the NEQ model, these findings suggested that infinite 2D systems in the NEQ model may also lack ferromagnetic ordering because the two phases, evidenced in finite 2D systems, might vanish in the thermodynamic limit, i.e., when the system becomes big enough. The question of how large the NEQ system should be to lose/retain two ferromagnetically ordered phases was addressed in [183] where it was shown that the two phases ‘survive’ the thermodynamic limit provided they exist in 2D systems with size greater than the ‘breakup length’  $L_b \approx \exp(A/R^2)$  with  $A = 2.1 \pm 0.2$  for the Gaussian distribution of the random magnetic field having disorder  $R$ .

Complementary to the preceding theoretical issues stood the question of whether the real 2D disordered ferromagnetic samples exhibit critical behavior until being experimentally confirmed in studies [184, 185], opening a wide venue for further fundamental experimental and theoretical investigations of the 2D disordered ferromagnets and their applications.

#### 4.2.1 The Case of Quadratic Lattices

Numerical simulations reported in [89,90], performed for the system sizes up to  $L = 131072$ , significantly exceeding the ‘breakup length’  $L_b$  and having up to  $\approx 1.7 \times 10^{10}$  spins, provided a numerical evidence for the critical behavior of the adiabatically driven ZT NEQ RFIM on the 2D quadratic lattices. The values of the non-universal critical parameters and of the universal critical exponents, obtained in [89,90], are quoted in Table 2 including the value of critical disorder  $R_c = 0.54$  corroborated in Fig. 5 implying  $L_b \approx 10^4$ .

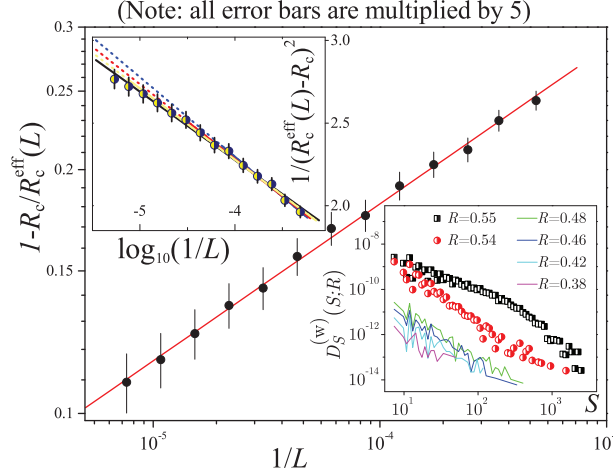


**Figure 5:** Effective critical disorder  $R_c^{\text{eff}}(L)$  vs. system size  $L$  (symbols) and the power-law prediction  $[R_c^{\text{eff}}(L) - R_c]/R_c^{\text{eff}}(L) \sim L^{-1/\nu}$  (continuous line) with  $R_c = 0.54$  and  $\nu = 5.14$ . Top inset shows Bray-Moore scaling  $\xi \sim \exp[\tilde{a}/[R_c^{\text{eff}}(L) - R_c]^2]$ ,  $R_c \sim 0$ ; see [186]. Bottom inset presents the windowed size distributions for  $R = 0.38$  to  $0.55$ ,  $L = 65,536$ , and more than 600 RFC for each  $R$ . Their shapes in the bottom inset indicate the onset of spanning avalanches for  $R \leq 0.54$ . This is Fig. 6 from [89]

**Table 2:** The values of the non-universal critical parameters (top part) and of universal critical exponents (bottom part) for the 2D ZT NEQ RFIM on quadratic lattices (presented in Table 1 in [89]). The quoted errors are based on the (200 runs) Monte-Carlo estimation and statistical uncertainties of the underlying data [187]

$R_c$	$H_c$	$M_c$	$b$
$0.54 \pm 0.02$	$1.275 \pm 0.020$	$0.00 \pm 0.01$	$0.24 \pm 0.04$
$\beta$	$\beta\delta$	$\tau$	$\tau + \sigma\beta\delta$
$0.15 \pm 0.04$	$4.8 \pm 0.2$	$1.54 \pm 0.05$	$2.02 \pm 0.06$
$\sigma$	$\nu$	$d + \beta/\nu$	$\eta$
$0.10 \pm 0.01$	$5.15 \pm 0.20$	$2.04 \pm 0.03$	$1.05 \pm 0.06$

In Fig. 6a, we presented (the rising part of) the magnetization curves  $M(H)$  obtained in [89,90] for the system size  $L = 131,072$  and several values of disorder, ranging from  $R = 0.52$  (which is below the critical disorder  $R_c = 0.54$ ) up to  $R = 0.76$  surpassing the effective critical disorder  $R_c^{\text{eff}}(L)$  ( $= 0.605$  for  $L = 131,072$ ). Due large value of  $L$ , one can take that the  $M(H)$  curves for disorder above

the effective critical disorder  $R_c^{\text{eff}}(L)$  obey the scaling

$$M_{R,L}(H) = |r|^\beta \widetilde{\mathcal{M}}(\hat{h}_R^{\text{eff}}/|r|^{\beta\delta}), \quad (22)$$

which follows from (12) in the  $L \rightarrow \infty$  limit, and analogously for the susceptibility curves

$$\chi_{R,L}(H) = |r|^{\beta-\beta\delta} \widetilde{\mathcal{X}}(\hat{h}_R^{\text{eff}}/|r|^{\beta\delta}), \quad (23)$$

and Eq. (13). The collapsing of  $M(H)$  curves according to (22) is presented in the main panel of Fig. 6b, and collapsing for the susceptibility curves and Eq. (23) in the inset. Besides, the distributions of avalanche parameters also indicate criticality by manifesting the power-law shapes. Thus, in Fig. 7 we show the distributions of size and duration in panels (a) and (b), respectively. In the bottom inset of panel (a) presented are the integrated size distributions for the five values of  $L$  and the corresponding effective critical disorder  $R_c^{\text{eff}}(L)$ . The collapsing for  $R > R_c^{\text{eff}}(L)$  size distributions according to

$$D_S^{(\text{int})}(S; R) = S^{-(\tau+\sigma\beta\delta)} \mathcal{D}(S^\sigma |r|), \quad (24)$$

following from Eq. (15) in the  $L \rightarrow \infty$  limit, is presented in the main part of panel (a). Although the  $D_S^{(\text{int})}(S; R)$  curves collapse well for large avalanches, they show a noticeable branching for small sizes, originating from the avalanches triggered near the end of the magnetization curve when almost all (except trapped) spins are already flipped, so that small avalanche sizes are more probable than Eq. (24) predicts. As the top inset shows, the branching disappears for the windowed distributions

$$D_S^{(\text{w})}(S; R) = \int_{H_c^{\text{eff}}+r^{\beta\delta}h'_0}^{H_c^{\text{eff}}-r^{\beta\delta}h'_0} D_S(S; R, H), \quad (25)$$

collected in complementary windows  $(-r^{\beta\delta}h'_0, r^{\beta\delta}h'_0)$  covering the central parts of magnetization curves where the scaling

$$D_S(S; R, H) = S^{-\tau} \mathcal{D}(S^\sigma |r|, h'|r|^{-\beta\delta}), \quad (26)$$

of the size distribution  $D_S(S; R, H)$  collected at the external field  $H$  applies, and  $h' = H - H_c - br$ ; for details, see [90]. As is illustrated in panel (b), analogous behavior is found for the duration distribution, as well as for the (here not shown) distributions of avalanche energy and amplitude; see [90] for the latter two and also for the joint distributions for pairs of avalanche parameters. Values of the corresponding exponents are quoted in Table 3.

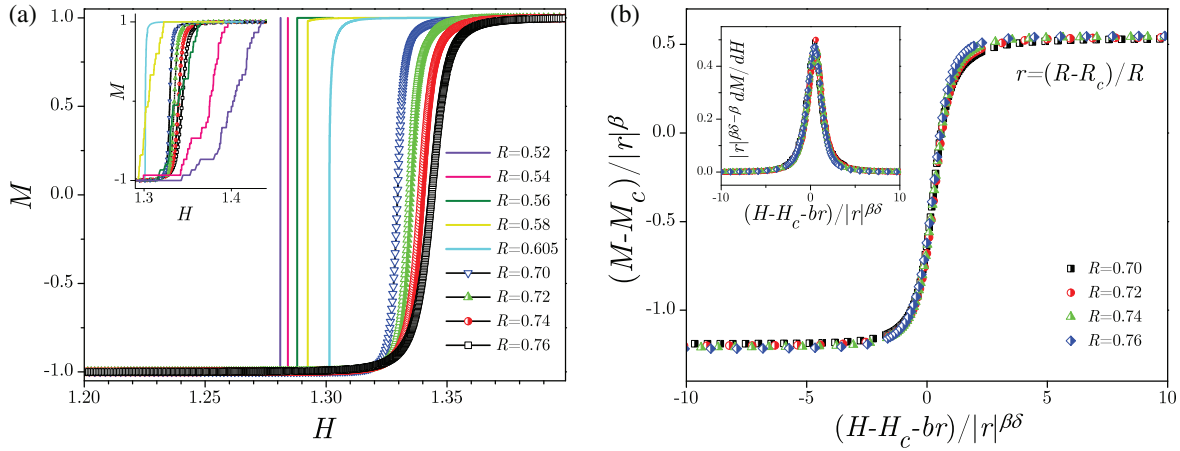


**Figure 6:** (a) Rising part of the magnetization curves  $M_R(H)$  for disorders  $R = 0.52 - 0.76$  and system size  $L = 131072$  where the effective critical disorder is  $R_c^{\text{eff}} = 0.605$ . For  $R < R_c^{\text{eff}}$ , the value  $H_{\text{sp}}$  of the external magnetic field at which the spanning avalanche occurs varies with the random field configuration (RFC). Main panel shows magnetization curves for single RFC sorted in increasing disorder  $R$ . Inset displays magnetization curves averaged over 30 RFC; while this number is small, visible are the steps appearing due to spanning avalanches and stochastic nature of  $H_{\text{sp}}$ . (b) Collapsing (22) of four magnetization curves and (23) of susceptibility curves  $\chi(H)$  are shown in the main panel and inset, respectively, for disorders  $R > R_c^{\text{eff}}$  from the legend. In this figure, combined are Figs. 1 and 2 from [89]

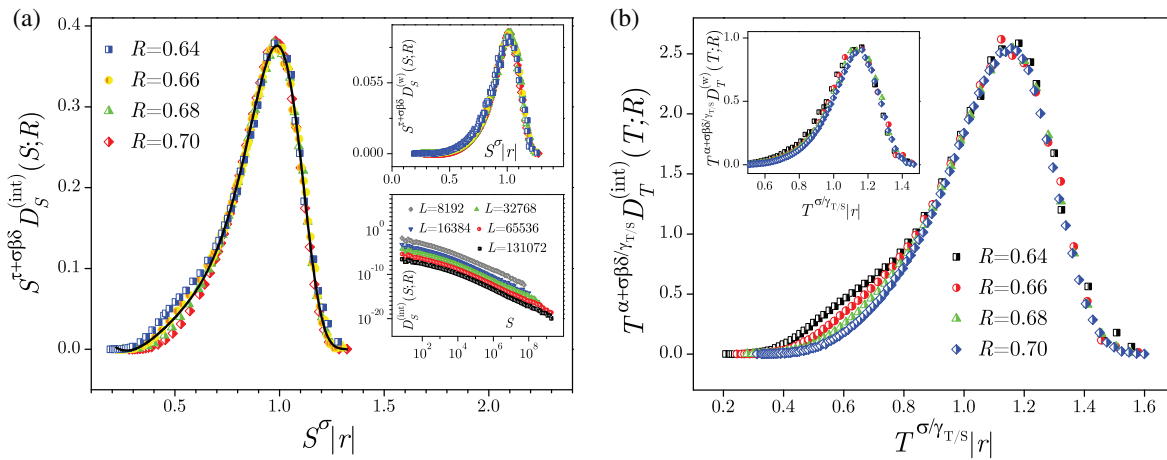


**Figure 7:** (a) The main panel shows the collapsing of the integrated distributions of avalanche size collected at  $R > R_c^{\text{eff}}$  for  $L = 65,536$ , top insets show the collapsing of the corresponding windowed distributions, whereas the bottom inset shows the (non-scaled) size distributions collected for the values of  $L$  quoted in the legend at the corresponding effective critical disorder  $R^{\text{eff}}(L)$ . (b) Main panel and inset like for (a), but for the duration distribution. The number of RFC used in quenched averaging of the data ranged between 30 for the largest and 8000 for the smallest  $L$ . In this figure, combined are Fig. 3 from [89] and Figs. 6 and 7 from [90]

**Table 3:** Universal critical exponents of distribution of avalanche duration ( $\alpha$ ), energy ( $\varepsilon$ ), and amplitude ( $\mu$ );  $\gamma_{T/S}$ ,  $\gamma_{E/S}$ , and  $\gamma_{A/S}$  are the duration/size, energy/size, and amplitude/size exponents, respectively. The values obtained from the scaling collapses, together with their uncertainties, are shown in the second column, and in the fourth column the values calculated using the scaling relations from the third column. Presented data are from Table III in [90]

Exponent	Measured value	Scaling relation	Scaling relation estimate
$\alpha$	$1.87 \pm 0.06$	$\alpha = 1 + (\tau - 1)/\sigma \nu z$	1.84
$\varepsilon$	$1.42 \pm 0.05$	$\varepsilon = 1 + (\tau - 1)/(2 - \sigma \nu z)$	1.40
$\mu$	$2.55 \pm 0.18$	$\mu = 1 + (\tau - 1)/(1 - \sigma \nu z)$	2.55
$\gamma_{T/S}$	$0.645 \pm 0.015$	$\gamma_{T/S} = \sigma \nu z$	–
$\gamma_{E/S}$	$1.35 \pm 0.04$	$\gamma_{E/S} = 2 - \sigma \nu z$	1.36
$\gamma_{A/S}$	$0.39 \pm 0.02$	$\gamma_{A/S} = 1 - \sigma \nu z$	0.36

The behavior of the correlation function  $G_R^{(\text{int})}(x)$  and the correlation length  $\xi(r, h')$ , depending on the reduced disorder  $r$  and reduced magnetic field  $h'$ , is presented in Fig. 8 for  $h' = 0$ . The data from the main part and the bottom inset of panel (a) show the divergence  $\xi \sim |r|^\nu$  of the correlation length  $\xi$  with the reduced disorder  $r$ , while the top inset shows the collapsing of the integrated correlation function  $G_R^{(\text{int})}(x)$  according to the scaling prediction

$$G_R^{(\text{int})}(x) \sim x^{-(d+\beta/\nu)} \mathcal{G}_\pm^{(\text{int})}(x|r|^\nu), \quad (27)$$

where  $x$  is the distance between the spins flipped in the same avalanche. Complementary, the panel (b) shows the collapsing of the correlation function  $G_{R,H}(x)$ , giving correlations at the external field  $H$ , which scales as

$$G_{R,H}(x) = \frac{1}{d-2+\eta} \mathcal{G}_\pm \left( \frac{x}{\xi(r, h')} \right), \quad (28)$$

where  $\eta$  is the exponent named anomalous dimension [28,31] (here,  $\eta = 1$ ).

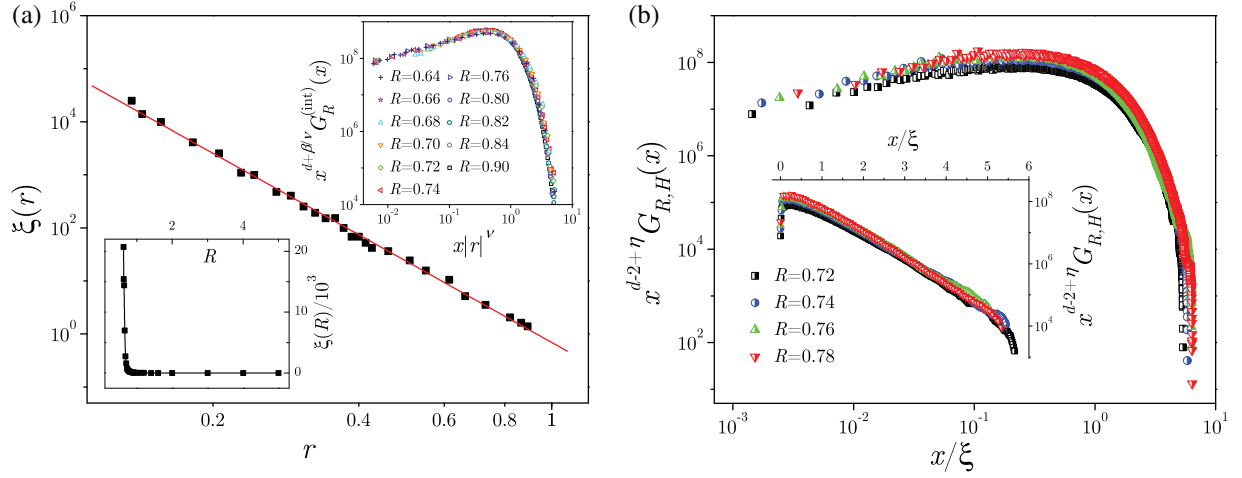


**Figure 8:** (a) The main part shows power-law divergence  $\xi \sim |r|^\nu$  of the correlation length  $\xi$  with reduced disorder  $r$  for reduced magnetic field  $h' = 0$ . In the bottom inset, the same data are shown against the disorder  $R$  on a linear scale. Top inset: scaling collapse (27) of the correlation function  $G_R^{(in)}(x)$  for disorders  $R = 0.64 - 0.90$  and system size  $L = 131,072$ . The curves are averages of 30 RFCs for each  $R$ . (b) The scaling collapse (28) of the correlation function  $G_{R,H}(x)$  for the avalanches at reduced field  $h' = 0$ . The collapse is obtained for  $\eta = 1$  and correlation lengths from the left panel. Inset: the same collapse on the lin–log scale illustrates the applicability of the approximation  $G_{R,H}(x) \sim \exp(x/\xi)/x^{d-2+\eta}$  which is used in determination of the correlation length  $\xi$ . In this figure are combined Figs. 4 and 5 from [89]

#### 4.2.2 Spanning Avalanches on Quadratic Lattices

Below the effective critical disorder  $R_c^{\text{eff}}(L)$ , system response is dominated by the spanning avalanches studied in [107] in the case of adiabatically driven ZT NEQ RFIM on 2D equilateral quadratic lattices. The number per single run,  $N_2(R, L)$ , of  $2d$  spanning avalanches (i.e., the avalanches that span the system along both dimensions), shown in Fig. 9a against  $R$  for lattice sizes  $L = 1024 - 16,384$ , scale as

$$N_2(R, L) = \tilde{N}_2(rL^{1/\nu}), \quad (29)$$

enabling their collapsing presented in the panel (b), and indicating that  $\lim_{L \rightarrow \infty} N_2(R, L) = U(R_c - R)$ , where  $U(x)$  is the unit step function. On the other hand, the number per single run  $N_1(R, L)$  of 1d spanning avalanches (spanning the system along only one dimension and shown in the inset of left panel) scales as

$$N_1(R, L) = L^{-\theta_1} \tilde{N}_1(rL^{1/\nu}), \quad (30)$$

with  $\theta_1 = 0.08 \pm 0.02$ , meaning that they become irrelevant in the  $L \rightarrow \infty$  limit. The number per single run  $N_{\text{ns}}(R, L)$  of the remaining (i.e., nonspanning) avalanches scales as

$$N_{\text{ns}}(R, L) = L^2 \tilde{N}_{\text{ns}}(rL^{1/\nu}), \quad (31)$$

and is presented in the inset of Fig. 9b. Due to scale invariance, the clusters of spins flipped during a spanning avalanche are fractals; their fractal dimension  $D_f$  is smaller for 1d than for the 2d spanning avalanches as is illustrated in Fig. 10.

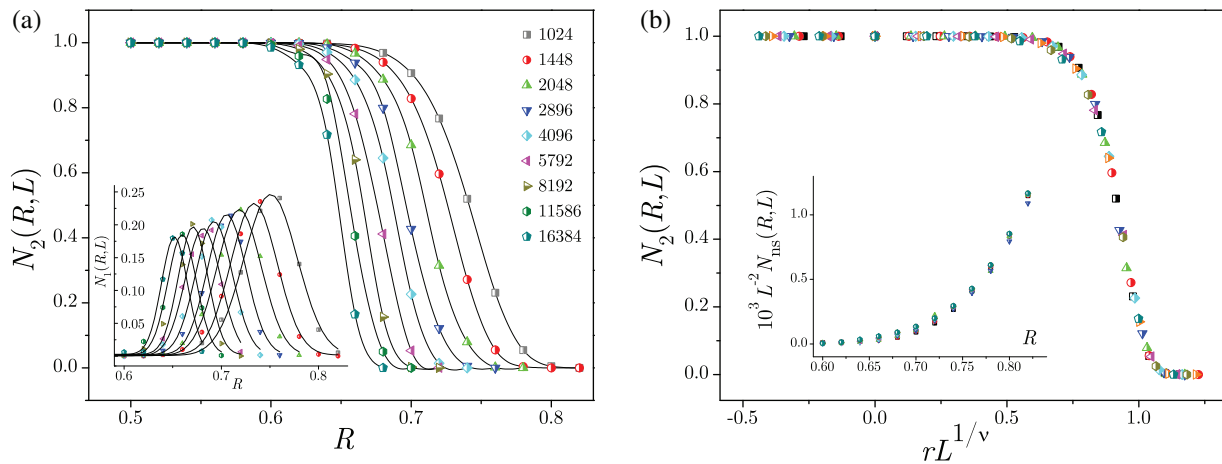


**Figure 9:** (a) Main part and inset show the number of spanning avalanches per single run,  $N_2(R, L)$  for 2d and  $N_1(R, L)$  for 1d spanning avalanches, respectively, against disorder  $R$  for the system sizes  $L$  quoted in legend. (b) Collapsing (29) of 2d spanning and (31) of nonspanning avalanches shown in the main part and inset, respectively. In this figure, combined are Figs. 2, 4, 5 and 13 from [107]

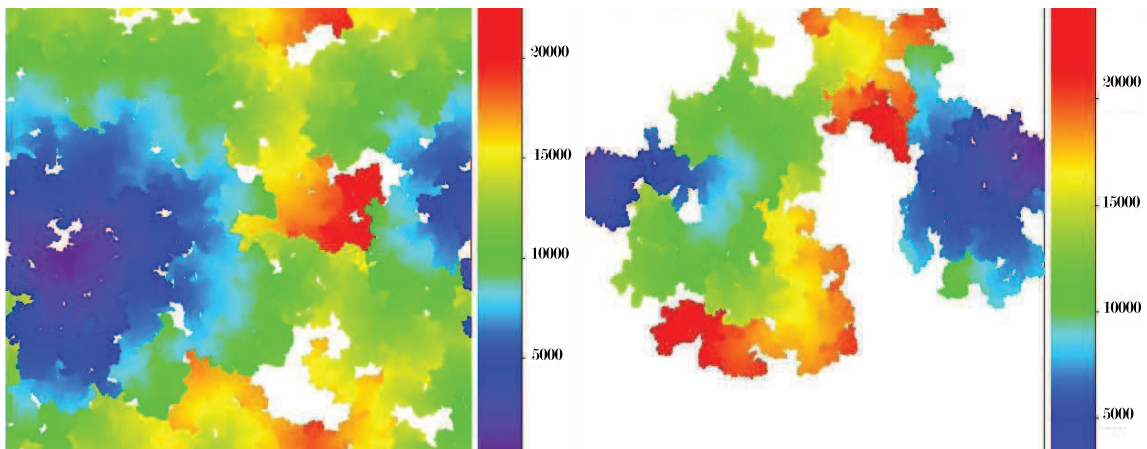


**Figure 10:** Plots of a 2d spanning avalanche (left) and a 1d spanning avalanche (right) for  $L = 4096$  and  $R = 0.68$  [107]; the time scale of spin flipping is shown by the color legend; not affected spins are white. Fractal dimensions are:  $D_f = 1.9828$  for the 2d spanning avalanche, and  $D_f = 1.9125$  for the 1d spanning avalanche. Presented figure is replotted from Figs. 7 and 8 from Reference [107]

Spanning avalanches cause bumps in distributions and jumps in magnetization  $\Delta M$  realized at some value of the external field  $H_{\text{sp}}$ , called the spanning field, whose distribution is determined by the RFC. This is shown in [107] and illustrated in Fig. 11.

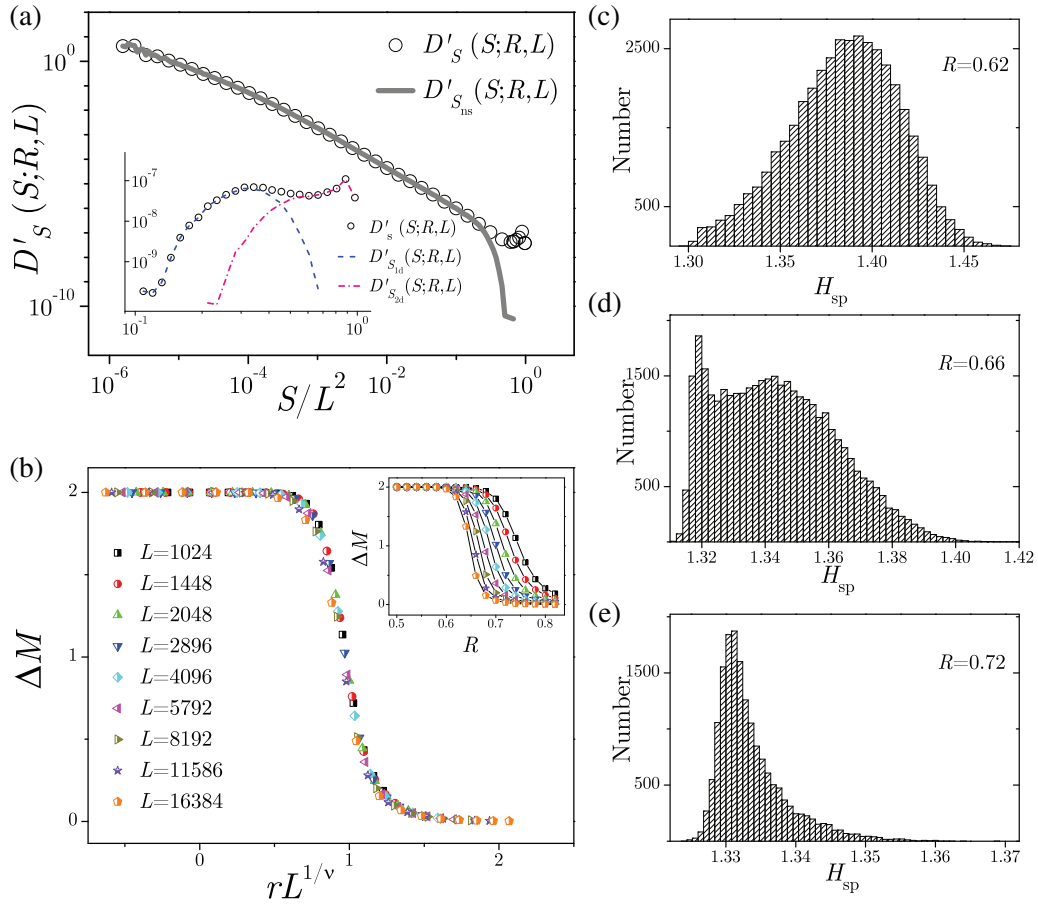


**Figure 11:** (a) (Scaled) size distributions of all avalanches (circles), nonspanning avalanches (full line), and spanning avalanches in the inset. (b) Magnetization jumps  $\Delta M$  shown in inset, and their collapsing in the main panel. (c)–(e) Distribution of spanning field  $H_{sp}$  for three different values of disorder  $R$ ; for details, see [107]. In this figure, combined are Figs. 14, 18 and 19 from [107]

#### 4.2.3 The Case of Triangular and Hexagonal Lattices

Besides quadratic, the ZT NEQ RFIM can be studied on other 2D lattices with translation symmetry, but with different topology of elementary cell, e.g., with different number of nearest neighbors given by the coordination number  $z_m$ . Two examples are the triangular and hexagonal lattices which, compared to quadratic lattice with four nearest neighbors, have six and three nearest neighbors for each spin, respectively; see Fig. 12.

The studies [100] on triangular and [103] on hexagonal lattices gave partial answers to the conjecture introduced in [135] that the coordination number  $z_m$ , and not solely the lattice dimension (as believed beforehand), plays the key role in determining the universality class of the ZT NEQ RFIM critical behavior. Thus, the study [100] showed that the ZT NEQ RFIM exhibit critical behavior on the triangular lattices (where  $z_m = 6$ ) in accordance with the general expectation that this should be the case for the lattices with  $z_m \geq 4$ . However, the values of some critical exponents and nonuniversal critical parameters reported for this lattice, see in Table 4, differ outside the error bars from the

corresponding ones reported in [89,90] for the quadratic lattices, suggesting that the universality classes for the triangular and quadratic lattices might be different. As an illustration of the critical behavior of the model on triangular lattice, in Fig. 13, we show the graph of  $R_c^{\text{eff}}(L)$  vs.  $L$ , implying that  $R_c = 0.86$  for the triangular lattice (left panel), and the collapsing of the windowed size distributions (right panel) obtained for the exponents from Table 4. Similar study [103] revealed the absence of critical behavior on the hexagonal lattice having  $z_{\text{nm}} = 3$ .

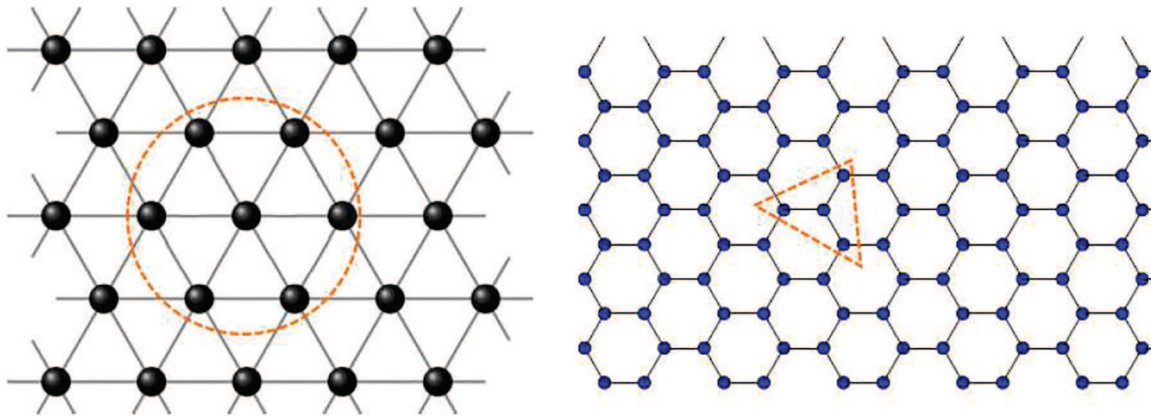


**Figure 12:** Triangular (left) and hexagonal (right) lattices. The right panel is Fig. 1 from [103]

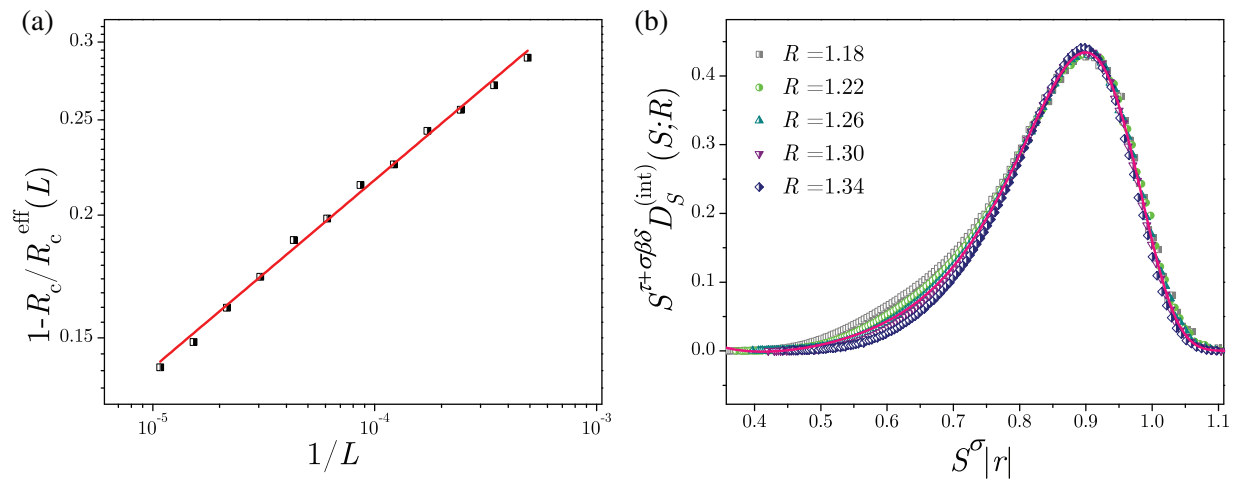


**Figure 13:** (a) Effective critical disorder  $R_c^{\text{eff}}(L)$  for the triangular lattice vs. system size  $L$  (symbols), and the power-law prediction  $[1 - R_c/R_c^{\text{eff}}(L)] \sim L^{1/\nu}$  (straight line) for  $R_c = 0.86$  and  $\nu = 5.26$ . (b) The scaling collapse of the integrated distributions of avalanche size for triangular lattice with  $L = 65,536$ . In this figure are combined Figs. 2 and 8 from [100]

**Table 4:** Critical exponents for the ZT NEQ RFIM on triangular lattice (published in Table 1 in [100]; the values obtained on 2D square lattice [89,90] are in parentheses, and are given for the sake of comparison

$\beta$	$\beta\delta$	$\tau$	$\tau + \sigma\beta\delta$	$\sigma$
$0.13 \pm 0.03$ ( $0.15 \pm 0.04$ )	$5.2 \pm 0.2$ ( $4.8 \pm 0.2$ )	$1.64 \pm 0.05$ ( $1.54 \pm 0.05$ )	$2.05 \pm 0.06$ ( $2.02 \pm 0.06$ )	$0.063 \pm 0.012$ ( $0.10 \pm 0.01$ )
$\nu$	$1/\sigma\nu z$	$\alpha$	$\alpha + \sigma\beta\delta/\sigma\nu z$	$z$
$5.25 \pm 0.20$ ( $5.15 \pm 0.20$ )	$1.65 \pm 0.01$ ( $1.55 \pm 0.02$ )	$2.05 \pm 0.06$ ( $1.87 \pm 0.06$ )	$2.70 \pm 0.05$ ( $2.65 \pm 0.05$ )	$1.83 \pm 0.18$ ( $1.25 \pm 0.17$ )

### 4.3 Crossover from 3D to 2D ZT NEQ RFIM Systems

The dimensional crossover from three to two spatial dimensions has been studied so far both experimentally [22,188] and in equilibrium models [189–192], where it has been established that the systems with constant thickness  $l$ , and two diverging spatial dimensions  $L \rightarrow \infty$ , behave in the asymptotic limit essentially as 2D systems, showing a critical temperature  $T_c(l)$  that shifts from the critical temperature of the planar 2D system,  $T_c(l=1) = T_c^{2D}$ , to the critical temperature of the bulk 3D system,  $T_c(l \rightarrow \infty) = T_c^{3D}$ , with a first approximation for this crossover function  $T_c(l) - T_c^{3D} \sim l^{-1/\nu_{3D}}$  for large  $l$ , where  $\nu_{3D}$  is the correlation length exponent in the 3D case.

The 3D to 2D dimensional crossover in ZT NEQ RFIM was studied in [110–112] on nonequilateral 3D  $L \times L \times l$  cubic lattices with quadratic  $L \times L$  base and thickness  $l$  in adiabatic regime with closed boundary conditions on base, and open conditions on thickness. For each  $l$ , one can define the critical disorder  $R_c(l)$  for infinite (i.e.,  $L \rightarrow \infty$ ) systems as the value of disorder such that for  $R < R_c(l)$  there is a finite jump  $\Delta M$  in the magnetization curve  $M(H)$  tending to zero when  $R$  tends to  $R_c(l)$ . Additionally, for  $R > R_c(l)$  the curve  $M(H)$  is smooth and has finite susceptibility  $\chi(H) = dM/dH$  for any  $H$ , while at  $R = R_c(l)$  the  $M(H)$  curve is still smooth but with infinite susceptibility at some value  $H_c(l)$  of the external magnetic field, called the *critical field* for the infinite lattices of thickness  $l$ . In finite  $L \times L \times l$  systems the biggest change in magnetization, and therefore the maximum value of susceptibility, is caused by the spanning avalanches which (roughly speaking) appear at disorders  $R \leq R_c^{\text{eff}}(l, L)$ , where  $R_c^{\text{eff}}(l, L)$  is the effective critical disorder (for given thickness  $l$  and base size  $L$ ) which tends to  $R_c(l)$  in the  $L \rightarrow \infty$  limit. At  $R = R_c^{\text{eff}}(l, L)$  the susceptibility attains its maximum value at the value  $H_c^{\text{eff}}(l, L)$  of the external field called the *effective critical field* which tends to  $H_c(l)$  in the  $L \rightarrow \infty$  limit. The analyses in [110] resulted in the analytical prediction

$$R_c^{\text{th}}(l, L) = R_c^{3D} \left[ 1 - \frac{\Delta}{l^{1/\nu_{3D}}} - \frac{(A - \Delta)l^{1/\nu_{2D}}}{L^{1/\nu_{2D}}l^{1/\nu_{3D}}} \right]^{-1}, \quad (32)$$

for the effective critical disorder  $R_c^{\text{eff}}(l, L)$ ; here  $A = 0.63 \pm 0.18$  is an adjustable parameter,  $\Delta = 1 - R_c^{3D}/R_c^{2D}$ , while  $\nu_{3D}$  and  $R_c^{3D}$  are the correlation length exponent and critical disorder in 3D model (and analogously for  $\nu_{2D}$  and  $R_c^{2D}$  and 2D model), see Eq. (7) in [110]. Extension of this analysis, presented in [112], led to

$$H_c^{\text{th}}(l, L) = H_c^{3D} + \frac{\Theta_{\text{cross}}}{l^{1/\nu_{3D}}} + \frac{B - \Theta_{\text{cross}}}{l^{1/\nu_{3D}}} \left( \frac{l}{L} \right)^{1/\nu_{2D}} \quad (33)$$

predicting the effective magnetic field  $H_c^{\text{eff}}(l, L)$ , where  $B = 0.20 \pm 0.07$ ,  $\Theta_{\text{cross}} = 0.68 \pm 0.07$ , and  $H_c^{3D}$  is the critical field in 3D model. From (32) and (33) follow the expressions

$$R_c^{\text{th}}(l) = R_c^{3D} \left[ 1 - \frac{\Delta}{l^{1/\nu 3D}} \right], \quad (34)$$

$$H_c^{\text{th}}(l) = H_c^{3D} + \frac{\Theta_{\text{cross}}}{l^{1/\nu 3D}}, \quad (35)$$

for  $R_c(l)$  and  $H_c(l)$  in the  $L \rightarrow \infty$  limit that agree with the simulational values as is illustrated in Fig. 14.

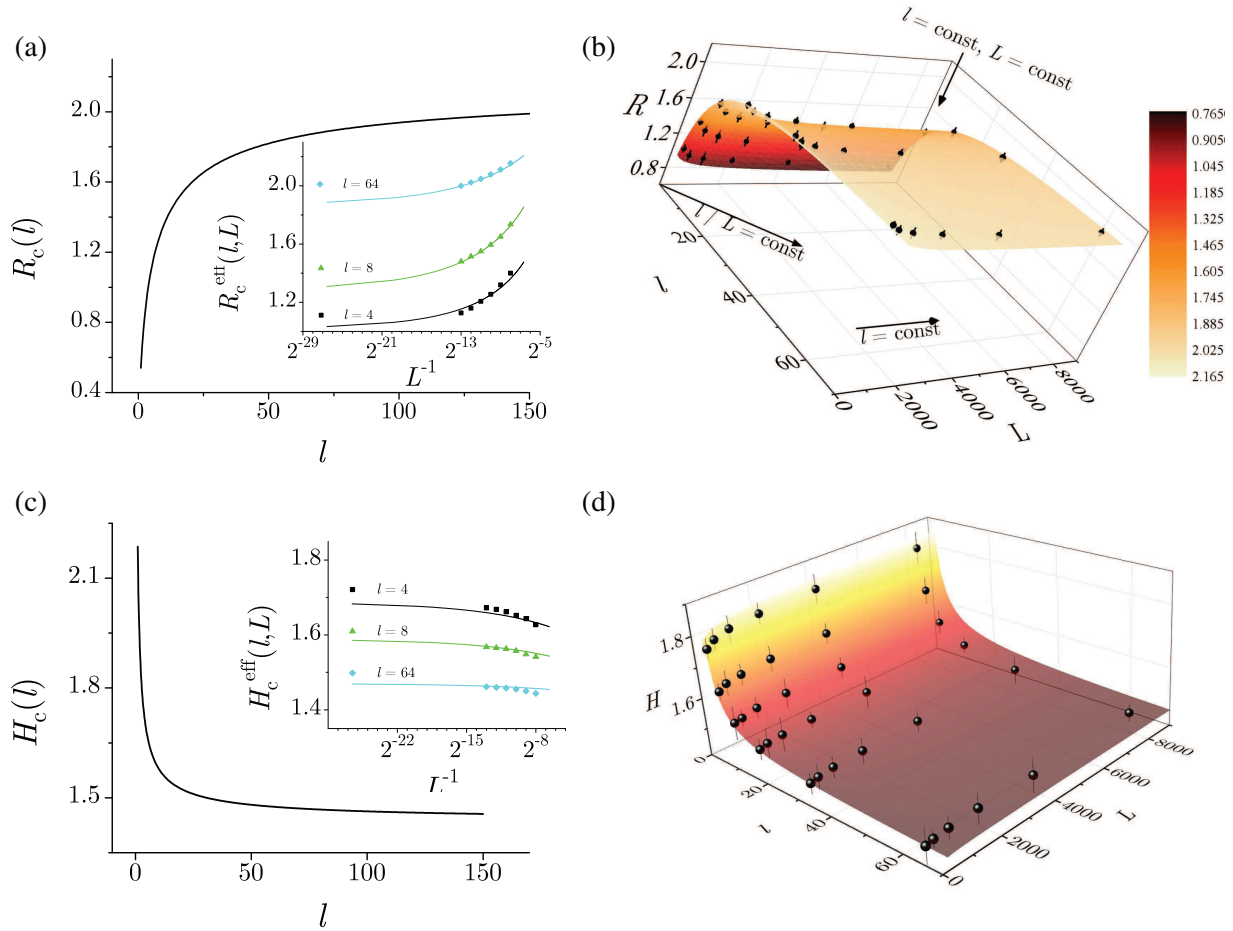


**Figure 14:** (a) Full line in the main left panel shows the  $R_c(l)$  vs.  $l$  prediction (34), while in its inset the  $R_c^{\text{eff}}(l, L)$  vs.  $L^{-1}$  data are presented by the full lines for the prediction (34) and by symbols for the simulational data; (b) panel shows the 3D plot of the surface (32) and the simulational data (symbols) with 0.01 maximum residual from the surface. (c) The same as in (a), but for  $H_c(l)$ ,  $H_c^{\text{eff}}(l, L)$ , prediction (35), and surface (33) in panel (d). Compiled from Fig. 2 in [110], and Figs. 3 and 9 from [112]

In Fig. 15, we show the integrated size distributions collapsed according to three types of scaling

$$D_S^{(\text{int})}(S; r, 1/L, 1/L, 1/l) = l^{-(\tau+\sigma\beta\delta)D_f} \times D_S^{(\text{int})}(S/l^{D_f}; r l^{1/\nu}, l/L, l/L, 1), \quad (36)$$

$$D_S^{(\text{int})}(S; r, 1/L, 1/L, 1/l) = L^{-(\tau+\sigma\beta\delta)D_f} \times D_S^{(\text{int})}(S/L^{D_f}; r L^{1/\nu}, 1, 1, L/l). \quad (37)$$

$$D_S^{(\text{int})}(S; r, 1/L, 1/L, 1/l) = S^{-(\tau+\sigma\beta\delta)} \times \tilde{\mathcal{D}}_{\pm}^{(\text{int})}(S^{\sigma}|r|, S^{\sigma v}/L, S^{\sigma v}/L, S^{\sigma v}/l), \quad (38)$$

predicted for  $L \times L \times l$  systems;  $D_f = 1/\sigma_{3D}v_{3D}$  is the fractal dimension of nonspanning avalanches in the equilateral 3D model.

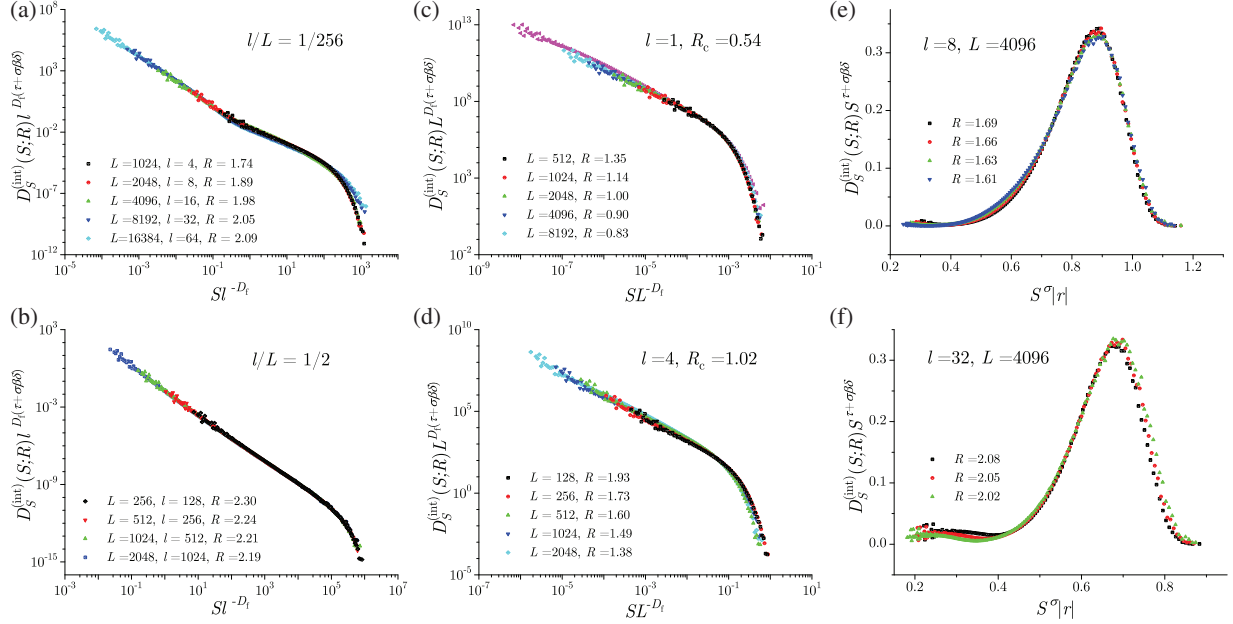


**Figure 15:** Data collapsing of the integrated size distributions  $D_S^{(\text{int})}(S; R)$  predicted by (36) in (a) and (b), by (37) in (c) and (d), and by (38) in (e) and (f). (a)  $l/L = 1/256$ . (b)  $l/L = 1/2$ . (c)  $l = 1$ ,  $R_c = 0.54$ . (d)  $l = 4$ ,  $R_c = 1.02$ . (e)  $l = 8$ ,  $L = 4096$ . (f)  $l = 32$ ,  $L = 4096$ . This is Fig. 3 from [110]

In the case of a small aspect ratio  $l/L$ , many avalanches reach the linear size  $l_a > l$  and, being squeezed between the top and the bottom system's base, effectively behave as if they are 2D avalanches spreading over a 2D lattice. On the other hand, avalanches of small linear size ( $< l$ ) are not affected by the lattice's top and bottom boundaries and behave like ordinary 3D avalanches. The presence of these two types of avalanches influences the shape of distributions like in the case of integrated size distribution shown in Fig. 15a where one can see two distinctive parts in the shape of size distributions, the left part resembling the distribution of small 3D avalanches and the right tail being comprised of quasi-2D avalanches. Such distributions have two scaling regions described by two different values of the pertinent power-law exponent, one like for 3D and the other like for 2D systems, the first one describing the region of small avalanches, and second one describing the region of quasi-2D avalanches. Between these two regions, the distribution bends at the maximum size  $S_{\text{max}}$  of the 3D-like avalanches which scales with thickness  $l$  as  $S_{\text{max}} \propto l^{D_f}$ . The distributions of other avalanche parameters (e.g., duration and energy) exhibit similar behavior as is detailed in References [110,112]. For a similar analysis performed on the strip-like systems, see Reference [131].

#### 4.4 Thin 3D Systems with Open Boundaries

Among various RFIM systems, thin systems with open boundaries play a distinguished role being the most appropriate model for real thin magnetic systems. The response of thin RFIM systems displays a lot of peculiarities studied in [111] on the  $L \times L \times l$  cubic lattices with open boundaries by the adiabatically driven ZT NEQ RFIM with Gaussian distribution of the random magnetic fields,

exchange coupling limited only to the nearest neighbors with  $J_{ij} = 1$ , absent dipolar interactions and zero demagnetizing field. The study was concentrated on the behavior of the system along the critical line comprised of the corresponding values of the effective critical disorder  $R_c^{\text{eff}}(l, L)$  and the effective critical field  $H_c^{\text{eff}}(l, L)$ , illustrated in the left panel of Fig. 16 for  $L = 256$  and  $L = 512$  vs. system thickness  $l$ . The magnetization curves obtained at  $R_c^{\text{eff}}(l, L)$  are shown in the right panel; see Section 7.2 for the multifractal analysis of the response signal of these systems.

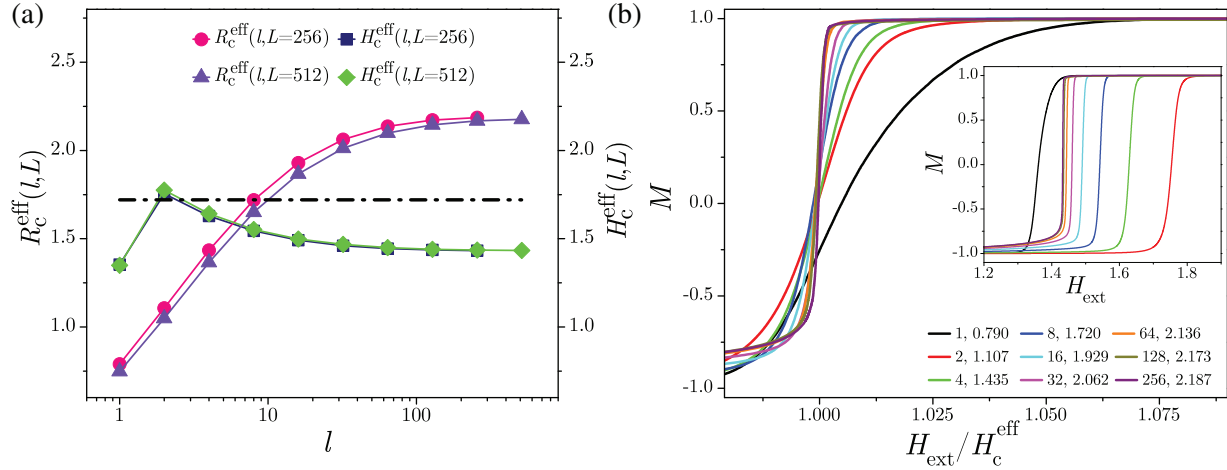


**Figure 16:** (a) Effective critical disorder  $R_c^{\text{eff}}(l, L)$  and the effective critical field  $H_c^{\text{eff}}(l, L)$  vs. sample thickness  $l$  for the base sizes  $L = 256$  and  $L = 512$ . (b) Magnetization  $M$  vs. the rescaled magnetic field  $H/H_c^{\text{eff}}$  for various  $l$  and  $L = 256$ ; for each  $l$  the magnetization curve is obtained at the corresponding effective critical disorder  $R_c^{\text{eff}}(l, L)$  shown in the legend. Inset shows the same magnetization curves vs. the magnetic field  $H$ . Figure is compiled from the first two panels of Fig. 1 from [111]

In the left column of Fig. 17, we show the size distributions  $D_S^{(w)}(S; R)$  collected in a narrow external-field window on the hysteresis loop center part (HLC), and also the corresponding integrated distributions  $D_S^{(\text{int})}(S; R)$  collected along the entire hysteresis loop. The distributions obtained for  $l$  comparable to  $L$  have the form of a power-law ending with a cutoff preceded by a bump due to the onset of large (spanning) avalanches expected at the effective critical disorder. On the other hand, the distributions for small values of  $l$  manifest two scaling regions, the left and steeper one from the small 3D-like avalanches, and the right region originating from the quasi-2D avalanches. To reliably estimate the effective values of the exponents  $\tau_1$  and  $\tau_2$ , pertaining to the left and right scaling regions, respectively, the size distributions was fitted with the aid of the model function

$$D_S^{(\text{mod})}(S) = \left\{ \left[ 1 - \tanh\left(\frac{S}{B}\right) \right] \frac{A_1}{S^{\tau_1}} + \tanh\left(\frac{S}{B}\right) \frac{A_2}{S^{\tau_2}} \right\} \exp \left[ \left(\frac{S}{D}\right)^k - \left(\frac{S}{C}\right)^\sigma \right], \quad (39)$$

that, besides on  $\tau_1$  and  $\tau_2$ , depends on additional fitting parameters, namely, the amplitudes  $A_1$  and  $A_2$ , bending size  $B$ , bump avalanche size  $D$  with the associated bump exponent  $k$ , and the cutoff avalanche size  $C$  associated with the cutoff exponent  $\sigma$ . The examples of such fits are plotted by full lines presented in the insets of the left and middle columns of Fig. 17, and also in the top row of Fig. 18. The graphs from the bottom row of Fig. 18 clearly display that  $\tau_1$  indeed corresponds to the exponent  $\tau$  in the equilateral 3D model, and likewise for  $\tau_2$  and the equilateral 2D model; for details, see supplementary information of Reference [111].

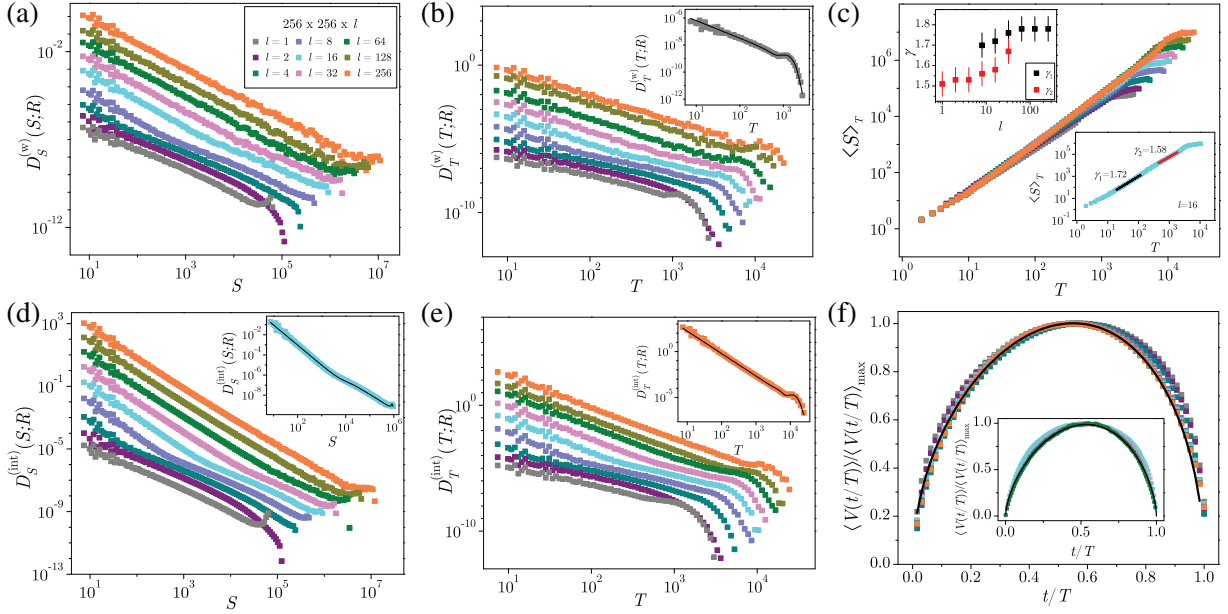


**Figure 17:** Distributions for thicknesses  $l$  from the legend that applies to the left and middle column panels. Left column: (a) windowed size distributions in the HLC part and (d) integrated size distributions with the best fit of type (39) for  $l = 16$  in the inset. Middle column: (b) HLC windowed and (e) integrated duration distributions with the insets showing the best fit of duration distribution adjusted type (39) for  $l = 1$  (b) and  $l = 256$  (e). (c) Average size  $\langle S \rangle_T$  of avalanches having duration  $T$ ; Insets in (c): determination of the exponents  $\gamma_1$  and  $\gamma_2$  for  $l = 16$  (right) and their variation with  $l$  (left). (f) Normalized average avalanche shapes  $\langle V(t/T) \rangle / \langle V(t/T) \rangle_{\max}$  vs.  $t/T$  for various  $l$  and fixed duration  $T = 64$  (main part) and  $T = 2048$  (inset). Fits with model function (40), shown by full lines, are obtained with the following values of parameters:  $a = -0.214$ ,  $\gamma_{\text{AAS}} = 1.51$  (main part);  $a = -0.176$ ,  $\gamma_{\text{AAS}} = 1.628$  (inset). This is Fig. 4 from [111]

Two scaling regions also appear in graphs showing the power-law correlation  $\langle S \rangle_T \propto T^{\gamma_{S/T}}$  between the avalanche duration  $T$  and the average size  $\langle S \rangle_T$  of avalanches of duration  $T$ , collected in a transitional range of thickness  $l$ , see Fig. 17c. The variation with thickness  $l$  of the effective values  $\gamma_1$  and  $\gamma_2$  of exponent  $\gamma_{S/T}$ , determined according to the bottom inset of the panel in the left and right scaling regions, respectively, are presented in the top inset describing two scaling regions in the thickness range  $8 \leq l \leq 32$  (for  $L = 256$ ).

The average shapes,  $\langle V(t/T) \rangle / \langle V(t/T) \rangle_{\max}$ , of avalanches with duration  $T$ , illustrated in Fig. 17f, are also considered to be described by the exponent  $\gamma_{\text{AAS}}$ . By fitting these shapes using the model function [193]

$$\langle V(t/T) \rangle / \langle V(t/T) \rangle_{\max} \propto T^{\gamma_{\text{AAS}}-1} \left[ \frac{t}{T} \left( 1 - \frac{t}{T} \right) \right]^{\gamma_{\text{AAS}}-1} \times \left[ 1 - a \left( \frac{t}{T} - \frac{1}{2} \right) \right], \quad (40)$$

depending on an additional parameter  $a$ , the so determined effective values of exponent  $\gamma_{\text{AAS}}$  are found to depend on both  $l$  and  $L$  spanning a range documented in [111] that is slightly larger than the range of effective values of  $\gamma_{S/T}$  shown in Fig. 17c.

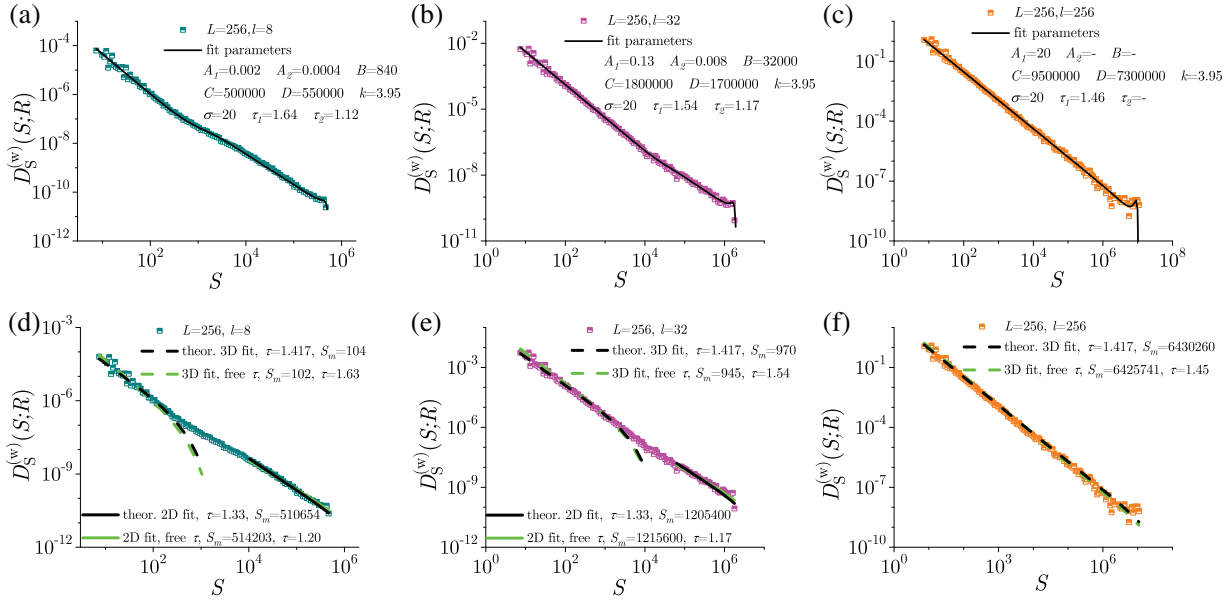


**Figure 18:** In the central part of the hysteresis loop, the distribution of avalanche size  $D_S^{(w)}(S; R)$  for different thickness  $l = 8, 32,$  and  $256$  is fitted using the expression (39), top row panels (a)–(c), and the theoretical expression predicted for interface dynamics, where 2D and 3D parts of the distribution are fitted separately in the bottom row panels (d)–(f). Note that the quoted estimates for  $\tau_1$  and  $\tau_2$  are the effective values obtained in fits of distributions' data, known to yield values different from those estimated by data collapsing, offering more reliable values generally acknowledged as the standard ones. This is Fig. 5 from [111]

## 5 Finite Driving Rate Induced Spatio/Temporal Merging of Avalanches

### 5.1 Finite Driving Rate Effects on 3D Systems

In comparison with the widely utilized adiabatic driving, presented in previous sections, driving a disordered ferromagnetic system at a constant rate provides a more realistic scenario that is very useful for analyzing experimental data. In this type of driving, the external magnetic field is incremented/decremented along rising/falling part of the magnetization curve by a constant amount  $\Delta H$  in each time-step so that the driving rate  $\Omega = \Delta H / \Delta t$  is finite and constant. Consequently, rather than developing just one at a time, avalanches (usually) propagate in multiples, sometimes overlapping in space and/or in time making impossible their separation into individual ones and the analysis of such events more complicated. Provided that  $R$  surpasses the effective critical disorder (determined for adiabatic driving), three distinct scaling regions are distinguished based on the value of the driving rate: slow (all avalanches are nonspanning), intermediate (all types of spanning avalanches appear), and fast (all spanning avalanches are full-system spanning) [130]. Power-law exponents with constant values characterize the distributions of nonspanning avalanches in the slow driving regime, being nearly identical to those in the adiabatic driving characterized by avalanches that propagate individually, well separated in time. An increase in driving rate is followed by the corresponding increase in exponent values as a result of avalanche merging and overlapping, and occurs once the rate-induced spanning avalanches emerge in the system.

As an example, three signal samples from the numerical simulations of equilateral 3D ZT NEQ RFIM driven at finite rates in each of the related regimes are displayed in Fig. 19b, together with

relevant avalanche size distributions depicted in Fig. 19a. Therefrom, it is evident that in the slow driving regime, the same behavior is observed as for the cases of adiabatic and quasistatic driving, manifested by overlapping of all avalanche distributions, regardless of the driving protocol employed. However, when driving rate increases, a departure from this tendency is observed, being the most noticeable in the fast driving regime.

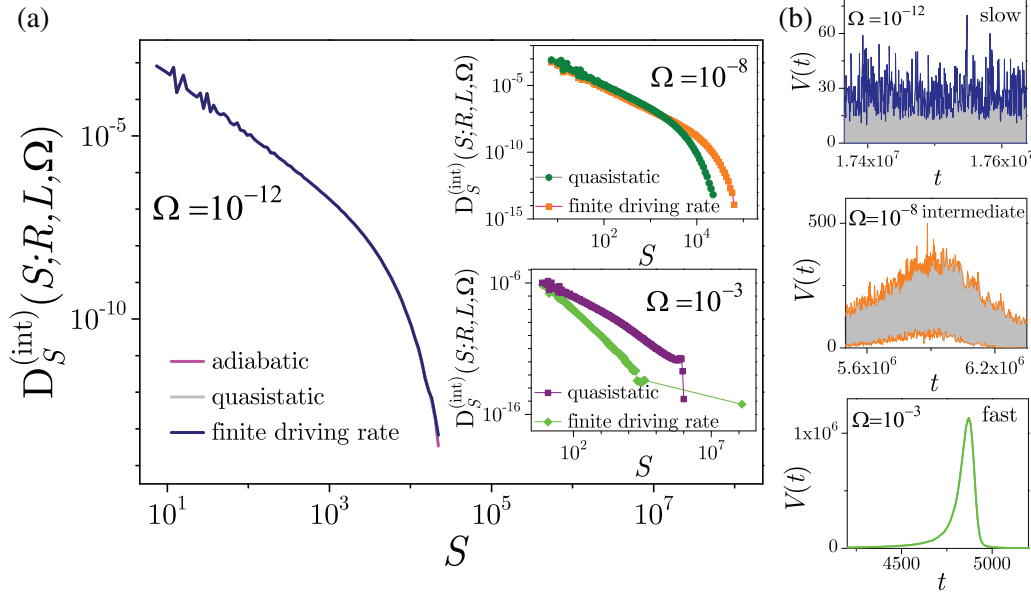


**Figure 19:** (a) Avalanche size distributions for  $L = 512$  and  $R = 2.6$ , averaged over 100 RFC for three different driving protocols: adiabatic, quasistatic and finite-rate driving. Main panel represents the cases of slow, top-inset of intermediate, and bottom-inset of fast driving. (b) Samples of signals for the cases of slow, intermediate, and fast finite rate driving regimes. This is Fig. 1 from [130]

Because the dynamics of avalanches are significantly impacted by the driving rate, it is appropriate to analyze the driving rate effects on the systems that are large enough and have sufficiently high disorder (e.g.,  $L = 512$  and  $R = 2.6$ ) ensuring that the occurrences of spanning avalanches are solely rate-attributed. Having parameters chosen in this way, the systems exhibit adiabatic-like behavior at slow enough rates which is more and more abandoned as the rate increases due to the emergence of many simultaneously propagating avalanches. Yet, the scaling of magnetization, susceptibility, and distributions of avalanche parameters of nonspanning avalanches still exists for the systems satisfying the finite-size scaling condition  $Lr^\nu = const$  amended by the rate-dependent condition  $\Omega r^{\nu/\bar{q}} = const$  with  $\bar{q} = 1$  as is shown in [130]. For magnetizations and magnetic susceptibilities obtained in simulations of such systems, the rate-dependent scaling read

$$m_{R,L}(H) = |r|^\beta \widetilde{\mathcal{M}}_\pm(h/|r|^{\beta\delta}, 1/L|r|^\nu, \Omega|r|^\nu), \quad (41)$$

$$\chi_{R,L}(H) = |r|^{\beta-\beta\delta} \widetilde{\mathcal{X}}_\pm(h/|r|^{\beta\delta}, 1/L|r|^\nu, \Omega|r|^\nu), \quad (42)$$

where  $m = M - M_c^{\text{eff}}$ . These scalings enable collapsing of the magnetization and susceptibility curves like those illustrated in Fig. 20 that are achieved with the standard values of the 3D RFIM exponents and the (adiabatic) critical value of disorder  $R_c = 2.16$  [28].

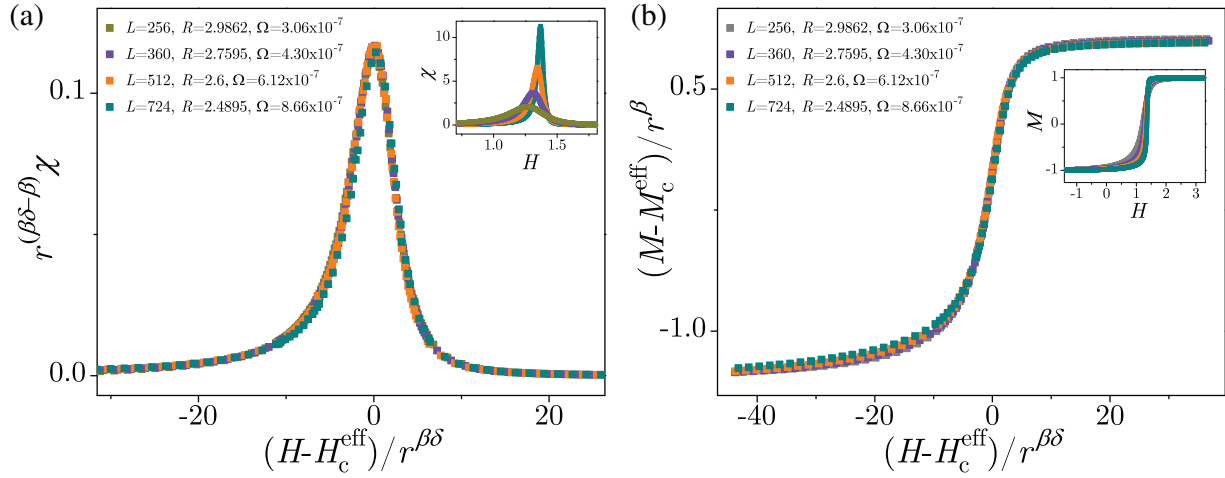


**Figure 20:** Scaling collapses of susceptibilities (a) and magnetizations (b) for system with parameters satisfying the conditions  $Lr^\nu = const$  and  $\Omega r^\nu = const$ . Insets show the non-scaled curves averaged over up to 400 different RFC realizations. Parameters of the presented set of simulations are shown in the legends. This figure is replotted from Fig. B3 from [130]

As already mentioned, the avalanching activities are more difficult to analyze at the finite driving rate because of the merging of separately nucleated avalanches into system activity events (in this section for simplicity also referred to as avalanches). Such merging enlarges avalanches changing the shape of their distributions by e.g., promoting 1d into 2d spanning avalanches causing them to ‘flow’ from the first into the second distribution (and likewise for 2d and 3d spanning avalanches). So, in the intermediate driving regime, the distributions of 1d and 2d spanning avalanches become bimodal, see two top panels in Fig. 21a, making their scaling (and consequently collapsing) impossible. Due to the same reason, prominent dents appear at the cutoff start of the nonspanning avalanches’ distributions, see the bottom-right panel of Fig. 21a, arisen from the amalgamation of multiple nonspanning avalanches that eventually approach the system boundaries, turning into the spanning and being excluded from the distribution of nonspanning avalanches. Nevertheless, given that the system parameters satisfy the compatibility conditions  $Lr^\nu = const$  and  $\Omega r^\nu = const$ , the distributions of nonspanning avalanches retain their scaling, however modified into

$$D_{S_{ns}}^{(int)}(S; R, L) = S^{-\tau'_{ns}} \mathcal{D}_{ns}(S^{\sigma_{ns}} r, 1/Lr^\nu, \Omega r^\nu), \quad (43)$$

with the rate-dependent values of the effective scaling exponents  $\tau'_{ns}$  and  $\sigma_{ns}$ , whose variation with  $\Omega$  is presented in the main panel of Fig. 21b; the collapsing following (43) is illustrated in the inset.

Inspecting the flow of the exponents  $\tau'_{ns}$  and  $\sigma_{ns}$  with the driving rate, presented in Fig. 21b, three distinct regions of driving rate can be recognized. In the regime of slow and fast driving rates, the values of both exponents are saturated at different values. However, in between these two, in the range of intermediate rates, the values of exponents are rate-dependent.

The influence of the applied driving protocol on the spatiotemporal correlations of spin-flipping activity events with quite complex rate-induced behavior is another aspect that merits consideration. Results show that, provided the system parameters are tuned to satisfy the finite-size and rate-dependent scaling conditions, the spatial activity correlations follow rate-dependent scaling in all three driving regimes [148]. Temporal activity correlations, however, turn out to be highly sensitive

to driving, so the collapsing of waiting time distributions is only achievable at very slow driving rates, and not possible for other rate choices. The increase in driving rate has a negative influence on various distributions of activity waiting times as well as on the activity average shapes that significantly deviate from slow driving and adiabatic behavior.

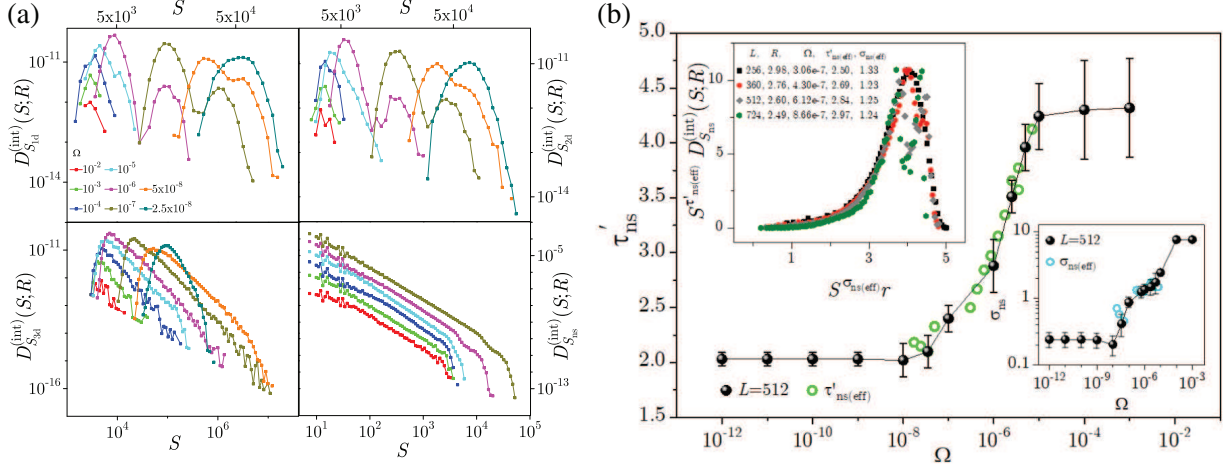


**Figure 21:** (a) The integrated size distributions of various types of avalanches (1d, 2d, 3d spanning, and nonspanning) collected at the driving rates from the legend, system size  $L = 512$ , and averaged over 100 different RFCs. (b) By open green symbols is shown the variation with  $\Omega$  of the exponents  $\tau'_{ns}$  (in the main panel) and  $\sigma_{ns}$  (in inset), pertaining to the scaling (43) under satisfied compatibility conditions  $Lr^\nu = const$  and  $\Omega r^\nu = const$ . Analogous variations, but for the scaling  $D_{S_{ns}}^{(int)}(S; R) = S^{-\tau'_{ns}} \mathcal{D}_{ns}(S^{\sigma_{ns}} r)$  which follows from (43) in the  $L \rightarrow \infty$  limit, are shown by black symbols. Left inset shows an example of the scaling collapse achieved according to (43). This figure is replotted from Figs. 5 and 9 from [130]

All spin flipping throughout the continuous system activity emerged at sufficiently high  $\Omega$  is considered as a single activity event, likely realized due to multiple nucleations of avalanches and their spatial merging. The activity event correlation function  $G_R^{ae(int)}(x; R, L, \Omega)$  refers to the probability per spin that the first spin to flip after the system's inactivity will cause the flipping of spins at a distance  $x$  from it. A characteristic plateau that develops in the intermediate and fast driving regimes is the reason for the consideration of the so-called *triggered correlation function*, defined as  $G_R^{(int)}(x; R, L, \Omega) = L^3 G_R^{ae(int)}(x; R, L, \Omega)$ ; see Fig. 22. These functions nearly overlap for slow driving rates, exhibiting adiabatic-like behavior permitting propagation of only one avalanche at a time, with the exception of the largest values of spin distance  $x$ , where the onset of a post-cutoff plateau can be observed. Insets in Fig. 22 show that as  $\Omega$  gradually increases, the heights of these plateaus rise proportionately to  $\langle T \rangle_R \Delta H$ , where  $\langle T \rangle_R$  is the average activity duration at disorder  $R$ . The plateau level finally overlaps with the main plateau at 1, signifying the beginning of genuine rate-induced spanning avalanches in the system at fast enough rates, as the driving rate increases further. The adiabatic scenario attributes this plateau exclusively to the beginning of the disorder-caused spanning avalanches emerging at higher disorders at sufficient driving rates.

When the system parameters are chosen so that the finite-size condition  $Lr^\nu = const$  and the rate-dependent condition  $\Omega r^\nu = const$  are fulfilled, the scaling

$$G_R^{ae(int)}(x; R, L, \Omega) \sim \frac{1}{x^{d+\beta/\nu}} \bar{\mathcal{G}}_{\pm}^{(\Omega)}(xr^\nu, 1/Lr^\nu, \Omega r^\nu/\bar{q}), \quad (44)$$

is expected for the activity event correlation functions  $G_R^{\text{ae(int)}}(x; R, L, \Omega)$ ; here  $\mathcal{G}_{\pm}^{(\Omega)}$  are the universal scaling functions. The pertaining collapses, shown in Fig. 23, are obtained with the rate-independent standard 3D RFIM scaling exponents in the slow, intermediate, and fast driving regime.

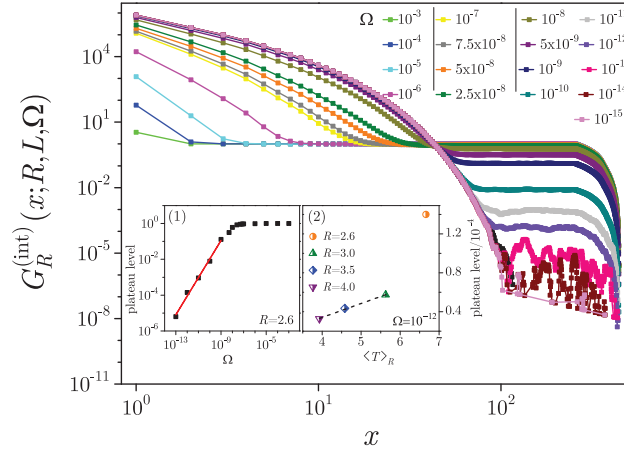


**Figure 22:** Triggered activity correlation functions  $G_R^{\text{(int)}}(x; R, \Omega, L)$  vs. inter-spin distance  $x$ . Presented  $G_R^{\text{(int)}}(x; R, \Omega, L)$  data are obtained for system size  $L = 512$ , disorder  $R = 2.6$  and a range of driving rates  $\Omega = 10^{-15} - 10^{-3}$  by averaging over 100 different RFC. The plateau level of the correlation functions increases with  $\Omega$ , reaching the saturation level ( $= 1$ ) for  $\Omega > 10^{-6}$ , as shown in inset (1). For small driving rates, the increase is linear with  $\Omega$ , indicated by the red solid line. In inset (2), it is demonstrated that the plateau level for fixed and very small  $\Omega$  and very high values of disorder  $R$  is linearly proportional also to the average duration  $\langle T \rangle_R$  of the activity event at disorder  $R$ . This figure is replotted from Fig. 1 from [148]

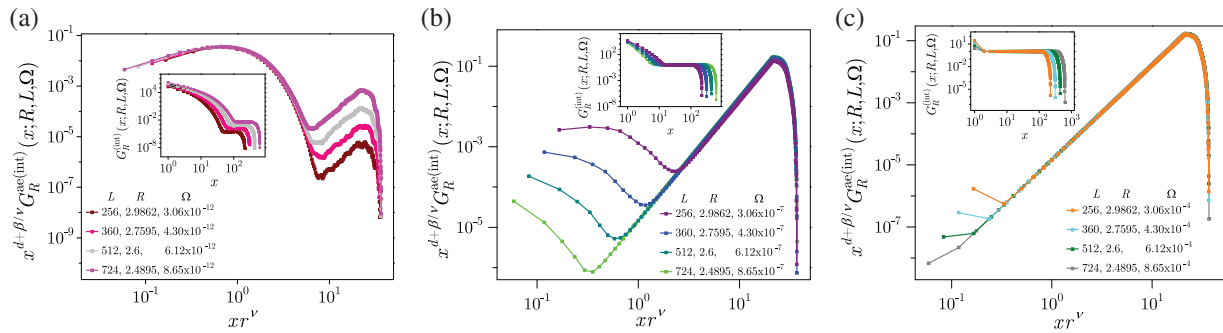


**Figure 23:** Triggered activity correlation functions  $G_R^{\text{(int)}}(x; R, \Omega, L)$ , shown in insets, and the pertaining collapses of type (44) of the activity event correlation functions  $G_R^{\text{ae(int)}}(x; R, \Omega, L)$ , shown in main panels, for systems whose parameters satisfy  $Lr^\nu = \text{const}$  and  $\Omega r^\nu = \text{const}$  scaling conditions for typical rate ranges: (a) slow, (b) intermediate, and (c) fast. The collapses are obtained with  $\nu = 1.41 \pm 0.02$ ,  $d + \beta/\nu = 3.05 \pm 0.03$ , and  $R_c = 2.16 \pm 0.03$ . The data are averaged over up to 800 RFCs. This is Fig. 3 from [148]

The time that passes between any two subsequent system activity events is known as the total waiting time,  $T_w$ . Each instance of waiting time can be classified either as internal or external waiting time,  $T_{w,\text{int}}$  and  $T_{w,\text{ext}}$ , corresponding to the period between two successive subactivities within the same

or from distinct activity events, respectively. The shape of the waiting-time distribution can be used to identify the type of temporal correlations present in the response signal. When this distribution is exponential, the temporal correlations are random; otherwise, the distribution is of a different kind.

Given that the threshold-collapsing requirements

$$V_{\text{th}}^{\sigma/(1-\gamma T/S)} r = \text{const}, \quad V_{\text{th}}^{\sigma v/(1-\gamma T/S)} / L = \text{const} \quad (45)$$

are met, together with the  $Lr^v = \text{const}$  and  $\Omega r^v = \text{const}$  scaling collapses to the form

$$V_{\text{th}}^{\sigma_{\text{int}}/(1-\gamma S/T)} D_{T_w}^{(\text{int})}(T_w; V_{\text{th}}, r, 1/L) = D_{T_w}(T_w/V_{\text{th}}^{1/(\gamma S/T-1)}; V_{\text{th}}^{\sigma/(1-\gamma T/S)} r, V_{\text{th}}^{\sigma v/(1-\gamma T/S)} / L), \quad (46)$$

introduced in [140] can be achieved in the slow driving regime for all types of the waiting-time distributions (see Fig. 24) with remark, however, that the increase of the driving rate causes distortions in the waiting time distributions  $D_{T_w}^{(\text{int})}$ , making these collapses unfeasible [148].

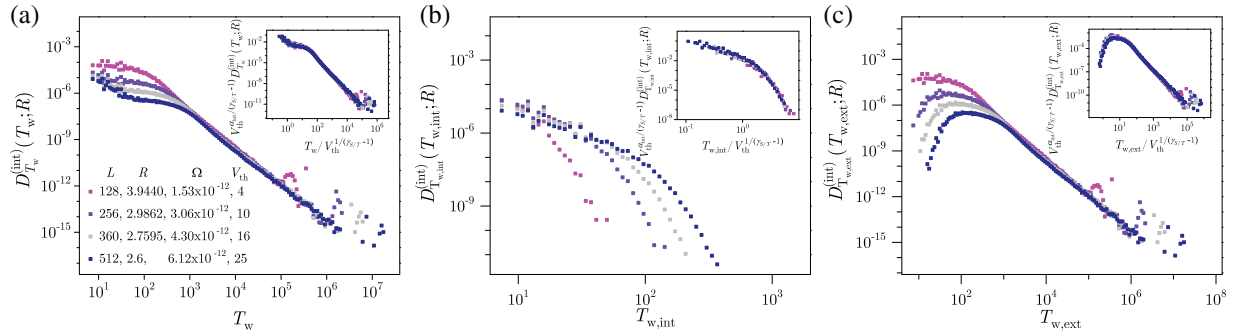


**Figure 24:** Distributions of (a) total, (b) internal, and (c) external waiting times, shown in the main panels, and their collapses (shown in insets) obtained in the slow driving regime with parameters satisfying the requirements (45) together with the  $Lr^v = \text{const}$  and  $\Omega r^v = \text{const}$ ; legend presented in (a) applies to all panels. Scaling collapses are achieved with  $R_c = 2.16 \pm 0.02$ ,  $\alpha = 2.75 \pm 0.10$  and with values of exponent  $\sigma v z = 2.00 \pm 0.05$  for the collapses of total  $D_{T_w}^{(\text{int})}(T_w; R)$  and external  $D_{T_{w,\text{ext}}}^{(\text{int})}(T_{w,\text{ext}}; R)$  waiting times, shown in panels (a) and (b), and  $\sigma v z = 1.8 \pm 0.02$  for the collapse of internal waiting times  $D_{T_{w,\text{int}}}^{(\text{int})}(T_{w,\text{int}}; R)$ , shown in panel (c). This figure is replotted from Fig. 8 from [148]

The correlation  $\langle S \rangle_T \sim T^{\gamma S/T}$ , between the duration  $T$  and the average size  $\langle S \rangle_T$  of activity events with duration  $T$ , is shown in Fig. 25a. The inset illustrates the change in the (specifying this correlation) exponent  $\gamma_{S/T}$  with the driving rate  $\Omega$ , declining in the range of slow driving rates, followed by the quick decrease in the intermediate, until reaching a plateau for the fast driving rates. Fig. 25b illustrates how the average shape of activity events changes with the driving rate, transitioning from adiabatic-like symmetric forms at slow driving rates to flat shapes at high driving rates, as a consequence of the spatio-temporal merging of simultaneously propagating avalanches. The driving rate's impact on the power spectrum is displayed in Fig. 25c. In the slow driving regime, the power-law shape is maintained over a wide range of frequencies. Power spectra of the finite-rate driven systems display a higher degree of rate sensitivity; as the driving rate increases, the low-frequency spectra begin to diverge from this form, which eventually causes the scaling area to subside before the maximum rates are even achieved.

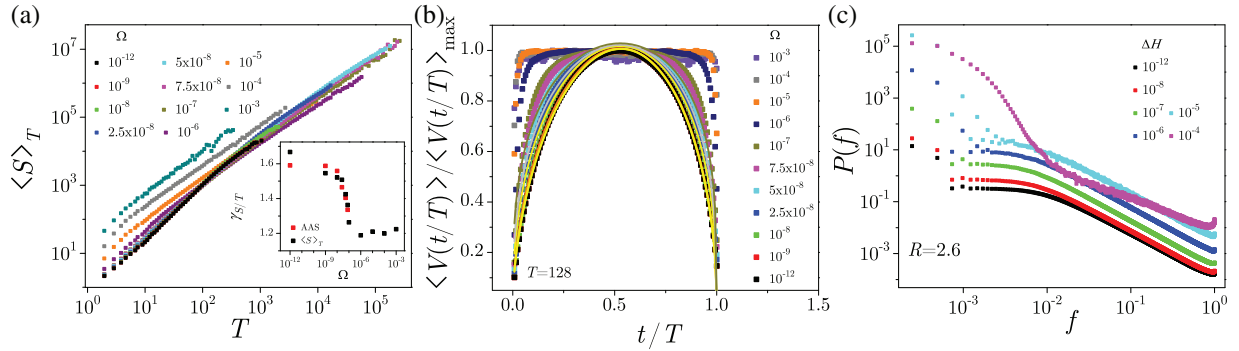


**Figure 25:** (a) Average size  $\langle S \rangle_T$  of activity events of duration  $T$  presented against  $T$  in the full range of driving rates given in legend. Inset shows the change of the exponent  $\gamma_{S/T}$  with the driving rate  $\Omega$ . (b) Normalized average shape of activity events,  $\langle V(t/T) \rangle / \langle V(t/T) \rangle_{\max}$ , in the full range of driving rates from legend and fixed duration  $T = 128$ . Data is for  $L = 512$ ,  $R = 2.6$ , and averaged over 100 RFCs. (c) Power spectra  $P(f)$  in a driving rates range from legend. Replotted from Fig. 9 [148], and Fig. 11 [147]

In the finite-rate driving protocol, spanning activity events occur not just in the subcritical disorder domain, but also for higher disorders given the system is driven fast enough. This suggests that in systems of size  $L$ , there exists an effective critical driving speed  $\Omega_c^{\text{eff}}(R, L)$  for every value of disorder  $R > R_c^{\text{eff}}(L)$  such that the spanning activity events are absent or present below or above it. These values are depicted by symbols in the left panel of Fig. 26, whereas by full lines are shown the values of critical driving rate  $\Omega_c^{\text{eff}}(R)$ , estimated as  $\Omega_c(R) = \lim_{L \rightarrow \infty} \Omega_c^{\text{eff}}(R, L)$  for the cases of quasistatic and finite-rate driving. Each of these two lines is the boundary between the region of *slow*, i.e.,  $\Omega < \Omega_c(R)$ , and *fast*, i.e.,  $\Omega > \Omega_c(R)$ , driving for the corresponding driving regime of infinite systems, whereas for finite systems *intermediate*, i.e.,  $\Omega_c(R) < \Omega < \Omega_c^{\text{eff}}(R, L)$ , rates separate slow from fast driving  $\Omega > \Omega_c^{\text{eff}}(R, L)$ . The values of  $\Omega_c(R)$  increase with  $R$ , and the flow for quasistatic driving qualitatively resembles the one for finite-rate driving, but the values belong to the range of higher rates.

Besides the critical driving speed, the flow of the effective critical magnetic field  $H_c^{\text{eff}}(R, L)$ , estimated from the corresponding maxima of the susceptibility curves with disorder  $R$ , is shown in Fig. 26b. Presented data are obtained for all three types of driving (adiabatic, quasistatic and finite-rate driving), as is shown in the pertinent legend. Provided the spanning activity events are present, the jump (more precisely-sharp increase) in magnetization occurs at this value of the external magnetic field. One can see the overlapping of the values obtained for adiabatic and for slow quasistatic and finite-rate driving, which is in accordance with the rest of the findings. With the increase in driving rate, the flow is systematically shifted vertically to higher magnetic field values.

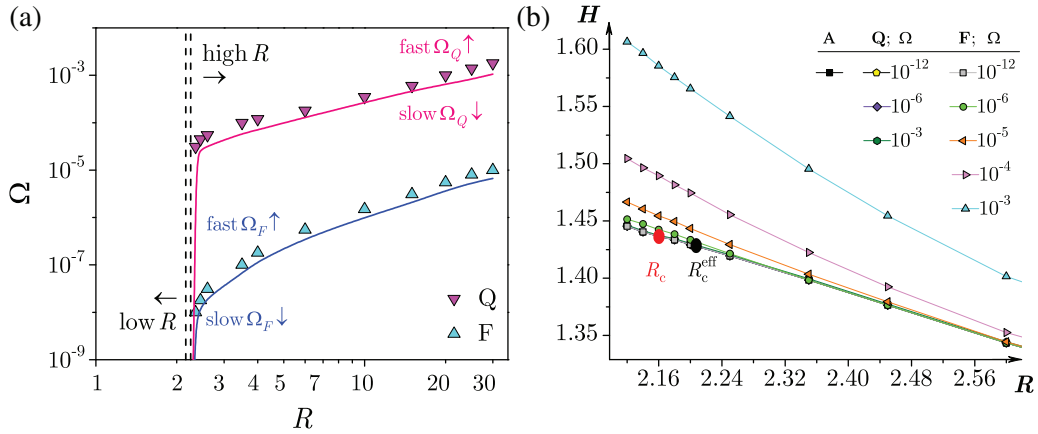


**Figure 26:** (a) Phase diagram showing the effective critical driving rate  $\Omega_c^{\text{eff}}$  against disorder  $R$  in quasistatic (Q) and finite-rate (F) driving protocol. Two vertical dashed lines bound the (narrow) region of transitional disorders for  $L = 512$ . (b) Effective critical magnetic field  $H_c^{\text{eff}}(R, L)$  vs. disorder  $R$  in adiabatic (A), quasistatic (Q), and finite-rate (F) driving protocol, the later two for the values of driving rate  $\Omega$  shown in legend. Symbols show the  $\Omega_c^{\text{eff}}(R, L)$  and  $H_c^{\text{eff}}(R, L)$  data for the system size  $L = 512$ , averaged over up to 50 different RFCs. The full lines in (a) depict the estimated values of the critical driving speed  $\Omega_c(R) = \lim_{L \rightarrow \infty} \Omega_c^{\text{eff}}(R, L)$ , while in (b) they connect the symbols for better visibility. This figure is replotted from Fig. 17 in [147]

## 5.2 Finite Driving Rate Effects on 2D Systems

The disorder of the system, which suppresses avalanche propagation, and the driving rate, which promotes it, pair up to produce the relaxation dynamics in the finite-rate driving protocol. Study of the effects of finite driving by the time-varying external magnetic field in the 2D disordered ferromagnetic systems is important from a conceptual and practical standpoint, due to the growing interest in novel miniature (quasi) 2D systems operating in the finite-rate driving regimes [149].

Following modified power-laws satisfying the scaling and data collapsing predictions introduced to describe the rate-dependent behavior of the model, it is demonstrated that it exhibits a dynamical phase transition with three distinctive regimes of driving rate identified in 2D, as in the case of 3D systems. Within the first regime of slow driving, the behavior of the system is approximately adiabatic from which it gradually deviates upon the increase of driving rate. At intermediate rates, owing to the temporal overlapping and/or spatial merging of avalanches, multiple spanning activity events are observed, whereas at fast driving rates, the system behavior is mainly influenced by the propagation of the biggest activity event as the single one spanning the system.

The new rate-dependent scaling forms are derived and implemented and their validity confirmed in extensive numerical simulations [149]. The system response follows a rate-dependent scaling in all three regimes of driving rate provided that the system parameters are tuned in compliance with the finite-size scaling condition  $Lr^\nu = \text{const}$  (relating system size  $L$  with reduced disorder  $r = (R - R_c)/R$ ), together with the rate-dependent scaling condition  $\Omega r^{\nu/\bar{q}} = \text{const}$  specified by the newly introduced rate exponent  $\bar{q}$  with optimal value found to be  $\bar{q} = -0.4 \pm 0.05$  [149].

Within the constraints of the 2D system geometry, only two types of spanning avalanches can be realized, namely the 1d and 2d spanning avalanches [27,106], depending on whether the spanning

spreads along only one, or both spatial dimensions; the remaining avalanches are classified as nonspanning. The numbers per single run of these two types of spanning avalanches,  $N_{1d}/N_{\text{runs}}$  and  $N_{2d}/N_{\text{runs}}$ , together with their total number  $N_{\text{tot}}/N_{\text{runs}}$  are shown in Fig. 27. What can be seen is that in the slow driving regime there are no spanning avalanches, as expected, while in the fast regime in each run appears one 2d full system spanning avalanche and none of the 1d spanning avalanches. In the intermediate regime of rates, both types of spanning avalanches are present and their rate-dependent numbers are reaching even up to 3 for the 2d spanning avalanches. This is a clear difference from the adiabatically driven systems where this number never surpassed 1.

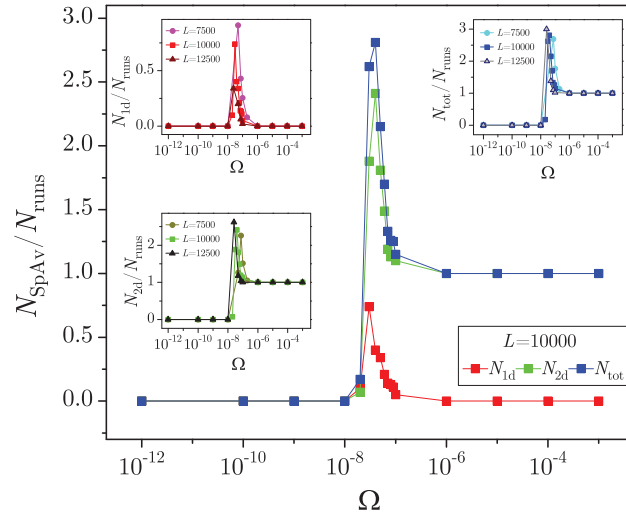


**Figure 27:** In the main panel are shown the number of spanning avalanches (1d, 2d and total) per single run  $N_{\text{SpAv}}/N_{\text{runs}}$  as a function of driving rate  $\Omega$ . System size is  $L = 10,000$ , disorder  $R = 0.8$  and the data are averaged over  $N_{\text{runs}} = 100$  RFCs. In the insets are separately shown: the number  $N_{1d}/N_{\text{runs}}$  of 1d (top left), the number  $N_{2d}/N_{\text{runs}}$  of 2d (bottom left) and the total number  $N_{\text{tot}}/N_{\text{runs}}$  (top right) of spanning avalanches per single run for the systems with parameters  $(L, R) = (12,500, 0.784)$ ,  $(L, R) = (10,000, 0.8)$ , and  $(L, R) = (7500, 0.8228)$ . The data are averaged over up to 500 RFCs. This is Fig. 1 from [149]

As was previously demonstrated in the 3D example, the presence of either disorder-induced or rate-induced spanning events in the system determines the shape of magnetization curves. Like in the case of 3D systems driven at a finite driving rate, adiabatic-like behavior is maintained at low driving rates, but at higher rates, a rate-induced deviation from the usual adiabatic curves is apparent. Modified scaling forms taking into account the rate-dependence of the general form of the invariant  $\Omega r^{\nu/\bar{q}}$  [130] are tested as well

$$m = r^{\beta} \mathcal{M}(h'/r^{\beta\delta}, 1/Lr^{\nu}, \Omega r^{\nu/\bar{q}}), \quad (47)$$

$$\chi = r^{\beta-\beta\delta} \chi(h'/r^{\beta\delta}, 1/Lr^{\nu}, \Omega r^{\nu/\bar{q}}) \quad (48)$$

and it has been numerically demonstrated that  $\bar{q} = -0.4$  is the optimal choice [149], allowing the collapses obtained using the rate-independent standard adiabatic 2D NEQ ZT RFIM values of the involved exponents  $(\beta, \beta\delta, \nu)$  [89], shown in insets of Fig. 28.

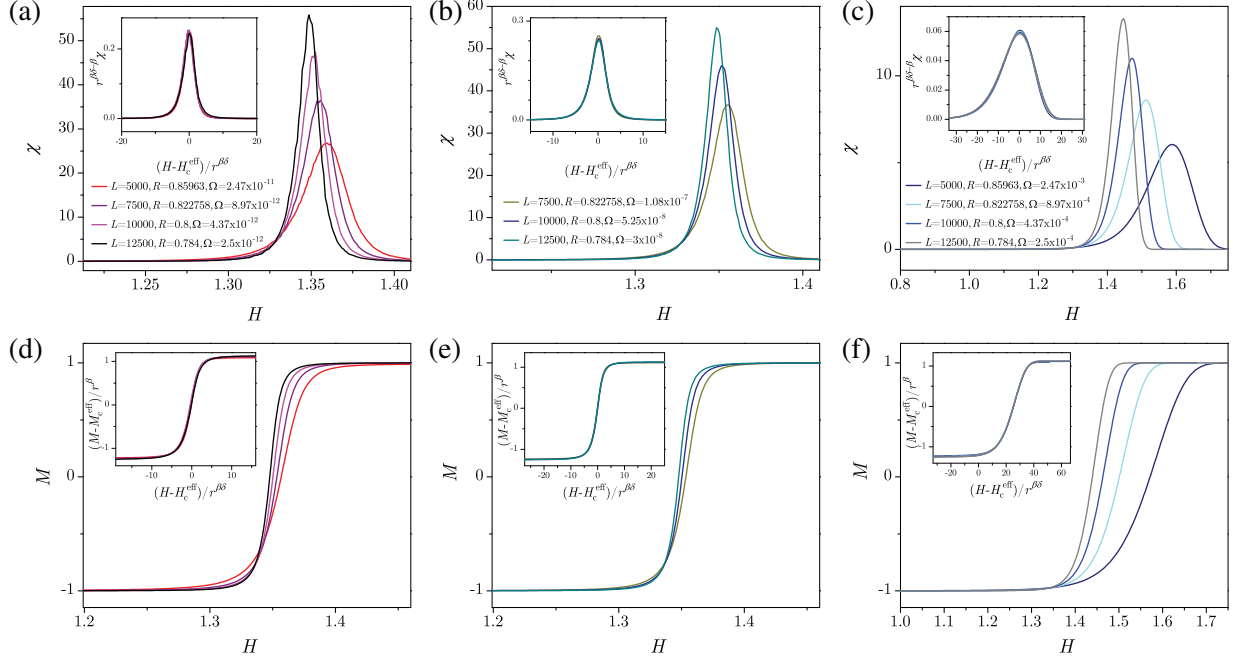


**Figure 28:** Susceptibilities are shown in the main panels of (a), (b), and (c) from the top row, while magnetizations are shown in the main panels of (d), (e), and (f) from the bottom row. All presented curves are acquired for the  $L, R$  pairs with both  $Lr^\nu = const$ , and  $\Omega r^{\nu/\bar{q}} = const$  ( $\bar{q} = -0.4$ ) scaling conditions satisfied. The curves in panels (a) and (d) are obtained in the slow driving rate regime for the  $L, R$  pairs quoted in legend from panel (a), the curves in panels (b) and (e) are obtained in the intermediate driving rate regime for the  $L, R$  pairs quoted in legend from panel (b), and the curves in panels (c) and (f) are obtained in the fast driving rate regime for the  $L, R$  pairs quoted in legend from panel (c). The pertaining finite-size scaling collapses, in all driving regimes, are accomplished using  $R_c = 0.54 \pm 0.02$ ,  $\beta = 0.15 \pm 0.04$  and  $\beta\delta = 4.8 \pm 0.2$ ; replotted from Fig. 5 from [149]

Taking into account the effect of driving rate, similarly as it was done for the 3D case [130], the three types of scaling predictions for the integrated size distributions of nonspanning activity events (avalanches) are predicted in [149] given that the conditions  $Lr^\nu = const$  and  $\Omega r^{\nu/\bar{q}} = const$  are satisfied

$$D_S^{(int)}(S; R, L, \Omega) = S^{-\tau'} \tilde{\mathcal{D}}_S(S^\sigma r; 1/Lr^\nu, \Omega r^{\nu/\bar{q}}), \quad (49)$$

$$D_S^{(int)}(S; R, L, \Omega) = L^{-\tau'/\sigma\nu} \tilde{\mathcal{D}}_L(S^\sigma r; 1/Lr^\nu, \Omega r^{\nu/\bar{q}}), \quad (50)$$

and

$$D_S^{(int)}(S; R, L, \Omega) = \Omega^{-\bar{q}\tau'/\sigma\nu} \tilde{\mathcal{D}}_\Omega(S^\sigma r; 1/Lr^\nu, \Omega r^{\nu/\bar{q}}), \quad (51)$$

where  $\tilde{\mathcal{D}}_S$ ,  $\tilde{\mathcal{D}}_L$ , and  $\tilde{\mathcal{D}}_\Omega$  are the corresponding universal scaling functions. These collapses, along with the pertinent distributions, are presented in Fig. 29.

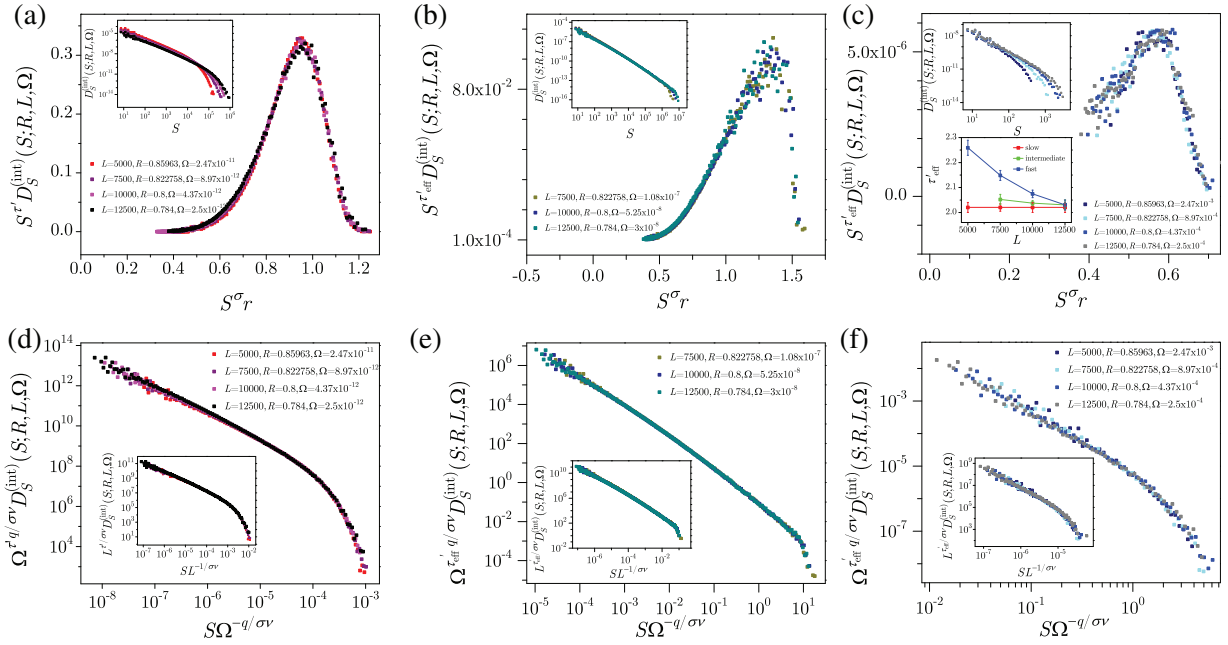


**Figure 29:** For the integrated size distributions of nonspanning activity events, shown in the top insets of panels (a), (b), and (c), we present their scaling collapses: of type (49) in top-row panels, of type (51) in bottom-row panels (d), (e), and (f), and of type (50) in insets of the bottom-row panels (d), (e), and (f). The systems parameters satisfy both  $Lr^\nu = \text{const}$  and  $\Omega r^{1/\bar{q}} = \text{const}$  scaling conditions in each of three driving regimes: slow (panels (a) and (d) in the left column), intermediate (panels (b) and (e) in the middle column), and fast (panels (c) and (f) in the right column). All collapses are achieved with adiabatic values  $R_c = 0.54 \pm 0.02$ ,  $\nu = 5.15 \pm 0.20$ , and  $\sigma = 0.10 \pm 0.01$ , together with  $\tau' = 2.02 \pm 0.06$  in the slow regime, while in the intermediate and fast driving regime the effective exponent  $\tau'_{\text{eff}}(L)$  is used whose values flow with the system size  $L$  as is depicted in the bottom inset of panel (c) along with the pertaining error bars. The obtained data are averaged over up to 6400 RFCs. In this figure are combined Figs. 8 and 9 from [149]

Fig. 30 evidences that all changes with  $\Omega$ , observed for the average size of activity events with given duration, average avalanche shapes, and power spectra in the 3D case, hold in the 2D case as well-cf. Fig. 25 for the analogous graphs in the 3D case. In particular, the main part of panel (a) shows that in a wide range of driving rates  $\Omega$  the correlations  $\langle S \rangle_T \sim T^{\gamma_{S/T}}$  seem to remain stable due to overlapping of graphs, while the inset illustrates barely noticeable differences between these graphs by the variation of the exponent  $\gamma_{S/T}$  with the driving rate  $\Omega$  obtained by three different methods described in the caption. Panel (b) shows how the normalized average avalanche shapes  $\langle V(t|T) \rangle / \langle V(t|T) \rangle_{\text{max}}$  for the fixed duration  $T$ , like in the 3D case shown in Fig. 25b, get more and more flat when  $\Omega$  grows as a consequence of increased spatio-temporal merging of individually nucleated avalanches caused by high driving rate, while the panel (c) gives an overview of the corresponding  $\Omega$ -variation of the graphs showing power spectra  $P(f)$  vs. frequency  $f$ .

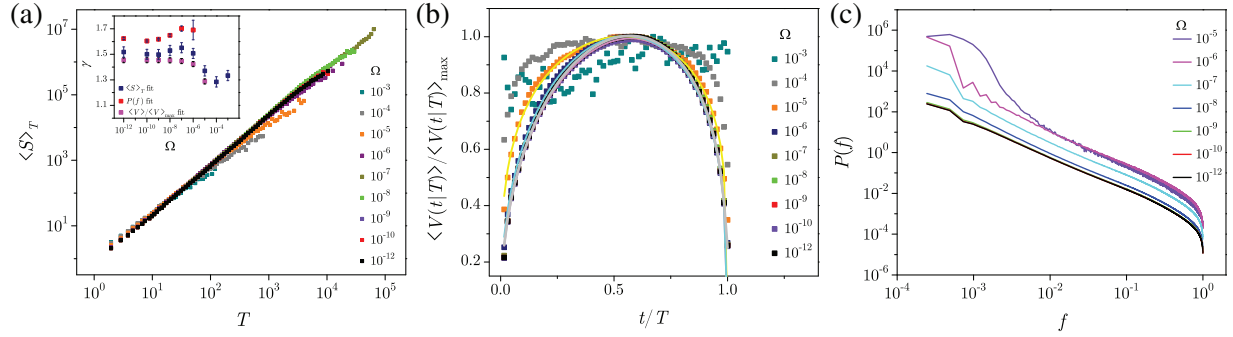


**Figure 30:** (a) Correlations between the average size  $\langle S \rangle_T$  of activity events of duration  $T$  presented against  $T$  in the full range of driving rates shown in the legend. Displayed data is obtained for the systems with  $L = 10,000$  and  $R = 0.8$ , and averaged over 100 different realizations of RFCs. (b) Normalized average avalanche shape  $\langle V(t|T) \rangle / \langle V(t|T) \rangle_{\max}$  for the fixed duration  $T = 64$  in a wide range of driving rates shown in the legend. (c) Power spectra  $P(f)$  vs. frequency  $f$  for the same driving rates. Inset in (a) shows the change with the driving rate  $\Omega$  of values of the exponent  $\gamma$  estimated in three ways as the fitting parameter:  $\gamma = \gamma_{S/T}$  for the  $\langle S \rangle_T \sim T^{\gamma_{S/T}}$  correlation data,  $\gamma = \gamma_{\text{spc}}$  for the power-law  $P(f) \sim f^{-\gamma_{\text{spc}}}$ , and  $\gamma = \gamma_{\text{AAS}}$  for the average avalanche shapes  $\langle V(t|T) \rangle / \langle V(t|T) \rangle_{\max} \sim T^{\gamma_{\text{AAS}}-1} \left[ \frac{t}{T} \left( 1 - \frac{t}{T} \right) \right]^{\gamma_{\text{AAS}}-1}$ . Error bars of the  $\gamma_{\text{spc}}$  values are 3 times magnified for better visibility. In this figure are combined Figs. 10, 11 and 12 from [149]

The preceding similarity trend continues for the integrated correlation functions which in the slow driving regime display adiabatic-like behavior illustrated in Fig. 8 for the 2D case, up to the cutoff end, after which the onset of a post-adiabatic plateau can be noticed, occurring for big inter-spin distances  $x$  due to the rate induced spatio/temporal overlapping of avalanches nucleating simultaneously without producing a spanning avalanche. With the increase of rate, the plateaus elongate and their level increases, eventually saturating and overlapping with the main plateau. This main plateau, ending with a region in which the correlation function rapidly drops to zero, occurs for fast rates and is being the characteristics of the onset of rate-induced spanning avalanches in the system resulting from merging of concurrently propagating avalanches, otherwise absent in the adiabatic and slow driving regime for disorders surpassing the effective critical disorder  $R_c^{\text{eff}}(L)$  for the employed lattice, see [149]. Taking into account the rate dependence, collapses of the correlation functions can be achieved following the scaling prediction

$$G_R^{(\text{int})}(x; R, L, \Omega) \sim \frac{1}{x^{d+\beta/\nu}} \bar{\mathcal{G}}_{\pm}(xr^{\nu}, 1/Lr^{\nu}, \Omega r^{\nu/\bar{q}}), \quad (52)$$

as presented in Fig. 31, provided that both of the conditions  $Lr^{\nu} = \text{const}$  and  $\Omega r^{\nu/\bar{q}} = \text{const}$  are met.

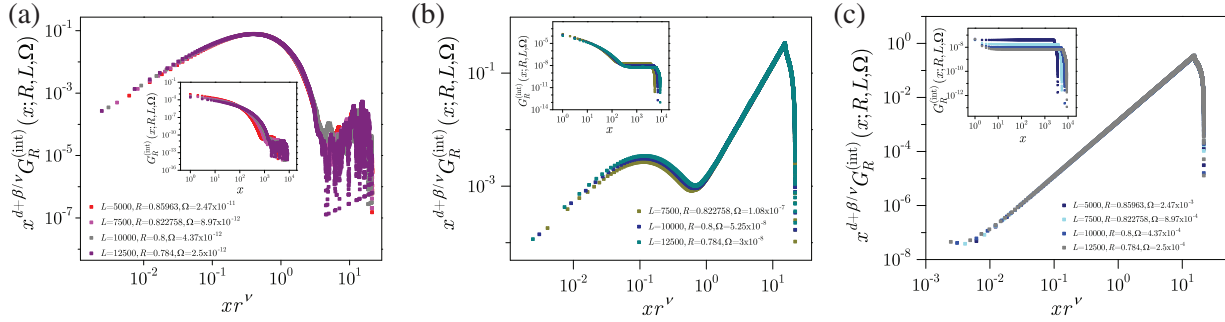


**Figure 31:** Main panels of (a), (b), and (c) show the scaling collapses of the integrated correlation functions  $G_R^{(\text{int})}(x; R, L, \Omega)$ ; integrated triggered correlation functions are depicted in insets. Scaling collapses of type (52) are all obtained with  $\nu = 5.15 \pm 0.02$ ,  $d + \beta/\nu = 2.04 \pm 0.03$  and  $R_c = 0.54 \pm 0.02$ . Number of runs per which the data are averaged goes up to 800. This is Fig. 15 from [149]

### 5.3 Crossover from 3D to 2D RFIM Systems Driven at a Finite Driving Rate

The imposed driving type together with the system thickness in the nonequilateral geometry profoundly affects its evolution, demonstrated in the magnetizations, coercive fields, distributions of avalanche sizes, correlation functions, average avalanche shapes and distributions of average avalanche size of a given duration [171]. While the driving rate remains in the slow regime, regardless of its thickness, a system behaves as being rate-independent and driven adiabatically. With the increase of the driving rate, the rate-sensitive behavior emerges, as a consequence of the initiation of multiple simultaneously propagating avalanches gathering and assembling into a complex response of system activity. This becomes even more intricate when the system's thickness is in the transitional range, due to the coexistence of different types of avalanches, displaying both 3D and 2D effects described with pertinent effective rate-dependent exponents changing with the driving rate. Understanding this dimensional crossover is of considerable importance for the analysis of data obtained in experimental studies conducted on field-driven nonequilateral samples such as ferromagnetic strips, ribbons and thin films [194,195].

The dimensional crossover from 3D to 2D systems at finite driving rates is numerically studied in [171] so that for each system's thickness the disorder is fixed above the critical line for adiabatic driving to ensure that the emergent critical behavior is solely attributed to the increased driving rates of the external field. The so-called transient thicknesses are characterized by the double-sloped distributions of avalanche parameters (such as sizes), which show the coexistence of two types of avalanches: purely 3D but small-sized avalanches and effectively 2D 'squeezed' avalanches, whose propagation is constrained by the system limits. Fig. 32 shows the integrated avalanche size distributions  $D_S^{(\text{int})}(S; R)$  across all driving regimes. The power-law is kept as long as the driving is slow enough, with the cutoff size increasing as the driving rate increases due to the merging and spatio/temporal overlapping of simultaneously propagating avalanches. This impact is particularly noticeable in the fast regime causing a massive system-spanning avalanche for each system thickness  $l$  [27,106,107]. The distributions in the insets of Fig. 32 are double-sloped, and they correspond to a transitional thickness of  $l = 16$ , at which point small 3D avalanches coexist with base-spreading ones that propagate as 2D avalanches. Both the exponents characterizing the scaling of large 2D-like avalanches and small 3D avalanches grow with the driving rate, with the latter being more sensitive to the applied rate.

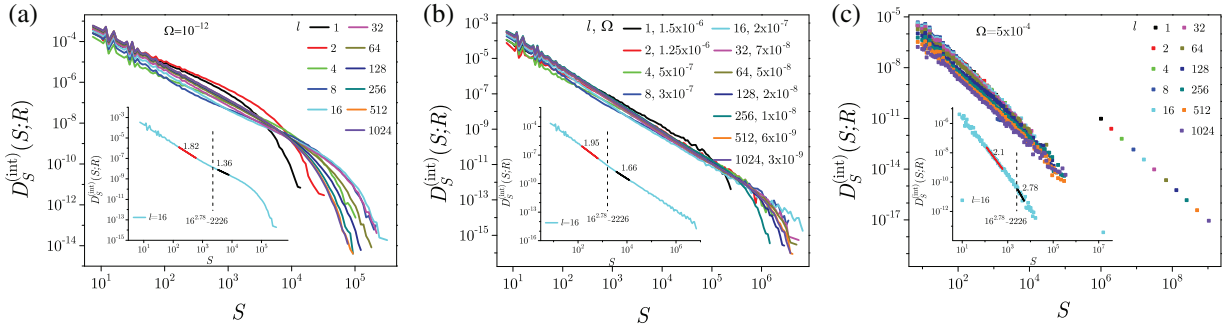


**Figure 32:** Integrated distributions  $D_S^{(\text{int})}(S; R)$  of avalanche size  $S$  in the slow (a), intermediate (b), and fast (c) regimes in the full range of system thicknesses  $l = 1 - 1024$  for  $L = 1024$ . Data are averaged over 100 RFCs. Insets show distributions for thickness  $l = 16$  with characteristic double slope, marking two different contributions: the initial one coming from 3D-like avalanches of small size  $S$ , followed by the part coming from large 2D-like avalanches. This is Fig. 5 from [171]

With some modifications in the transition from 3D to 2D with the systematic change of system thickness  $l$ , integrated triggered activity event correlation functions [148,149], which measure the correlations between pairs of spins belonging to the same activity event and being separated by a distance  $x$ , exhibit similar rate dependency as was shown for the equilateral 3D systems [148]. The integrated correlation functions in the slow, intermediate, and fast regimes for representative thicknesses, namely, very thin that produce 2D-like avalanches, transient that permit the coexistence of 2D and 3D avalanches, and fully equilateral 3D systems that have no restrictions on the shape of the avalanche, are displayed in Fig. 33.

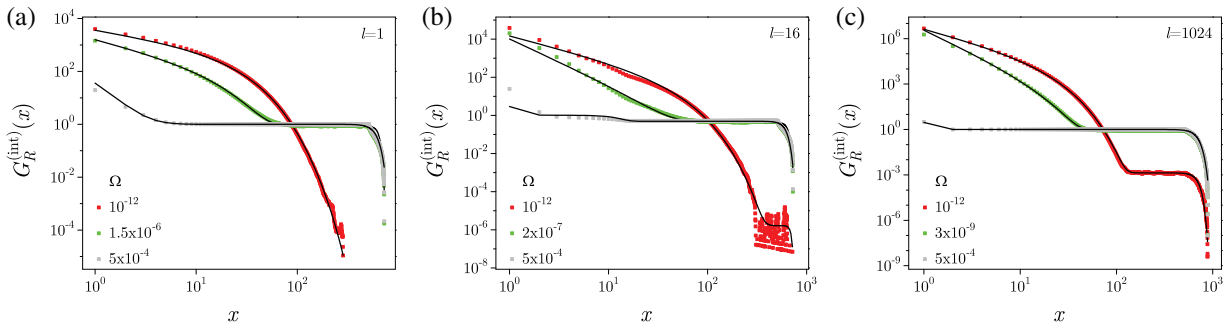


**Figure 33:** Integrated correlation functions in the slow, intermediate, and fast regimes for the representative thicknesses:  $l = 2$  in (a),  $l = 16$  in (b), and  $l = 1024$  in (c). This is the bottom row of Fig. 7 from [171]

Fig. 34 shows average avalanche shapes on the time scale measured from the commencement of an avalanche divided by the duration of the avalanche  $T$ . These shapes are fairly symmetric for all system thicknesses for slow and moderate driving regimes, but flattening of their forms occurs for high rates, as seen in panel (c), because of the superposition of simultaneously propagating avalanches (also shown for the equilateral field-driven systems in [148]). With  $\gamma_{\text{eff}}$  being the effective rate-dependent value of the exponent  $\gamma_{S/T}$ , the average size of avalanches with a given duration  $T$  scales as  $\langle S \rangle_T \sim T^{\gamma_{\text{eff}}}$ . As the system thickness increases, the  $\gamma_{\text{eff}}$  values transition from  $\gamma_{2D} \sim 1.55$ , peaking at  $l = 16$ , where the distribution also breaks because of the combined effect of 2D and 3D avalanches. From there, as

$l$  increases within the system transit to the equilateral 3D geometry,  $\gamma_{\text{eff}}$  increases further, reaching the value of  $\gamma_{3\text{D}} \sim 1.7$ . This change is less noticeable in the intermediate regime, although the exponent still somewhat maintains the same flow. Due to the existence of a massive system-consuming avalanche,  $\gamma_{\text{eff}}$  values saturate to a lower range at about  $\gamma_{\text{eff}} \sim 1.2$  in the fast driving regime.

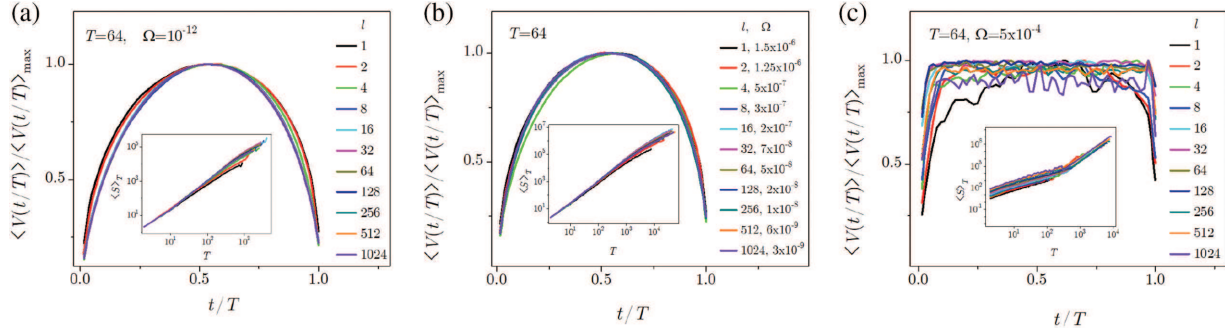


**Figure 34:** Average avalanche shapes for avalanches with duration  $T = 64$  and systems with various thicknesses in three characteristic driving regimes, slow (a), intermediate (b), and fast (c). Insets show the average size  $\langle S \rangle_T$  of avalanches having duration  $T$  for various system thicknesses in the pertaining driving regimes. This figure is replotted from Figs. 8 and 9 from [171]

#### 5.4 Finite Driving Rate Effects on the Behavior of Thin 3D Systems

From a theoretical, experimental, and practical standpoint, thin disordered ferromagnetic systems pose a challenge in terms of comprehending their spatio/temporal evolution. Numerical simulations using the geometry of thin nonequilateral systems, where one dimension is much smaller than the other two, are used to address this problem over a wide range of driving rates and disorders [172].

The results suggest that the behavior that arises is the product of a non-trivial interaction between the three elements: the sample's geometry, the disorder, and the employed driving protocol. Therefore, all commonly analyzed quantities exhibit rate-sensitive behavior, which appears in the generated signal's shape and consequently all related behavior characteristics. In particular, this leads to changes in the distributions of avalanche parameters, correlation functions, and average avalanche shapes, which are characterized by the rate-dependent values of relevant exponents and coercive field values. Regardless of the system's disorder, an almost adiabatic response happens during the slow driving, the deviation from which increases with the driving rate because many generated avalanches advance simultaneously (and possibly merge in space) forming activity events in the system response by their intricate superposition. This process is also influenced by the system's geometry, which restricts the propagation in the direction of the system's thickness, forcing avalanches to expand over the base plane and making them essentially two-dimensional.

The size distributions obtained for systems with a representative combination of thickness and disorder are exemplified in Fig. 35. System's behavior for disorders below the effective critical is dominated by spanning avalanches, independent of its thickness. The occurrence of rate-induced spanning avalanches is evident with increasing rate, manifested in the modification of the distribution shape and the extension of the cutoff area to larger avalanche sizes. The windowed avalanche size distributions (comprised of avalanches that occur in the narrow magnetic field window selected so to facilitate comparison with the experimental data) are displayed in the middle panel of Fig. 35. Right panel of Fig. 35 shows the variation of  $\tau_{\text{eff}}$  with the driving rate  $\Omega$ , falling as driving rate increases, up to the fastest driving rate ( $\Omega = 10^{-6}$ ), at which the exponent value abruptly increases.

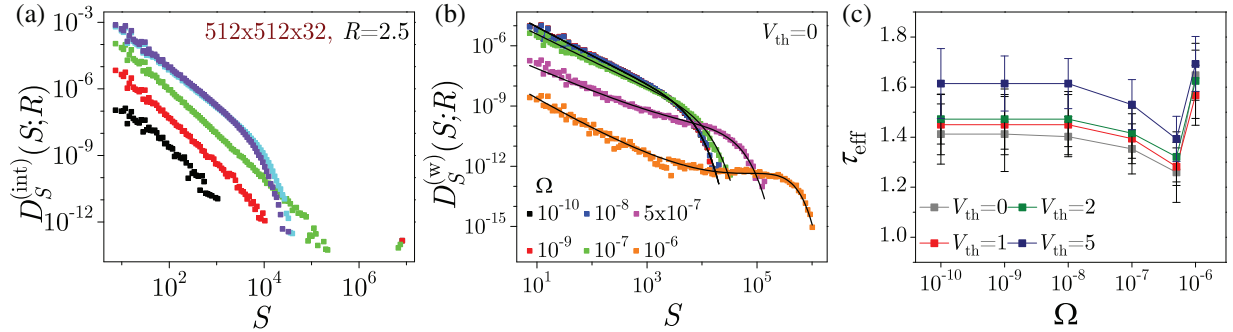


**Figure 35:** Integrated in (a), and windowed in (b) avalanche size distributions for the 3D systems with base  $512 \times 512$ , thickness  $l = 32$ , and disorder  $R = 2.5$ , driven at rates presented in legend. Data are averaged over up to 1300 RFCs. Windowed distributions are collected in the  $H$ -field windows with 5% change in magnetization around the coercive magnetic field. (c) Effective values  $\tau_{eff}$  (of the size distribution  $\tau$ -exponent) vs. driving rate  $\Omega$  for various threshold levels  $V_{th}$  shown in legend. This figure is replotted from Figs. 2, 3, and 4 from [172]

The integrated average avalanche shapes in the slow, intermediate, and fast driving regimes, as well as for different system thicknesses, are displayed in Fig. 36. It is evident that, at sufficiently low driving rates, the corresponding average shapes are symmetric and equal to adiabatic, irrespective of sample thickness. As the rate increases, the shapes begin to alter, becoming progressively more wide and flat due to temporal and/or spatial avalanche overlapping. Shape asymmetry happens at faster rates as well, and it's more noticeable in samples with the lowest levels of disorder.

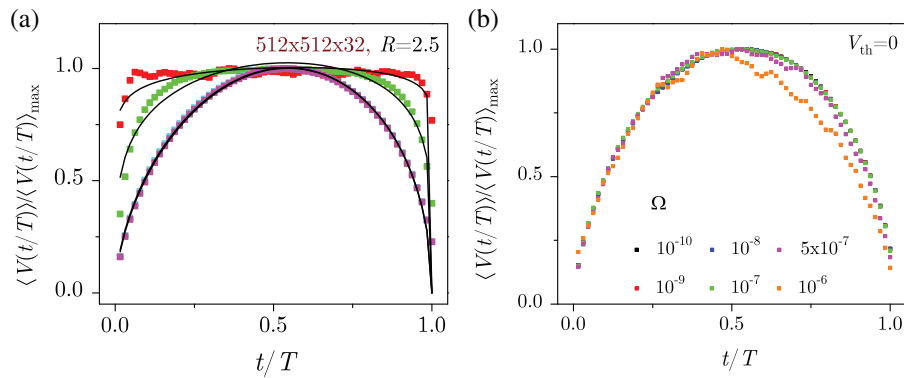


**Figure 36:** (a) Integrated average shapes of avalanches with fixed duration  $T = 64$  for the driving rates shown in the legend. The data corresponds to the systems with base  $512 \times 512$ , thicknesses  $l = 32$ , and disorder  $R = 2.5$ . All curves are obtained after averaging over 100 RFCs. (b) Windowed average avalanche shapes, collected in the  $H$ -field window with 5% change in magnetization around the coercive magnetic field. This figure is replotted from Figs. 5 and 7 from [172]

In addition to the integrated, average avalanche shapes are also calculated for the avalanches formed in the magnetic-field window centered at the coercive field and having width corresponding to the 5% range of magnetization. The system with lateral dimension  $l = 32$  and base  $512 \times 512$  with disorder  $R = 2.5$  is used as a representative, with application of the zero threshold level, shown

in Fig. 36b. The windowed average avalanche shapes are generally symmetric for slow driving and deviate from this shape when the rate is raised, much like in the integrated case.

The triggered integrated correlation functions are displayed in Fig. 37 for a system of a chosen thickness, driven with a set of rates spanning the entire range of driving regimes. These functions have a characteristic spanning-induced plateau at 1. When spanning avalanches (i.e., activity events) are present, the system’s behavior is dominated by them, and as a result, the correlation function’s shape has a plateau at all system thicknesses. Conversely, the beginning of a post-cutoff plateau can be observed for very large disorders and the slowest driving rates. This plateau’s level increases with the rate until it eventually saturates and overlaps with the main plateau. Similar observations were made previously for the equilateral 3D systems with finite driving [148].

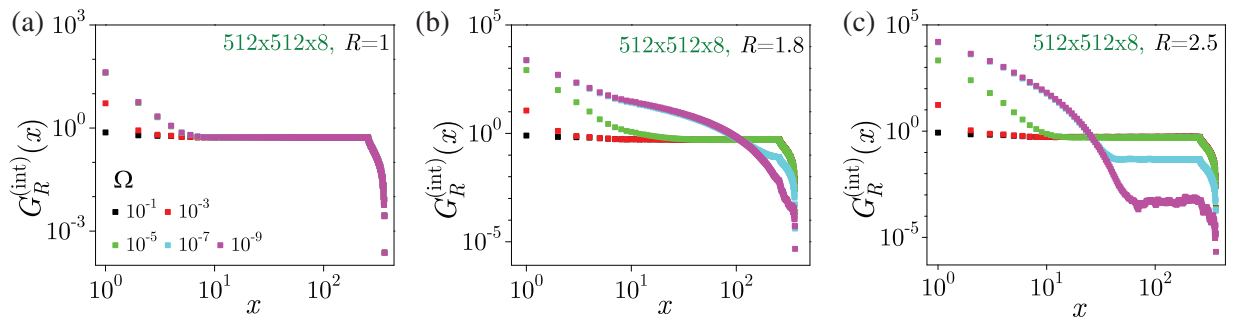


**Figure 37:** Variation with disorder  $R$  of the triggered integrated correlation functions driven at the rates shown in the panel (a) legend (valid for all panels) for systems with base  $512 \times 512$  and lateral dimension  $l = 8$ . The presented correlation functions correspond to disorders  $R = 1$  in panel (a),  $R = 1.8$  in panel (b), and  $R = 2.5$  in panel (c). Up to 100 RFCs are used to average the data. This figure is replotted from Fig. 8 in [172]

### 5.5 Disordered 3D Ferromagnetic Systems with Stochastic Driving

For simulating the complex phenomena with intermittent avalanche dynamics, deterministic external driving has typically been used with a well-defined protocol. In order to get as close as possible to the realistic scenario, a new driving method was proposed in the recent study [196], in which the external field takes stochastic increments within the framework of the ZT NEQ RFIM. This mimics realistic occurrences and potentially enables the results to be extended to the study of some difficult-to-achieve natural phenomena (e.g., earthquakes).

The results show that, provided the permitted range of field increments is small, the behavior is comparable to that of a constant-rate driven system. The system reacts in a complex way when the width of this range is expanded so that larger field increments are allowed. The scaling of the power laws is preserved and demonstrated for the distributions of avalanche parameters, average avalanche size of a given duration, and power spectra, whereas the deviations due to stochastic driving are found for the magnetizations and correlation functions.

Fig. 38 shows the integrated distributions of avalanche sizes, durations and waiting times. One can see that in the slow regime with small enough stochastic increments of the external field the distributions are practically the same as in the case of driving with a constant and small driving rate, while for the bigger stochastic steps, the differences start to emerge. Spanning avalanches are also generated, shown in the distributions as isolated points occurring after the cutoff region. As a consequence, the slope of distributions is also changed, reflected in the variation of the corresponding

exponent values. The flows of the effective rate-dependent values of exponents are shown in pertinent insets against the logarithmic width  $\log(\Omega_{\max}/\Omega_{\min})$  of the stochastic increment range.

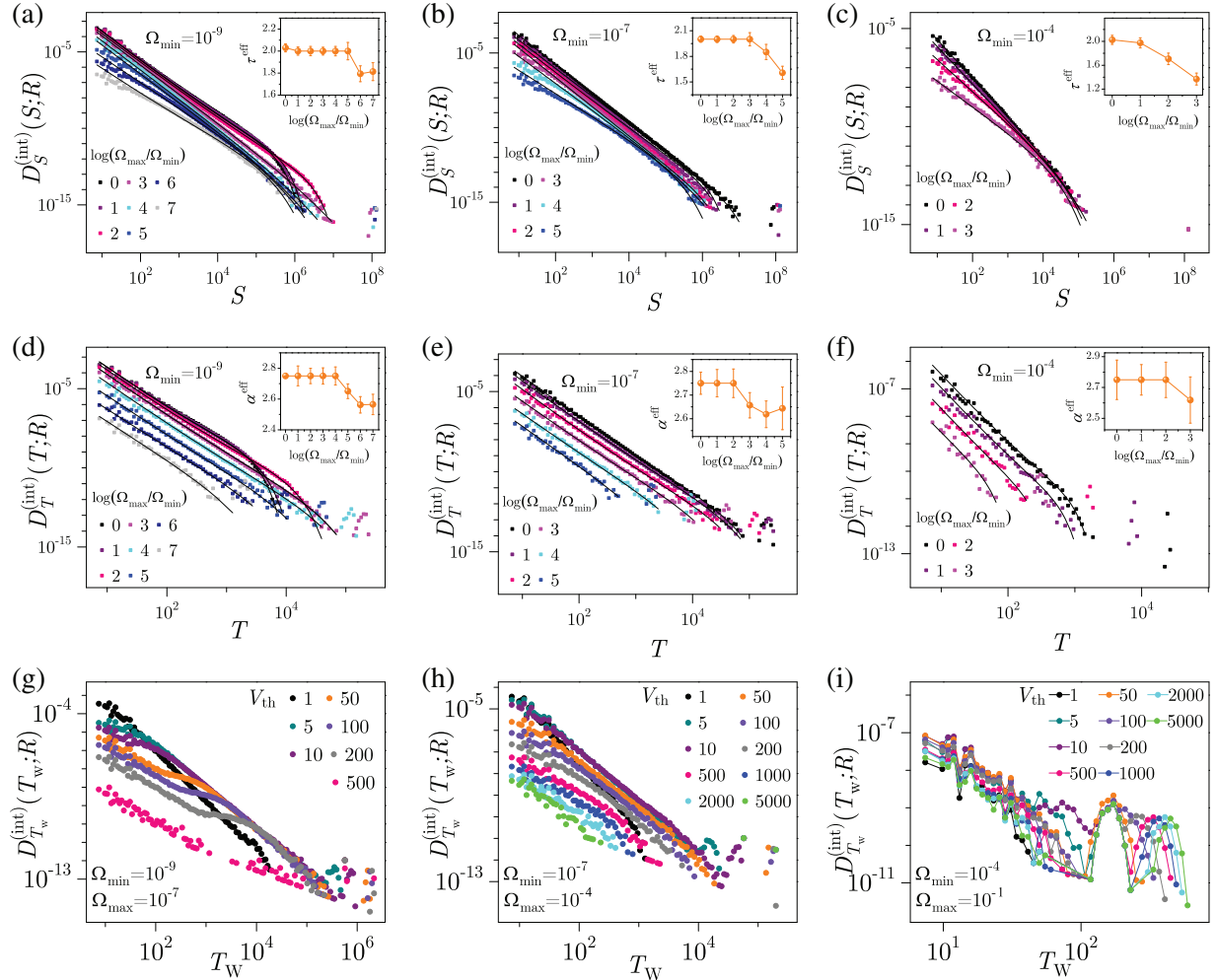


**Figure 38:** Integrated distributions of avalanche size (in (a)–(c) panels), duration (in (d)–(f) panels), and waiting time (in (g)–(i) panels) for the slow, intermediate and fast minimum stochastic driving rates  $\Omega_{\min}$  collected in a wide set of ranges of the stochastic increments of the external field. System size is  $L = 512$ , disorder  $R = 2.3$ , and the data are averaged over 100 RFCs. The values of the pertinent effective exponent  $\tau^{\text{eff}}$ , estimated by fitting the size distributions  $D_S^{(\text{int})}(S;R)$ , are shown in the corresponding insets against the logarithmic width  $\log(\Omega_{\max}/\Omega_{\min})$  of the range of the stochastic external field increments; fits are shown in main panels with full black lines. Presented error bars in insets are augmented 3–5 times for better visibility. In this figure are combined Figs. 4, 5 and 8 from [196]

Additionally, in Fig. 39, preservation of the power-law dependence of average avalanche size of a given duration for the case of stochastic driving is showcased, as well as for the power spectra showing that this scaling holds only for narrow intervals of  $\Delta H$  increments in the slow and intermediate stochastic regimes, being violated in the fast driving regime. Regarding the integrated triggered activity

correlation function, one can see that the characteristic plateaus, indicating the presence of spanning avalanches, are shown in the shapes of the correlation function as well. For the case of a small range of permitted stochastic field increments we see the plateau at a level below 1, which is the same adiabatic-like behavior previously observed for the constant rate driving in the limit of small rates.

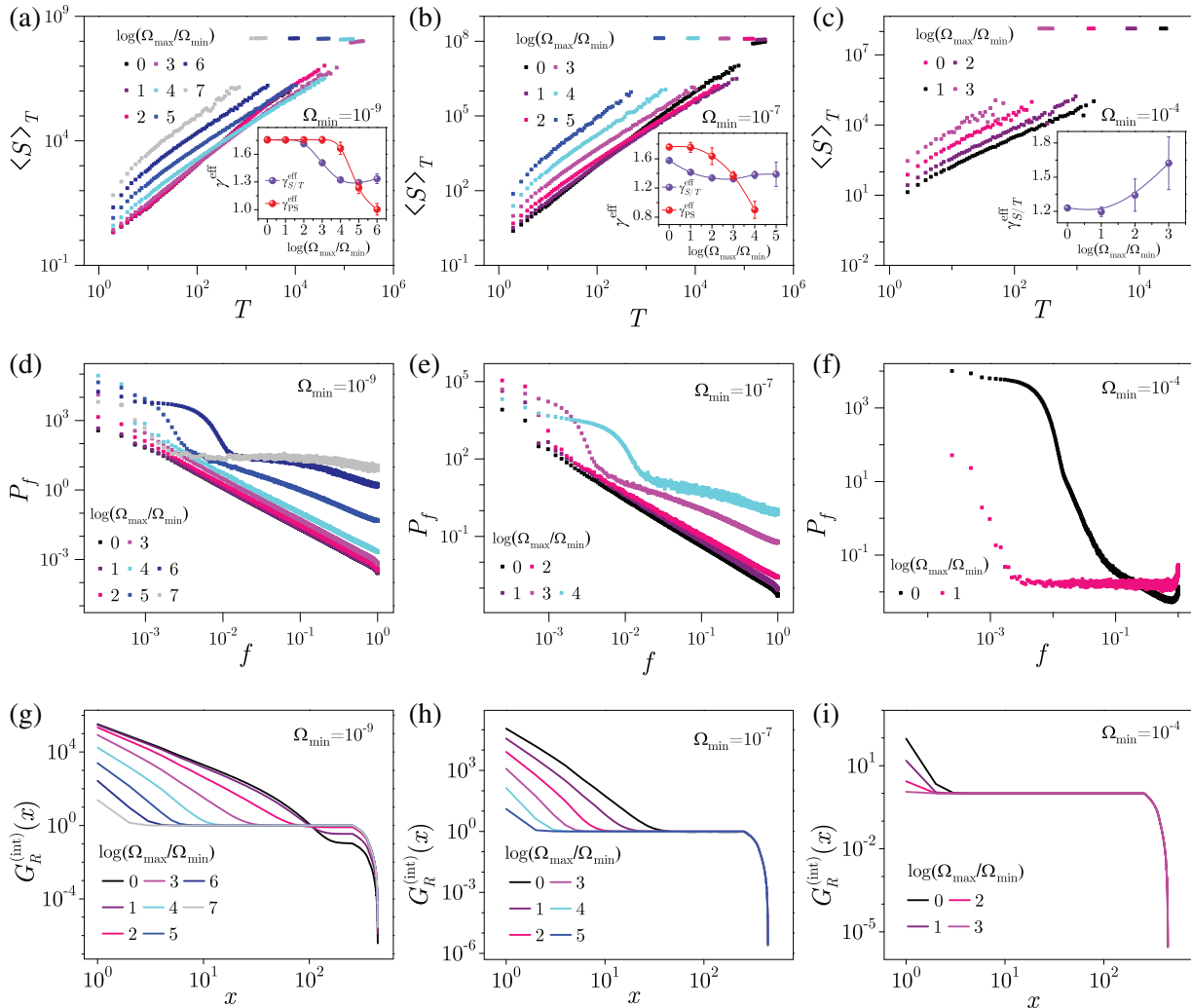


**Figure 39:** (a)–(c) Average size  $\langle S \rangle_T$  of avalanches with duration  $T$ , against this duration. (d)–(f) Power spectra  $P_f$  vs. frequency  $f$  for the slow, intermediate and fast stochastic driving regimes in a wide set of ranges of the stochastic external field increments. (g)–(i) Integrated triggered activity event correlation functions  $G_R^{(int)}(x)$  vs. inter-spin distance  $x$ . This is Fig. 9 from [196]

Moreover, it is discovered that there is a high degree of consistency between the data from numerical simulations and the experimental data from fracture experiments, which demonstrate seismic-like behavior, and acoustic emission experiments of single crack propagation in inhomogeneous solids. This suggests that when complex systems generate intermittent, scale-free avalanche dynamics, there is a general underlying process that reproduces empirical rules, like Gutenberg-Richter’s law of earthquakes. Fig. 40 presents the comparison of the integrated energy distributions obtained in the

numerical simulations of stochastically driven RFIM with the corresponding distributions obtained in acoustic emission experiments of a single crack propagation in inhomogeneous solid and fracture experiments [142] for which the seismic-like behavior is demonstrated.

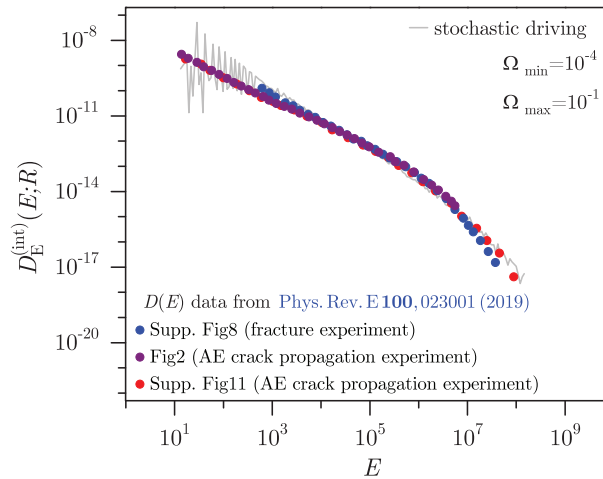


**Figure 40:** Comparison of integrated energy distributions, obtained in numerical simulations with stochastic driving (for system with size  $L = 256$ , disorder  $R = 2.3$ , and the field increments within the range  $(\Omega_{\min}, \Omega_{\max})$  from legend), and the data from [142], obtained in experimental measurements of acoustic emissions during the crack propagation and fracture experiments [142], shifted in this figure along both horizontal and vertical logarithmic axes in order to achieve the overlapping with the simulation data. This is Fig. 11 from [196]

## 6 Towards More Realistic Modeling: The Impact of Thermal Fluctuations and Demagnetizing Fields

Modelling driven disordered systems in a way that closely resembles experimental settings is a challenging endeavor due to the multitude of connected factors that impact their nonequilibrium dynamical behaviour. In a recent study on the effects of demagnetizing fields and thermal fluctuations of a thin ferromagnetic samples [164], the numerical simulations of the extended version of RFIM were conducted implementing novel algorithmic techniques. In this study, the magnetic field is cycled from the saturated hysteresis loop through a series of nested subloops gradually reducing to zero, forming along the demagnetization curve from the tips of all simulated subloops (see an example in the top left panel of Fig. 41).

Using the thermal scenario (i.e., with the non-zero temperature) affects the values of the coercive field and remanent magnetization, causing the shrinking of the hysteresis loop and amplifying minor activity events. The temperature effects on the saturation loops and relevant demagnetization curves of the demagnetized system are shown in the middle panels of Fig. 41. The saturation magnetization loops exhibit a sharp rise at lower temperatures, gradually shrinking in width as temperature rises. This dissolves the hysteresis and brings the rising and descending branches into overlap, with the coercive field tending towards zero. In parallel, the characteristic plateau of demagnetization curve remains in the range of lower temperatures, gradually shrinking as the temperature rises and ultimately dissolving, smoothing the demagnetization curve.

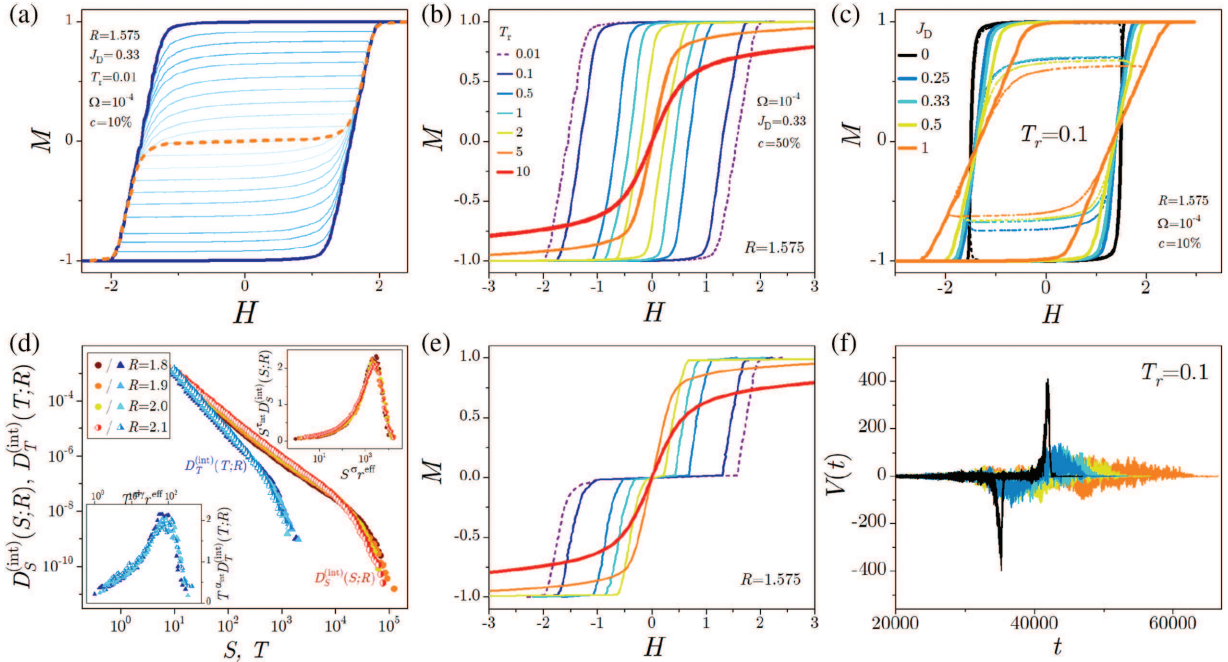


**Figure 41:** (a) Saturation hysteresis loop (full thick curve) with 10 subloops (shown out of 50 by thin full curves) and the demagnetization (dashed) curve. (b) Shrinking of single-run saturation magnetization curves with increasing relative temperature. (c) Single-run magnetization loops *vs.* simulation time  $t$  for the range of  $J_D$  values from the legend and fixed temperature  $T_r = 0.1$ . (d) Integrated distributions  $D_S^{(int)}(S; R)$  of size  $S$  (circles) and  $D_T^{(int)}(T; R)$  of duration  $T$  (triangles) of activity events, for a set of disorder values  $R > R_c^{eff}$ . Presented data are averaged over 20 RFCs. Insets show pertinent scaling collapses obtained for exponents  $\tau_{int} = 1.95 \pm 0.09$ ,  $\alpha_{int} = 2.60 \pm 0.02$ ,  $\sigma = 0.98 \pm 0.04$ ,  $\sigma\gamma = 1.01 \pm 0.03$ , and  $R_c^{eff} = 1.575 \pm 0.108$ . System size is  $256 \times 256 \times 4$  with parameters from the legend. (e) Demagnetization curves for the simulation parameters quoted in the legend of panel (b). (f) Response signals  $V(t)$  *vs.* simulation time  $t$  for the range of  $J_D$  values from panel (c) and fixed temperature  $T_r = 0.1$ . Presented data are replotted from [164], combining Figs. 1 and 6, and parts of Figs. 2 and 3

Conversely, the demagnetizing field introduces the prolonged linear segments in the loops and alters the multifractal nature of the magnetization fluctuations. The right panels of Fig. 41 display the effects of varying the  $J_D$  coefficient over a wide range of values alongside the corresponding time profiles of the system's response signal  $V(t) = n_+(t) - n_-(t)$ , expressed in terms of the numbers  $n_+(t)$  and  $n_-(t)$  of spins that flip up and down at the moment  $t$  during one time-step. As the demagnetizing factor  $J_D$  increases, the virtually rectangular saturation loops for  $J_D = 0$  start to become more and more slanted, while the coercivity and remanent magnetization stay constant. Compared to the situation without the demagnetizing fields, the emergence of a sizable linear section lengthens the hysteresis loop's central part and delays the magnetization reversal process. These changes of the hysteresis shape may result in an altered role of disorder due to these long-range effects. Theoretically, a crossover from the disorder-induced critical point to a self-organized critical behavior [197] may occur, in analogy to the driving-induced crossover revealed in [198]. Another example to mention in this context is the hysteresis behavior in the infinite-range spin glasses [199].

The integrated distributions  $D_S^{(\text{int})}(S; R)$  and  $D_T^{(\text{int})}(T; R)$  of activity events realized during the whole hysteresis loop are displayed in Fig. 41d. The corresponding critical exponents characterize their power-law scaling, which comes to an end in a cutoff region. As indicated in the insets of this panel, the  $D_S^{(\text{int})}(S; R)$  and  $D_T^{(\text{int})}(T; R)$  distributions collapse in accordance with

$$D_S^{(\text{int})}(S; R) = S^{-\tau_{\text{int}}} \mathcal{D}_S(S^\sigma r), \quad (53)$$

$$D_T^{(\text{int})}(T; R) = T^{-\alpha_{\text{int}}} \mathcal{D}_T(T^{\sigma\gamma} r), \quad (54)$$

where  $\mathcal{D}_S$  and  $\mathcal{D}_T$  are the appropriate universal scaling functions and all exponents have the values pertinent to the 2D adiabatically driven ZT NEQ RFIM [89].

### 6.1 Details of the Developed Numerical Algorithm

A more realistic modeling of the hysteresis loop phenomena in disordered ferromagnetic samples is introduced in [164] incorporating thermal and demagnetization field effects with possible extensions to heterostructures and thin films which are all the subject of numerous applications at the moment. This approach, which is computationally more efficient for thermal simulations than the one proposed in [166], selects a given fraction  $c$  of spins at random and checks if they are thermally flippable at the current  $H$  value, while the rest of the spins are checked according to the field-flipping conditions. These criteria are more suited to a low-temperature fixed point in the relevant field-theory models since they give greater weight to the field-flipping than thermal-flipping, particularly for small values of  $c$ , controlling the number of ongoing thermal spin-flipping attempts in between two consecutive discrete changes of the external magnetic field. Even though the algorithm permits the limit  $c = 1$  with fully developed thermal fluctuations near the temperature-dominated fixed point, it uses two independent parameters  $T_r$  and  $c < 1$  to enable better control over the time scale separation, keeping the system near the low-temperature disorder-dominated fixed point where thermal fluctuations are subject to the dynamics of avalanche spreading and driving.

In Fig. 42, we present the flowchart of a single-run algorithm used in [164], and its key points we summarize as follows:

- The single-run simulation input parameters are the size  $(L, L, l)$  of the lattice (determining the number of spins in the system  $N = L^2 \times l$ ), the seed for the random number generator used in generating the configuration  $\{h_i\}_{i=1}^N$  of the quenched random field, the disorder parameter  $R$ , the demagnetization field coefficient  $J_D$ , relative temperature  $T_r$ , the fraction  $c$  of thermally flippable spins, the value of  $\Delta H$  (setting the driving rate  $\Omega = \Delta H / \Delta t$ ), the number  $N_{\text{sl}}$  of subloops and the corresponding sequence  $\{H_k^{(\text{max})}\}_{k=1}^{N_{\text{sl}}}$  of the maximum external field values in the subloops.
- For the supplied value of seed, the (Gaussian) random field configuration  $\{h_i\}_{i=1}^N$  is formed with the aid of the numerical procedure named RNFARR from [200] for generation of uniform deviates in  $(0, 1)$  interval; the saturated hysteresis loop simulation is initialized by setting  $s_i = -1$  for all spins and  $H$  to the maximum negative value such that all spins are field-stable.
- In each (new) time step the external magnetic field  $H$  is changed by  $\Delta H$ .
- After  $H$  is changed, all spins are in parallel tested and (possibly) flipped following the steps:
  - the effective magnetic field  $h_i^{\text{eff}}$  and the thermal flipping probability  $p_i^{\text{eff}}$  are calculated for each spin  $s_i$ , see (2) and (3) in Section 2.
  - random numbers  $r_i^{(\text{sel})}$  and  $r_i^{(\text{th})}$  are generated from the uniform distribution in the closed interval  $[0, 1]$  for each index  $i$ .

- for  $s_i$  that is:
  - \* field-unstable,  $s_i$  is flipped
    - if  $r_i^{(\text{sel})} > c$
    - or( $r_i^{(\text{sel})} < c$  and  $r_i^{(\text{th})} < p_i^{\text{eff}}$ )
  - \* field-stable,  $s_i$  is flipped if ( $r_i^{(\text{sel})} < c$  and  $r_i^{(\text{th})} < p_i^{\text{eff}}$ )
- When  $H < H_k^{(\text{min})}$  for the first time on the falling part of the current  $k$ -th (sub)loop, the initial spin state  $\{s_i^{(k+1)}\}_{i=1}^N$  for the next (i.e.,  $k + 1$ -th) subloop is stored.
- After  $H$  falls below the  $H_k^{(\text{min})}$  for the first time on the falling part of the current ( $k$ -th) (sub)loop, the simulation of the rising part of the next (i.e.,  $k + 1$ -th) subloop is initiated by restoring the spins to the initial spin configuration  $\{s_i^{(k+1)}\}_{i=1}^N$  and  $H$  to  $H_{k+1}^{(\text{min})}$ .

Quenched averaging is performed over different RFCs using the same input parameters.

## 7 Collective Magnetization Fluctuations and Structure of Barkhausen Noise (BHN) in Experiments and Theory

As stated in the Introduction, the magnetization reversal in disordered ferromagnets is a stochastic process related to the motion, pinning and depinning of domain walls driven by slow ramping of the external magnetic field. Such motion is accompanied by a ‘crackling noise’ signal [201], known as the Barkhausen noise (BHN). It represents a time series of the magnetization changes during the reversal processes and is measured in the experiments. Given the avalanching dynamics related to the critical behaviour of the hysteresis-loop discussed above, the related BHN signals have a vibrant structure. For example, the BHN signal possesses long-range temporal correlations seen in the power spectrum and multi-scale fractality [33]; moreover, the sequence of avalanches represents another structured set characterized by Tsallis q-Gaussian distribution of the first returns [202]. Hence, the appropriate analysis of BHN signals can reveal valuable information about the stochasticity of the magnetization reversal process and quantify its dependence on relevant parameters [203]. In this section, we first demonstrate how the magnetization avalanches are extracted from the experimental BHN signal. Next, we show that the BHN distributions, measured in a nanocrystalline sample, are adequately described by the ZT NEQ RFIM with suitably selected parameters [168]. Furthermore, we give a more detailed description of the multifractal analysis of the BHN signals simulated by RFIM in different conditions. We define the appropriate quantitative measures and demonstrate their sensitivity to varied parameters by considering two representative examples.

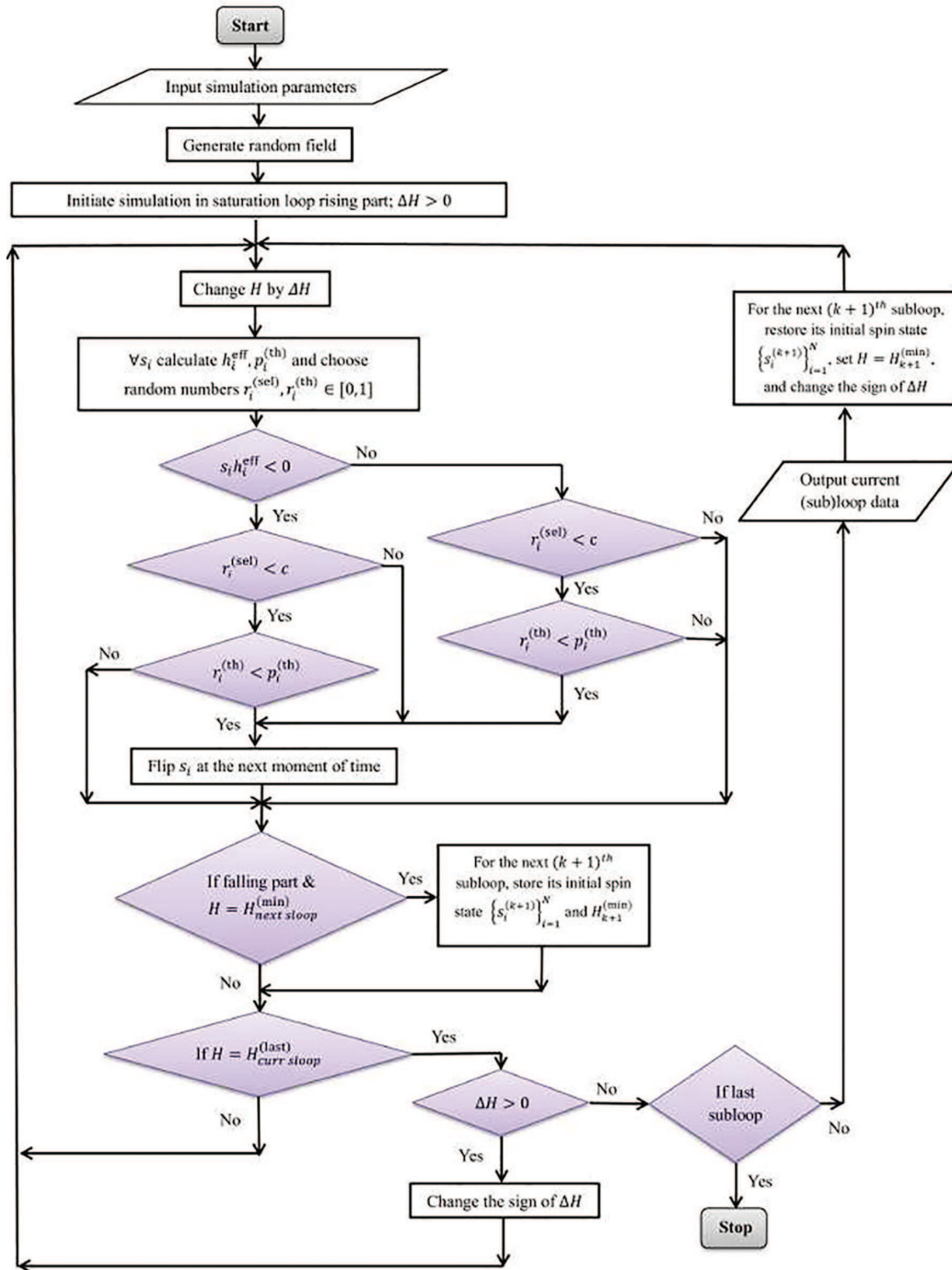


**Figure 42:** A flowchart of the single-run algorithm used in numerical simulations of the RFIM version incorporating demagnetizing field [164]. The dashed curve encloses the parallelized part of the algorithm. This figure is replotted from Fig. 7 from [164]

### 7.1 RFIM Simulations Compared with the Real Samples' BHN Avalanches

In this subsection, we give a comparison between the BHN emitted by a real sample and the RFIM version adjusted to give as close as possible matching with the experimental data reported in [168]. BHN recordings were performed with the experimental setup schematically depicted in Fig. 43 on an annealed (at 300°C) 16 cm × 1 cm × 40 μm VITROPERM 800 R (Vacuumschmelze GmbH) metallic glass sample having very small demagnetizing factor (= 0.00053) and homogeneously distributed magnetically coupled monodomain ferromagnetic nanocrystalline grains whose magnetic dipole moments are possible to model with single spins. As the recordings were performed at room temperature which is far below the Curie temperature (= 600°C) of this material, the temperature fluctuations can be considered absent in its modeling. For the foregoing reasons, the athermal ZT NEQ RFIM on the 3D cubic lattice (with the same aspect ratio as the real specimen) can be considered as adequate for modeling of the BHN emitted from such a sample.

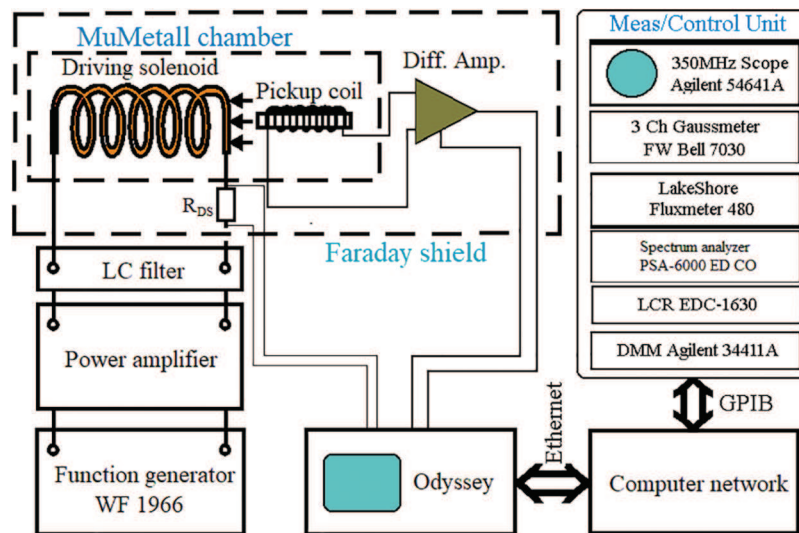


**Figure 43:** Scheme of the experimental setup used in BHN measurements. This is Fig. 1 in [168]

In BHN inductive recordings, the response signal is the voltage (i.e., electromotive force) induced in a pickup coil tightly wound around the sample. This voltage is amplified approximately 2000 times by an ultra-low noise differential amplifier, and registered and A/D converted by a Nicolet Odyssey data acquisition system. The pickup coil with the sample was placed in the middle of a driving solenoid making inside it a homogeneous external magnetic field generated by the current with a triangular time profile supplied by a power amplifier and a function generator. The sample, pickup coil, driving solenoid, and differential amplifier were inside a four-wall magnetic shielding and an aluminum Faraday cage with 1 cm thick solid walls. Due to such shielding and battery-operated amplifiers, the recorded BHN was virtually free from the external electromagnetic noise and pollution penetrating from the electric network, as well as from the external static and low-frequency environment electric and magnetic field.

One period of the response signal, sampled 200,000 times per second at the resolution of 14 bits, is presented in Fig. 44 for seven driving frequencies from the range 0.5–50 mHz. The corresponding hysteresis loops are shown in the right insets, while the left insets illustrate the appearance and distribution of the overall system noise collected near the tip of the hysteresis loop where the contribution due to changes in magnetization caused by time-varying external magnetic field is absent.

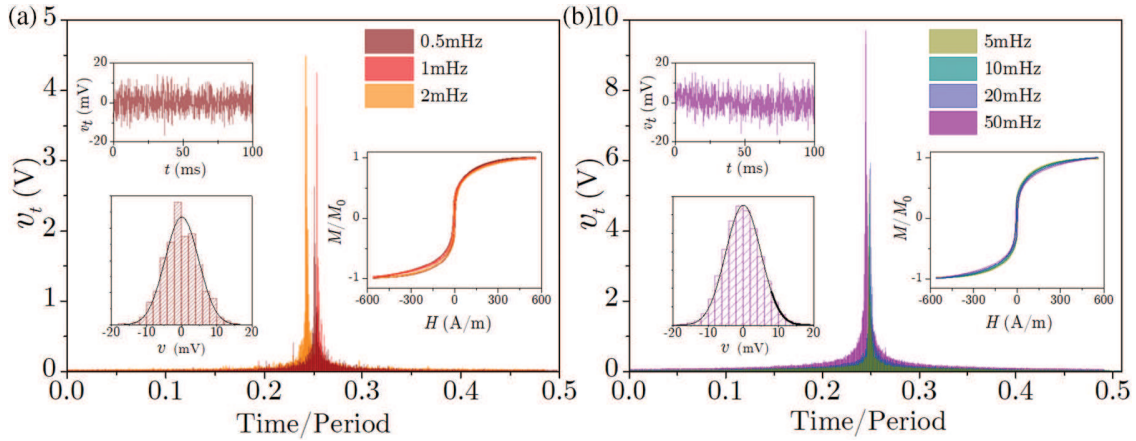


**Figure 44:** The main panels show one example of time profiles of the voltage response signal  $v_t$  recorded during a single half-period of the external driving field  $H$  for each of the employed ‘slow’ (panel (a)) and ‘fast’ (panel (b)) driving frequencies  $\Omega$  quoted in legends. Top-left inset in the left main panel presents an excerpt of the time profile of the response signal recorded at  $\Omega = 0.5$  mHz near the maximum value of the external field  $H$ , while the histogram, presented in the bottom-left inset of the same panel, illustrates that these values of noise are normally distributed, which could be mainly attributed to random fluctuations in the sample’s magnetization. In the right panel, the left insets show the same, but for  $\Omega = 50$  mHz, while for the remaining frequencies, the corresponding distributions are roughly the same with the standard deviation less than 5 mV. Hysteresis curves, displaying  $v$  vs. the external magnetic field  $H$  the sample’s magnetization  $M$  scaled by maximum magnetization  $M_0$ , are given in the right insets. This is Fig. 3 in [168]

To enable comparison with the experimental data, simulational units are scaled so as to provide the best match for the two types of data. This is achieved by dividing the simulational timescale by the factor  $c_t = 2 \times 10^5$  (equal to the sampling rate used in the experiment) and the signal scale by the factor  $c_v = 50$  (hence, the factor  $c_t c_v = 10^7$  for the scale of avalanche size and the factor  $c_t c_v^2 = 5 \times 10^8$  for the scale of avalanche energy). Comparison between the experimental and (rescaled) simulational data, presented in Fig. 45 for the integrated distributions of avalanche size  $S$ , duration  $T$ , energy  $E$ , and amplitude  $A$  expressed in physical units (e.g., second for duration and volt for amplitude), reveals a remarkable matching suggesting the adequacy of the employed RFIM version for the simulations of the BHN emitted by the real ferromagnetic samples having a nanocrystalline grain structure.

Further matching supporting the preceding conclusion is illustrated in Fig. 46, in the case of correlations  $\langle S \rangle_T \propto T^\gamma$  and power spectra  $P(f)$ , dependence of the critical exponent  $\gamma$  on the choice of the imposed thresholds in Fig. 47, and the average avalanche shapes and distributions of various types of waiting time in Fig. 48.

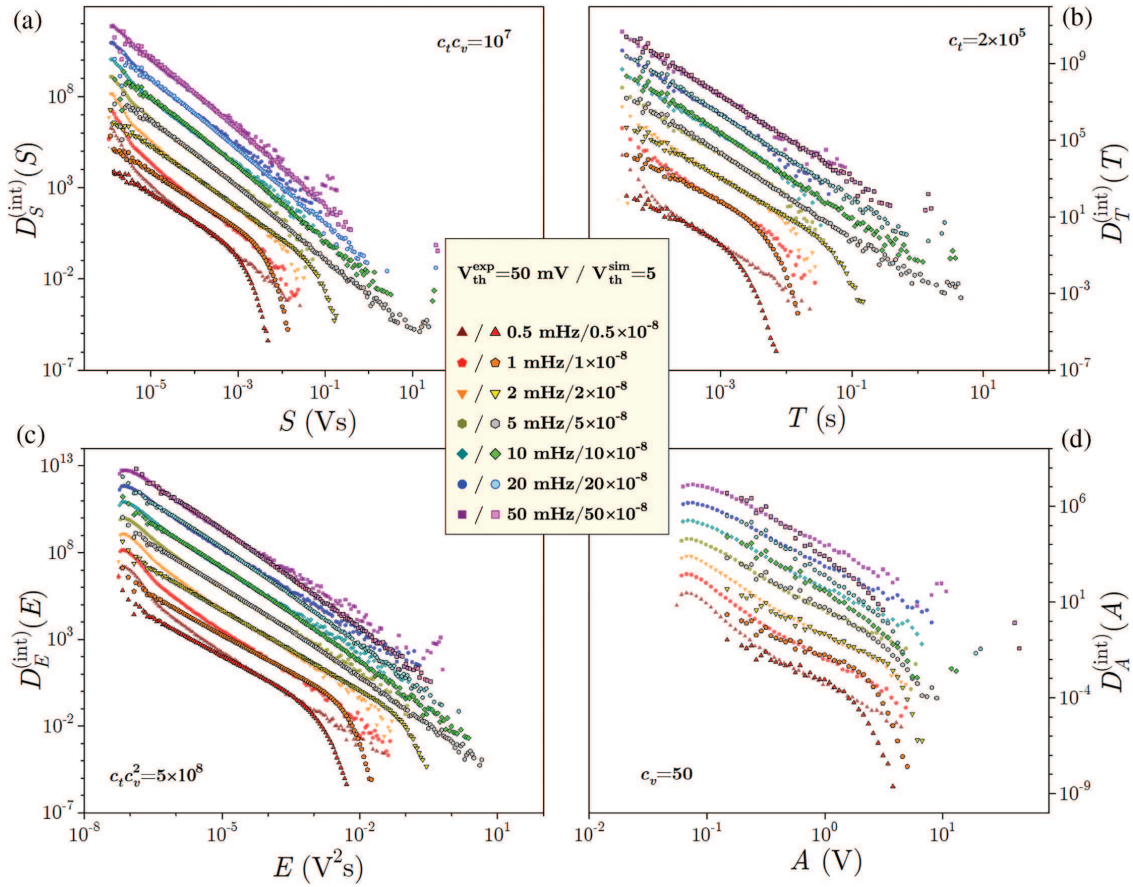


**Figure 45:** Comparison of integrated (unit area) distributions of avalanche parameters, size  $S$  in (a), duration  $T$  in (b), energy  $E$  in (c), and amplitude  $A$  in (d), obtained in experiments and numerical RFIM simulations on the  $32,768 \times 2048 \times 8$  striplike cubic lattice for the experimental (simulation) driving rates quoted in the common legend. Each experimental distribution is extracted at the (same) experimental base threshold  $V_{th}^{exp} = 50$  mV of 20 hysteresis cycles data and presented with full symbols on the requisite scale using SI units for time and voltage. Starting from the distribution recorded at the lowest driving rate, each experimental distribution obtained at the next (higher) rate is for better visibility vertically translated by one decade upwards relative to the distribution recorded at the previous (lower) rate. Each simulational distribution is extracted at the (same) simulational base threshold  $V_{th}^{sim} = 5$  of 20 RFIM simulations performed with different RFCs with disorder  $R = 2.3$ . For comparison, the simulational distributions, presented by empty symbols, are shifted along the horizontal axis dividing the data by a suitable factor ( $c_t = 2 \times 10^5$  for  $T$ -axis,  $c_v = 50$  for  $A$ -axis,  $c_t c_v = 10^7$  for  $S$ -axis, and  $c_t c_v^2 = 5 \times 10^8$  for  $E$ -axis). This is Fig. 8 from [168]

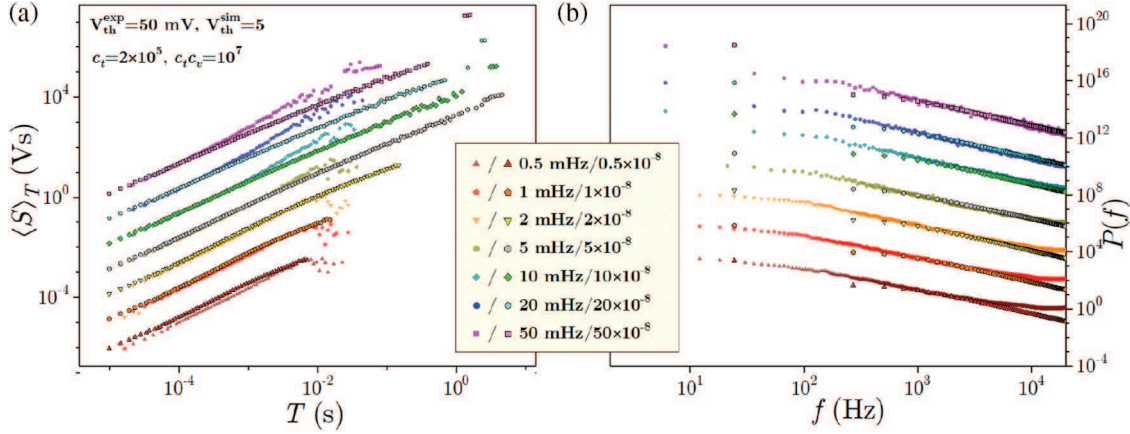


**Figure 46:** (a) Experimental and simulational correlations between the avalanche duration  $T$  and the average avalanche size  $\langle S \rangle_T$  of that duration extracted at the same experimental and simulational base thresholds, the same values of experimental and simulational driving rates, and the same  $c_l$  and  $c_l c_v$  factors as in Fig. 45. (b) Comparison of the experimental and simulational power spectra  $P(f)$  for the driving rates from the legend. Simulational frequencies are multiplied by the factor  $c_l = 2 \times 10^5$ . For visibility, each of the next-driving-rate curves in both panels is shifted vertically upwards by one-two decades in left-right panel relative to the previous one. The underlying sets of data are the same as in Fig. 45. This is Fig. 9 in [168]

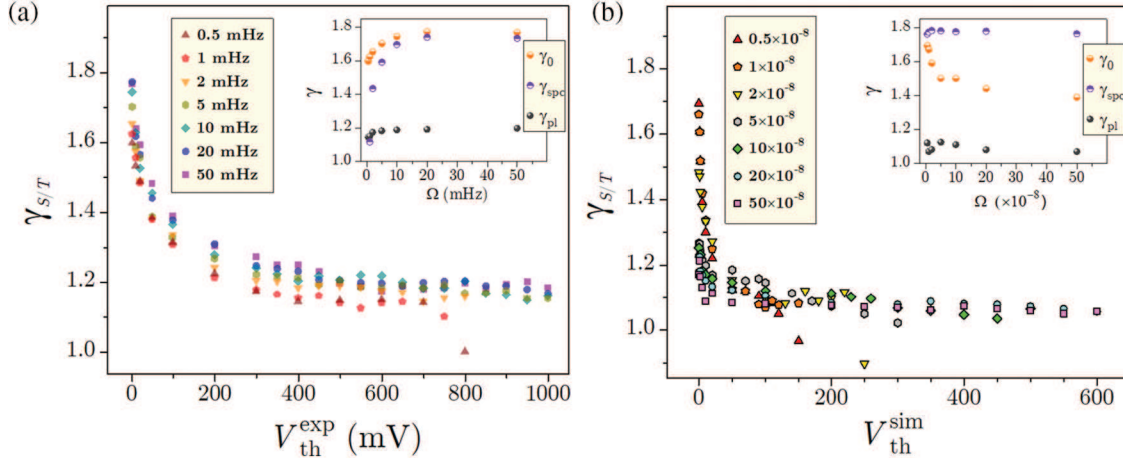


**Figure 47:** (a) Effective experimental values of the exponent  $\gamma_{S/T}$  against the base threshold  $V_{th}^{exp}$ . In the inset, we show against the driving rate  $\Omega$  the effective experimental values of  $\gamma_0$  (i.e., the value of  $\gamma_{S/T}$  at the current driving rate  $\Omega$  for the smallest experimental base threshold  $V_{th}^{exp} = 1$  mV),  $\gamma_{spc}$  (i.e., power spectrum exponent values), and  $\gamma_{pl}$  (i.e., plateau value of the exponent  $\gamma_{S/T}$  at the corresponding driving rate  $\Omega$ ). (b) The same as in (a), but for the values obtained from the simulational data. Each effective exponent value is the slope determined by the linear fit in the power-law region of the corresponding distribution. The underlying data sets and other relevant parameters are the same as in Fig. 45. This is Fig. 10 from [168]

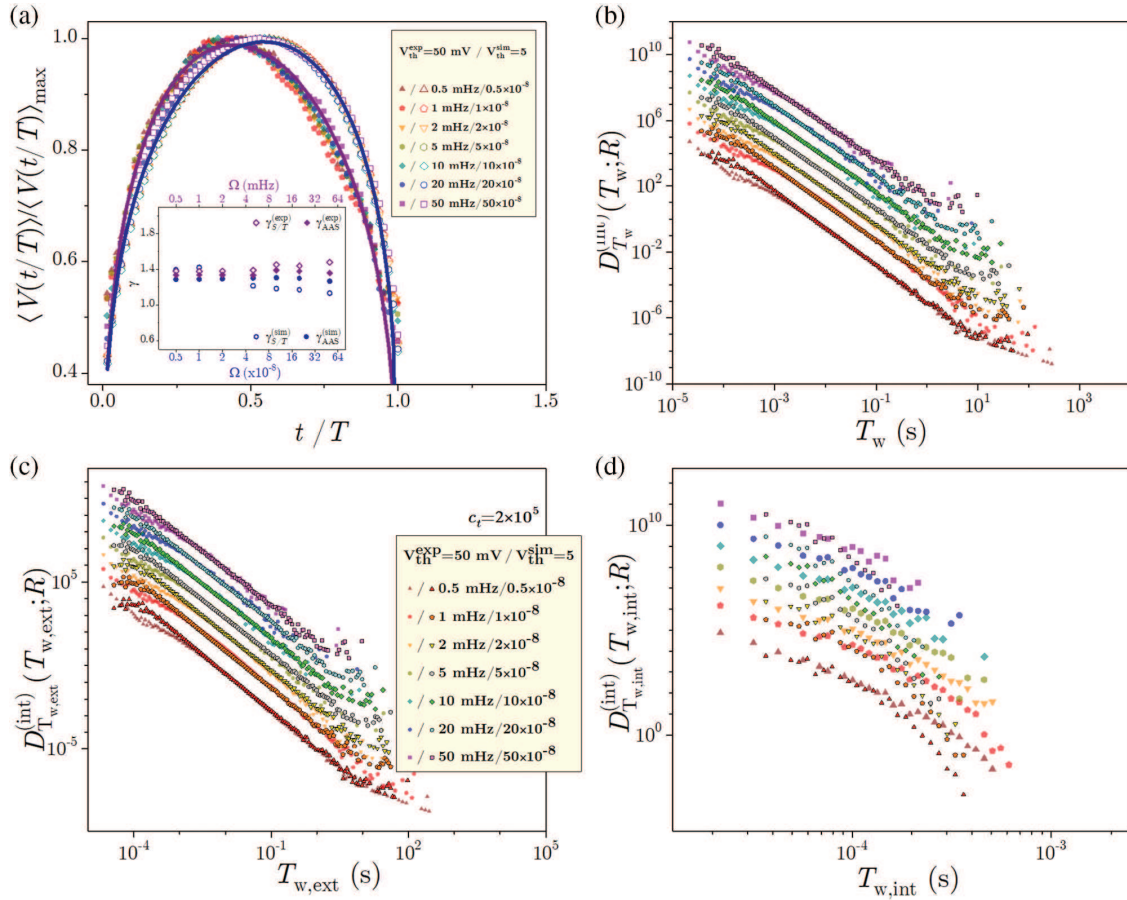


**Figure 48:** (a) Experimental/simulational average avalanche shapes shown in the main panel by filled/empty symbols and the values of exponents  $\gamma_{S/T}$  and  $\gamma_{AAS}$  in inset. Experimental and simulational distributions of waiting times, total in (b), external in (c), and internal in (d); the legend in (c) applies to all waiting time distributions. In this figure are combined Figs. 11 and 12 from [168]

## 7.2 Multifractal Analysis of BHN Reveals Impact of Relevant Parameters

The multifractality of time series manifests in nontrivial scaling properties of the generalized fluctuation function  $F_q(n)$  of time interval  $n$ , where the amplification parameter  $q$  takes a range of real values. We use the detrended multifractal analysis for the magnetization changes  $\{m_t\}$  at time  $t$ , where  $t = 1, 2, \dots, t_{\max}$ , consisting a time series with  $N$  nonzero data points. According to the procedure described in [33,204,205], the profile  $Y(i) = \sum_{t=1}^i (m_t - \langle m \rangle)$  is constructed and divided into  $N_s = \text{int}(N/n)$  non-overlapping intervals of the length  $n$  starting from the beginning of the time series. As the interval  $n$  is often not an integer fraction of  $N$ , the process repeats starting from the end, resulting in total  $2N_s$  intervals. The local trend  $y_\mu(i)$  is determined by a polynomial fit at each interval  $\mu = 1, 2, \dots, 2N_s$ . Then, the standard deviation

$$F^2(\mu, n) = \frac{1}{n} \sum_{i=1}^n [Y((\mu - 1)n + i) - y_\mu(i)]^2 \quad (55)$$

is determined at each interval for  $\mu = 1, 2 \dots N_s$  starting from the beginning of the time series. Similarly,

$$F^2(\mu, n) = \frac{1}{n} \sum_{i=1}^n [Y(N - (\mu - N_s)n + i) - y_\mu(i)]^2 \quad (56)$$

for  $\mu = N_s + 1 \dots 2N_s$ , starting from the end point. Then the  $q$ -th order fluctuation function  $F_q(n)$  for different interval length  $n \in [2, \text{int}(N/4)]$  is determined as

$$F_q(n) = \left\{ \frac{1}{2N_s} \sum_{\mu=1}^{2N_s} [F^2(\mu, n)]^{q/2} \right\}^{1/q} \sim n^{H_q} \quad (57)$$

where the parameter  $q$  is varied over a range of positive and negative values to test its scaling properties.

The scale-invariant segments of  $F_q(n)$  for each  $q$  line is identified as a straight line in the log–log plot, and the scaling exponent  $H_q$  is determined according to (57). The spectrum of the  $H_q$  values, representing the generalised Hurst exponent, and the difference  $\Delta H_q$  between its largest and smallest value serve as a measure of the signal's multifractality [33,205]. Note that for a mono-fractal  $H_q = H_2$  for all  $q$  values equals the standard-deviation Hurst exponent. Another multifractal measure is well-known *singularity spectrum*  $\Psi(\alpha)$ , where  $\alpha$  values indicate the power-law singularities observed along the time series. The singularity spectrum is readily determined from the  $H_q$  spectrum [205] by the Legendre transform

$$\Psi(\alpha) = q\alpha - \tau_q, \quad (58)$$

where  $\alpha = d\tau/dq$  and  $\tau_q = qH_q - 1$  stands for the scaling exponent known in the familiar probability function approach [205]. In this context,  $\Psi(\alpha)$  represents the fractal dimension of the subset of data points with the singularity exponent  $\alpha$  along the time series.

Using a couple of representative examples, we demonstrate how the multifractal features of the BHN vary with the pertinent parameters and thus quantify their relevance to the magnetization reversal processes. As stated above, the multifractal features of BHN are tightly related to the collective (avalanching) magnetization fluctuations that also manifest in the long-range temporal correlations; they are often seen in the region of high-frequencies  $f$  of the power spectra according to the scale-invariant decay

$$P(f) \sim Bf^{-\gamma}. \quad (59)$$

The collective dynamic behavior in the BHN signals is not just a concept but a quantifiable reality. We further solidify this understanding by considering the temporal sequence of distinct avalanches. For example, the difference in the size of two consecutive avalanches  $\Delta = S_i - S_{i-1}$  (the first return) exhibit  $q_e$ -Gaussian distributions

$$P(\Delta) = A \left[ 1 - (1 - q_e) \left( \frac{\Delta}{\Delta_0} \right)^2 \right]^{1/1-q_e}, \quad (60)$$

that universally appear in different complex dynamical systems out of equilibrium [202], where  $q_e$  is the Tsallis non-extensivity parameter [206].

### 7.2.1 Multifractality of BHN Varies with Demagnetizing Effects

As an interesting example, we analyze the structure of BHN signals simulated at low temperatures and varied demagnetizing factors by the extended RFIM (excluding the dipolar interactions term) in Eq. (1). For this purpose, we consider quasistatic driving, where the field increases for a given amount after an avalanche has stopped. It allows us to identify the impact of the propagation of individual avalanches on the magnetization fluctuations. We refer to Section 4.1 for more details on the quasistatic driving and Section 6 for the impact of demagnetizing fields on the shape of the hysteresis loop.

As stated above, the presence of demagnetizing fields induces long-range interactions counteracting the external magnetic field; they affect the shape of the hysteresis loop, in particular, introducing the extended linear segment in the central part of the loop, and potentially change the nature of critical behaviour; see Fig. 41. The magnetization reversal process is prolonged compared with the case without the demagnetizing fields ( $J_D = 0$ ), which also manifests in the structure of the BHN. For example, Fig. 49 shows a segment of the prolonged reversal time series with characteristic alternation of small and large deviations. Such fluctuations affect the multifractal properties of BHN signals, compared to the studied cases without demagnetizing fields in 3D and thin RFIM systems [33,111]. Figs. 49 and 50 summarize some results of the BHN signal analysis for different disorder strengths and demagnetizing factors. Specifically, in Fig. 49, the bottom panel shows the BHN signal recorded on the ascending branch of the saturation loop and one of its subloops for a significant demagnetization factor  $J_D = 1$  and the disorder  $R = 2.0$  below the critical disorder  $R < R_c(L)$  for the actual lattice size [89]. The structure of the signal, see close-up in the top right panel, shows alternating large and small peaks, corresponding to the step-like magnetization changes (reminiscent of the presence of antiferromagnetic layers [72]) in the weak disorder range, compatible with large domains. Such steps disappear with the increasing disorder above  $R \geq R_c(L)$ . The time necessary for the complete reversal is extended, and the signal exhibits smaller peaks in agreement with decreasing avalanche sizes in the strong-disorder regime. The power spectra of BHN signals for the varied disorders are shown in the top left panel, where we find that the power-law exponent  $\gamma$  varies between 1.55 for weak disorder and 1.95 at the highest disorder strength considered; the exponent is estimated according to Eq. (59) in the high-frequency range, which also varies with the disorder, as the figure shows. We also notice that the signal recorded on a subloop for the same set of parameters shares these qualitative properties of the signal on the saturation loop, apart from being shorter.

The fluctuation function  $F_q(n)$  vs.  $n$  is shown in Fig. 50 for  $q \in [-4.5, 4.5]$ , corresponding to the saturation-loop signal at the effective critical disorder  $R = 2.4$  and high demagnetizing factor  $J_D = 1$ . In the inset to Fig. 50, we show the singularity spectrum  $\Psi(\alpha)$  for varied demagnetizing factor  $J_D$ . As this figure shows, increasing  $J_D$  from zero to one changes the spectrum's shape and systematically shifts the maximum towards the smaller values of  $\alpha$ . Differences between these spectra are significant in the region with small values of  $\alpha$ , which are related to the large fluctuations. They are compatible with the changed Hurst exponent from  $H_2 > 1$  in the absence of demagnetization effects to  $H_2 < 1$  for  $J_D = 1$ , suggesting changed stochasticity of the process from the original fractional Brownian motion to fractional Gaussian noise when the demagnetizing effects are significant. In the latter case, the spectrum is asymmetrical, with an extended right branch (large  $\alpha$  values) describing small magnetization fluctuations.

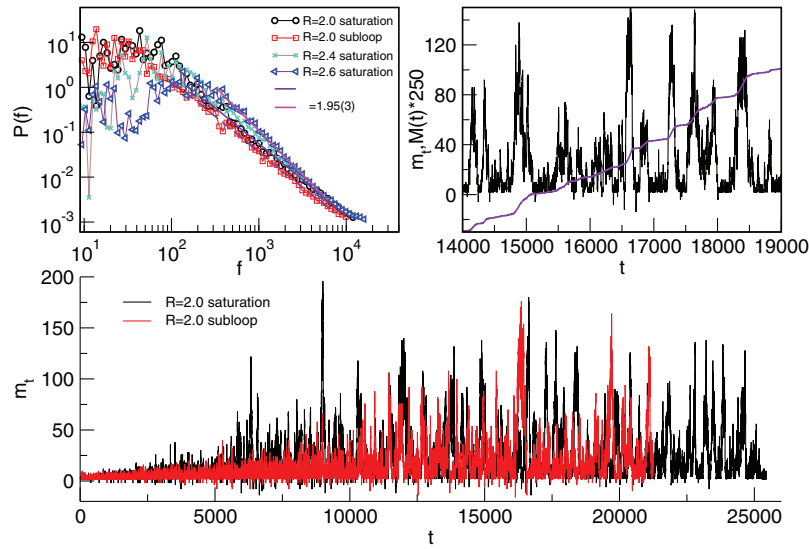


**Figure 49:** The bottom panel shows the magnetization fluctuations  $m_i$  vs. time  $t$  along an ascending branch of the saturation loop (black) and subloop (red line) for a high demagnetizing factor  $J_D = 1$ ; low temperature  $T_r = 0.5$  and the disorder  $R = 2.0$  below the critical  $R_c(L)$  are fixed. A close-up of the signal is shown as a black line in the top right panel, and the total magnetization  $M(t)$  (pink line) appropriately multiplied to fit the same scale, showing characteristic steps and plateaus corresponding to alternating large and small avalanches. Corresponding power spectrum  $P(f)$  vs. the index  $f$  of these signals are shown in the top left panel with saturation loop signals for several values of disorder  $R$ , as indicated in the legend

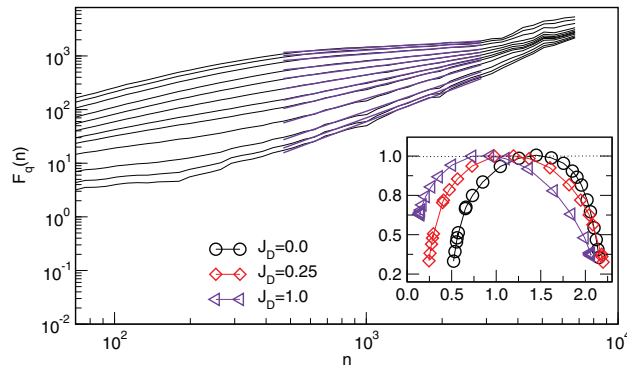


**Figure 50:** The fluctuation function  $F_q(n)$  vs. the time interval length  $n$  for  $q \in [-4.5, 4.5]$  for the magnetization fluctuations along the ascending branch of the hysteresis loop simulated at low temperatures for the effective critical disorder  $R = 2.4$  and significant demagnetizing factor  $J_D = 1.0$ . The straight colored lines indicate the fitted scaling regions; the corresponding singularity spectrum is shown by triangle symbols in the inset together with the spectra for two lower values of  $J_D$ , as indicated in the legend

Considering a more realistic scenario, as explained above in [Section 6](#) with the finite driving rates and thermal fluctuations, the structure of BHN was also analyzed in [164]. At very low relative temperatures and decisive demagnetizing factor  $J_D = 1$ , an asymmetric singularity spectrum was

found, similar to the one in Fig. 50. However, the corresponding window of time intervals where the scaling of the fluctuation function is apparent is different, and it is systematically shifting towards larger time intervals with increasing relative temperatures. However, the fractality is absent at intermediate and small time scales.

### 7.2.2 Multifractal BHN Spectra Vary with the System's Spatial Dimension

Without demagnetizing fields,  $J_D = 0$  in ferromagnetic RFIM considered in this subsection, the critical disorder point firmly controls the hysteresis loop behaviour, as discussed in Section 1. In this case, the BHN's temporal correlations differ along different segments of the hysteresis loop; see for example Reference [111]. Consequently, they alter the multifractal properties of the magnetization fluctuations in distinct segments of the loop, as we discuss below.

Behavior in the central part of the loop is often monitored as closely related to the hysteresis-loop critical point [28,108]. The following example demonstrates the change of the hysteresis-loop critical behavior with the system's dimensionality and its crucial impact on multifractal spectra. In samples with varied thickness, see a detailed study in [111], the critical disorder line  $R_c(\ell, L)$  varies with the sample thickness  $\ell$ , interpolating between the 3D and 2D RFIM critical points; see Section 4.4 above. Consequently, it impacts the stochasticity of the magnetization fluctuation and causes its multifractal features to change with the thickness. Measurements in an experimental realization of samples with varied thicknesses [22] support these general conclusions.

Considering the fluctuations  $F_q(n)$  vs.  $n$  in the central part of the hysteresis loop, in Fig. 51, we show the differences for two samples of finite thickness,  $\ell = 64$  and  $\ell = 128$  and the same base dimension  $L = 512$ . The inset shows the corresponding multifractal spectra  $H_q$  vs.  $q$ ; it also shows the spectrum for a thicker sample with  $\ell = 256$  and the spectra corresponding to the limiting 2D and 3D samples. As this figure suggests, the multifractal spectra in samples above a certain thickness virtually coincide with the one of the 3D samples. Meanwhile, for smaller but finite thicknesses, the multifractal features of small fluctuations (i.e., for the negative  $q$  values) closely follow the line of the 2D sample. In contrast, the large fluctuations (captured by the positive  $q$  values) coincide with the ones of the 3D sample. As stated above, the beginning of the hysteresis loop and its shoulder are compatible with different temporal fluctuations of BHN and possibly different multifractality.

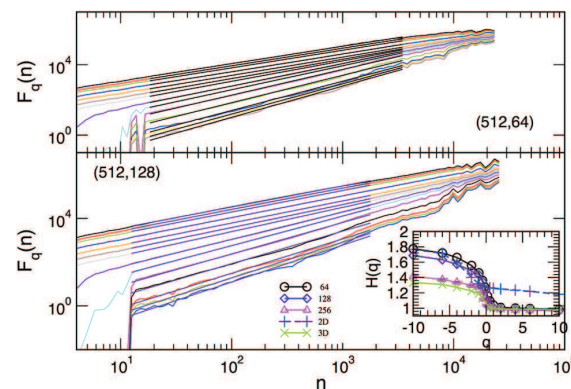


**Figure 51:** The fluctuation function  $F_q(n)$  vs. time interval  $n$  of the magnetization fluctuations in the central part of the hysteresis loop simulated in two samples of the base length  $L = 512$  and different thicknesses  $\ell = 64$  and  $\ell = 128$ . Inset shows the multifractal spectra  $H_q$  vs.  $q$  for different thicknesses indicated in the legend and for 2D and 3D limits; part of the Fig. 7 from [111]

### 7.2.3 Other Factors That Influence the Structure of BHN at Low Temperatures

Besides the system's dimensionality, which determines the universality class of critical behavior, and the strength of disorder (relative to the critical disorder point), which translates to the typical size of domains or the strength of the domain-walls pinning, the structure of BHN in disordered ferromagnets without demagnetizing fields exhibits characteristic variations depending on the considered segment of the hysteresis loop, driving rates and the potential presence of nonmagnetic defects. For demonstration, Fig. 52 shows some representative data, replotted from [33]. In the right panel, plots of the generalized Hurst exponents  $H_q$  vs.  $q$  for different segments of the hysteresis loop and the whole branch are displayed. As this figure shows, the initial 10% of the BHN signal is characterized by the generalized Hurst exponents  $H_q < 1$  for all  $q$  values, and  $H_2 \sim 0.5$ , indicating the class of fractional Gaussian noise. Meanwhile, for the central part of the hysteresis loop  $H_2 > 1$ , suggesting the fractional Brownian motion associated with the affected domain walls. Notably, when the BHN signal integrated over the entire hysteresis branch (or its sizable part) is considered, the parts of the spectrum for small ( $q < 0$ ) and large ( $q > 0$ ) fluctuations have distinct functional forms, leading to a discontinuity at  $q = 0$ .

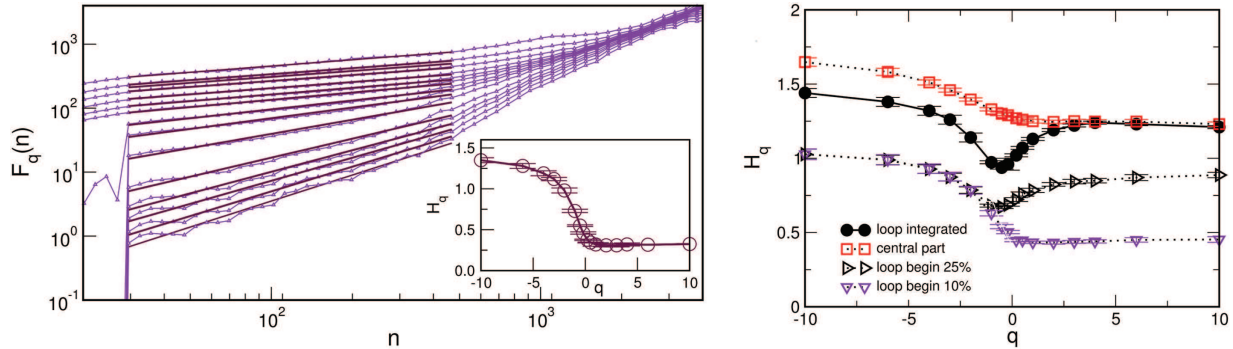


**Figure 52:** The left panel shows the fluctuation function  $F_q(n)$  vs. time interval  $n$  of the magnetization fluctuations in RFIM at critical random-field disorder and the 30% fraction of nonmagnetic sites. Inset shows the corresponding generalized Hurst exponent  $H_q$  vs. the amplification parameter  $q$  determined in the scaling area of  $F_q(n)$ , indicated by thick lines. The right panel shows the spectra of the generalized Hurst exponents  $H_q$  vs.  $q$  of the BHN in different segments of the hysteresis loop and the loop integrated along the ascending branch, as indicated in the legend. Data replotted from [33] are for RFIM without nonmagnetic defects at the critical random-field disorder and quasistatic driving with a small field increment

As stated above, the structure of the BHN is also sensitive to the driving rate. In particular, the increased driving rate leading to the spatio-temporal merging of the avalanches also results in the increased size of magnetization fluctuations; consequently, the whole reversal process is accomplished faster, resulting in a shorter time series overall. It manifests in the altered avalanche statistics, as discussed in Section 5. Increasing the driving rates also changes the multifractal properties of BHN, as shown in [33]. Specifically, the part of the spectrum corresponding to  $q < 0$  is strongly affected by the increased driving rate, indicating that the present amount of slight fluctuations of the magnetization needs to be amplified with more prominent exponents  $H_q$  to become self-similar with the rest of the signal; see Fig. 10 in [33]. Conversely, the large fluctuations weakly change with the driving rates. However, the large fluctuations can be considerably affected, resulting in the exponents  $H_q < 0.5$  for  $q > 0$ , by adding nonmagnetic defects [33]. These defects further reduce the size of domains, thus

hindering the avalanche propagation compared to the ones defined by the random fields [26]. The fluctuation function  $F_q(n)$  vs.  $n$  in the presence of 30% fraction of nonmagnetic defects is shown in the left panel of Fig. 52. The Hurst exponents spectrum  $H_q$  plotted against  $q$  shown in the inset is determined in the intermediate range of time intervals, indicated by the straight lines on the main plot.

The hysteretic response to the slow field ramping, which results in the collective magnetization fluctuations, also manifests in the structure of avalanche sequences. As stated above, the difference between the size of two consecutive avalanches is not a normal Gaussian; it exhibits a structure which is described by Tsallis distribution in Eq. (60). In Fig. 53, we show two examples of avalanche sequences, demonstrating that the non-extensivity parameter  $q_e$  of this distribution also varies with the driving rate and may serve as another measure of its impact on the magnetization reversal process. In a more general context, this feature of the Barkhausen avalanches in disordered ferromagnets indicates a complex dynamical behaviour of driven domain walls in these systems, which belongs to a class of non-extensive out-of-equilibrium dynamics occurring in many complex systems driven by the external forces; see recent review in [207] and references there.

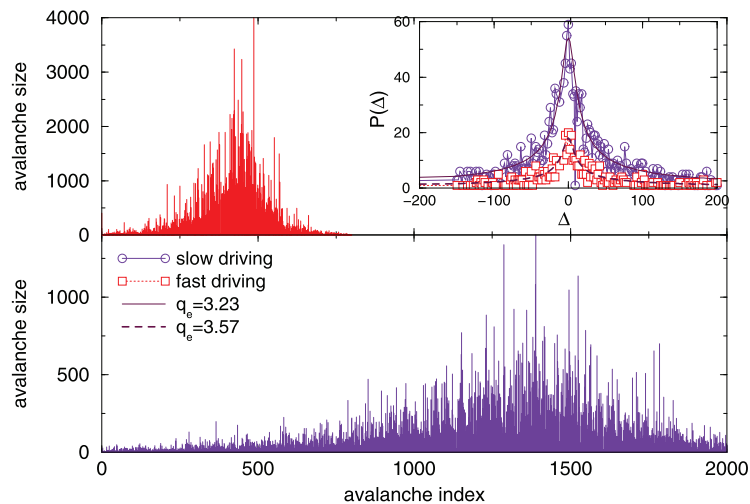


**Figure 53:** The bottom and top-left panels show the avalanche sequences for slow ( $\Omega = 0.002$ ) and fast driving ( $\Omega = 0.008$ ), respectively, and fixed strong random-field disorder  $R = 4.0$ . The top-right inset shows their first-return distributions; fitting lines according to Eq. (60) correspond to the non-extensivity parameters  $q_e$  shown in the legend. Data replotted from Fig. 2 of Reference [33]

## 8 Response Signal Analysis with the Aid of Threshold

Being superposed on the magnetic response, thermal fluctuations prevent the decomposition of the response signal of the thermal RFIM systems into events that can be considered as essentially caused by magnetic interactions and only randomized by thermal noise. This is also the case for real (magnetic) systems where, besides thermal, some amount of noise of other origins appears (e.g., digital noise and/or noise caused by electromagnetic interference). In such cases, the decomposition of the response signal into (subsequently analyzed) events is accomplished with the use of threshold  $V_{th} > 0$ , see in Section 2.

The threshold value is not given in advance but instead has to be suitably chosen (e.g., estimated from the parts of the response signal in which the magnetic response could be rightly considered to be

absent). Fortunately, in all situations with reasonably small/moderate overall noise, there is some range of not-too-small and too-big values of threshold such that for any  $V_{\text{th}}$  in this range the subsequently collected statistics are (almost) not affected by this choice.

In this section, we show how the choice of threshold influences the statistics of the adiabatically driven ZT NEQ RFIM of homogeneous ferromagnetic spin systems ( $R_i = R$ ,  $J_{ij} = J = 1$ , and  $H_i = H$ ) without demagnetizing field which are situated at (3D) equilateral cubic lattices of size  $L$  with Gaussian distribution of the quenched random magnetic field uncorrelated at different lattice sites. In the analysis [140] of the noiseless case, it was shown how the choice of threshold influences the decomposition of the response signal into events (i.e., subavalanches because in that case, due to adiabatic driving, the events are actually individual avalanches), leading to introduction of several types of waiting time graphically illustrated in Fig. 54 replotted from Fig. 1 of Reference [140]. Panel (b) of this figure demonstrates that large values of threshold are needed for a significant change in duration and size distributions. Data from panel (c) show that the power-law correlation  $\langle S \rangle_T \propto T^{\gamma_{S/T}}$  between the average size of subavalanches  $\langle S \rangle_T$  of duration  $T$  is maintained with remark that the (effective) value of the power-law exponent  $\gamma_{S/T}$ , estimated as the slope of log-log plot of the  $\langle S \rangle_T$  vs.  $T$  data, varies with the threshold value  $V_{\text{th}}$  as shown in panel (d).

The values of  $\gamma_{S/T}$  fall from the initial value  $\gamma_{S/T} \approx 1.78$  at  $V_{\text{th}} = 0$ , describing also the scaling of the power spectra, to a pretty much stable plateau value  $\gamma_{\text{th}} \approx 1.5$ , attained by this exponent in a rather broad range of threshold values. This finding may be of significant importance for the analyses of experimental data where the use of thresholds is unavoidable and the exponent values are determined by fitting of the experimental data to some reasonably chosen analytic form because the (more reliable) estimation of the exponents' values through the data collapsing procedure is impossible.

Starting from the conjecture that the temporal shape of avalanches satisfies the scaling conditions that are given by Eqs. (2) and (12) from Reference [140], the RFIM analysis in question revealed that the integrated distributions of avalanche duration,  $D_T^{(\text{int})}(T; V_{\text{th}}, r, 1/L)$ , avalanche size,  $D_S^{(\text{int})}(S; V_{\text{th}}, r, 1/L)$ , and the distributions  $D_{T_w}^{(\text{int})}(T_w; V_{\text{th}}, r, 1/L)$  of each type of waiting time  $T_w$ , follow the data-collapsing predictions

$$V_{\text{th}}^{\alpha_{\text{int}}/(\gamma_{S/T}-1)} D_T^{(\text{int})}(T; V_{\text{th}}, r, 1/L) = D_T \left( T/V_{\text{th}}^{1/(\gamma_{S/T}-1)}; V_{\text{th}}^{\sigma/(1-\gamma_{T/S})} r, V_{\text{th}}^{\sigma v/(1-\gamma_{T/S})} /L \right), \quad (61)$$

$$V_{\text{th}}^{\tau_{\text{int}}/(1-\gamma_{T/S})} D_S^{(\text{int})}(S; V_{\text{th}}, r, 1/L) = D_S(S/V_{\text{th}}^{1/(1-\gamma_{T/S})}; V_{\text{th}}^{\sigma/(1-\gamma_{T/S})} r, V_{\text{th}}^{\sigma v/(1-\gamma_{T/S})} /L), \quad (62)$$

$$V_{\text{th}}^{\alpha_{\text{int}}/(\gamma_{S/T}-1)} D_{T_w}^{(\text{int})}(T_w; V_{\text{th}}, r, 1/L) = D_{T_w}(T_w/V_{\text{th}}^{1/(\gamma_{S/T}-1)}; V_{\text{th}}^{\sigma/(1-\gamma_{T/S})} r, V_{\text{th}}^{\sigma v/(1-\gamma_{T/S})} /L), \quad (63)$$

provided that the conformity conditions

$$V_{\text{th}}^{\sigma/(1-\gamma_{T/S})} r = \text{const}, \quad V_{\text{th}}^{\sigma v/(1-\gamma_{T/S})} /L = \text{const}. \quad (64)$$

are satisfied. The same type of scaling is satisfied also for the windowed type of distributions, see Fig. 55 replotted from Fig. 3 of Reference [140].

The previous results are extended in the analysis [141] of the impact of the (zero-mean) noise added on the response signal manifesting only intrinsic thermal noise; see also [208]. The added noise is much greater than the system's noise so that it only affects the registered signal and not the system dynamics. Such RFIM modification mimics the real systems influenced by the external noise originated from detectors, amplifiers, analog-to-digital (AD) converters, ambient electromagnetic interference (EMI), etc.

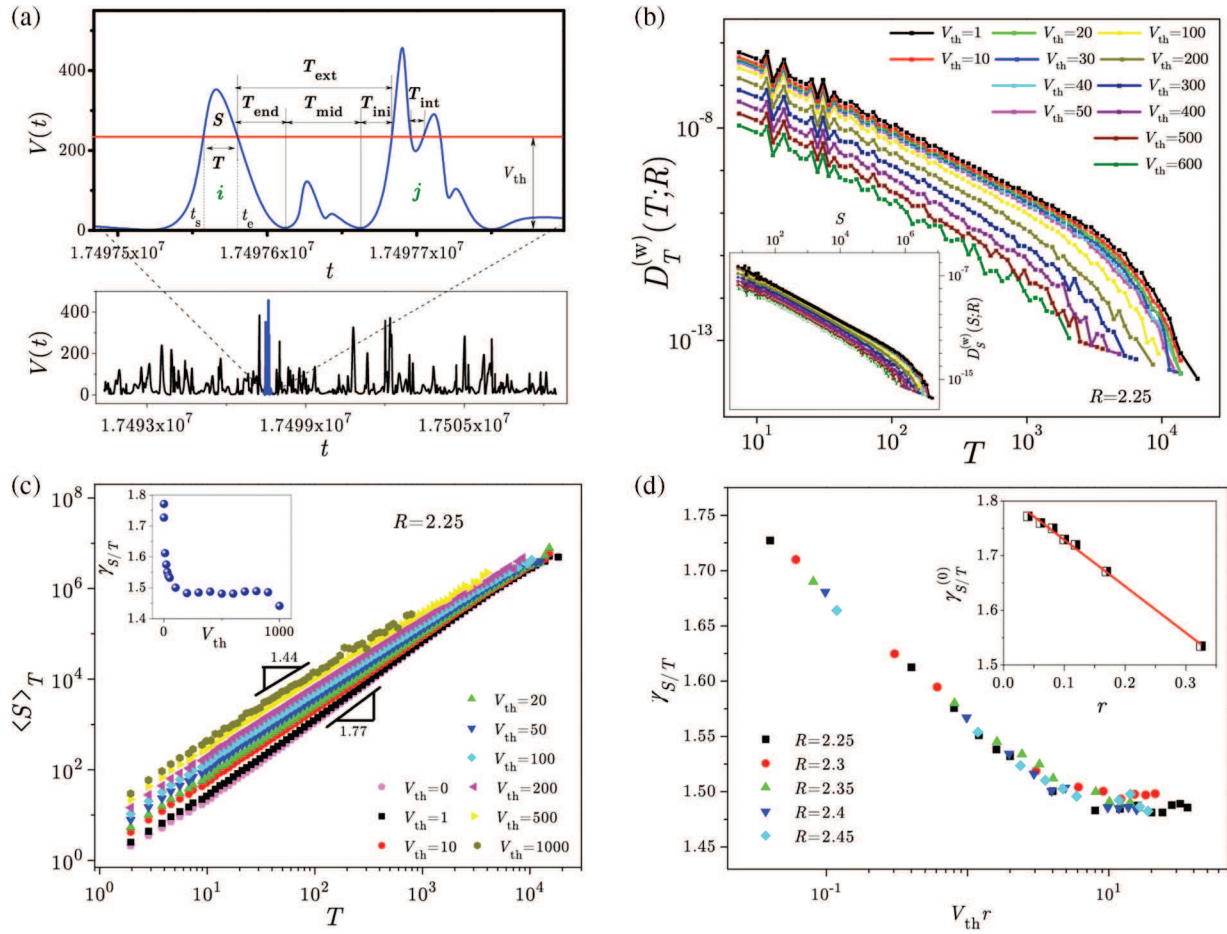


**Figure 54:** (a) Decomposition into events (i.e., subavalanches) of the response signal. For a (blue) part of a train of avalanches (shown in the bottom, and zoomed in the top part of this panel) and the imposed threshold  $V_{th}$  (red line), we illustrate: the determination of size  $S$  and duration  $T$  of a subavalanche (starting at the moment  $t_s$  and ending at  $t_e = t_s + T$ ) taken out of the avalanche  $i$ , the internal waiting time  $T_{w,int}$  between two subavalanches of avalanche  $j$ , and the contributions  $T_{w,end}$ ,  $T_{w,mid}$ , and  $T_{w,ini}$  to the external waiting time  $T_{w,ext}$  between avalanches  $i$  and  $j$ . (b) Windowed distributions  $D_T^{(w)}(T; V_{th}, r, 1/L)$  of duration (main panel), and distributions  $D_S^{(w)}(S; V_{th}, r, 1/L)$  of size (inset) of subavalanches selected by thresholds from a wide range shown in legend. (c)  $\langle S \rangle_T$  shown against  $T$  for the thresholds in legend, where  $\langle S \rangle_T$  is the average size of subavalanches with duration  $T$ ; variation of exponent  $\gamma_{S/T}$  with  $V_{th}$  is shown in the inset. (d)  $\gamma_{S/T}$  vs.  $V_{th}$  data, obtained for various disorders  $R$  (see legend), collapse onto the same curve when presented against  $V_{th}r$ , where the reduced disorder  $r = (R - R_c)/R$  measures a distance to the critical disorder  $R_c$  of the model. Inset shows how  $\gamma_{S/T}^{(0)}$  (i.e., the exponent  $\gamma_{S/T}$  value taken for  $V_{th} = 0$ ) depends on the reduced disorder  $r$ . The data from panels (b)–(d) are obtained in 40 random field configurations for each disorder  $R$  and  $L = 1024$ . This is Fig. 1 from [140]

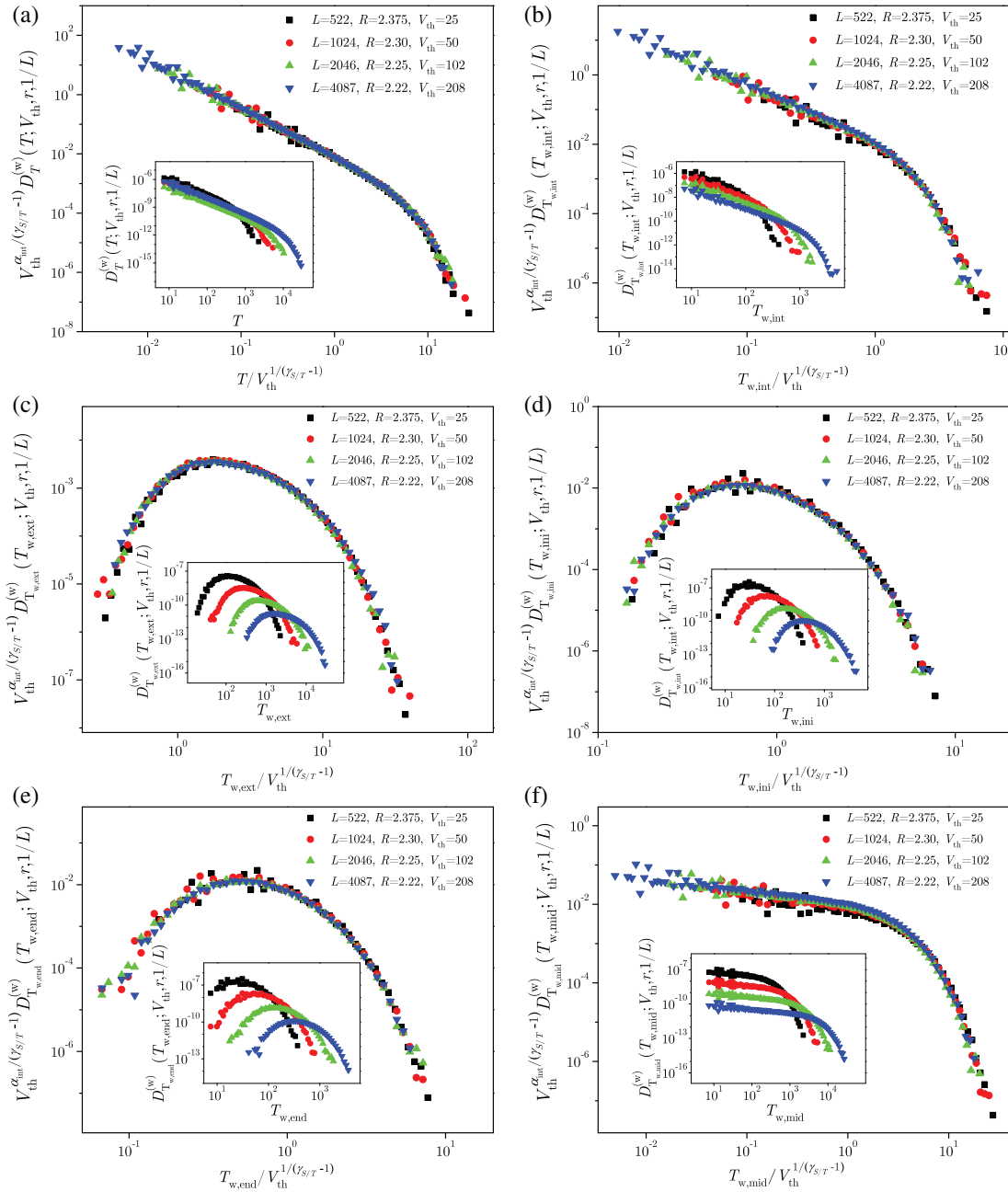


**Figure 55:** Collapsing of windowed distribution of duration and waiting time for the events (i.e., parts of the signal that are above threshold  $V_{th}$ ) extracted in simulations with values of disorder  $R$  and lattice size  $L$  from the legends satisfying collapsing requirements Eq. (64). All collapses are achieved after the distributions are multiplied by  $V_{th}^{\alpha_{int}/(\gamma_S T^{-1})}$  and presented against their arguments divided by  $V_{th}^{1/(\gamma_S T^{-1})}$ , see Eq. (61) and Eq. (63) [140]. Panel (a) shows the scaling collapse of distributions of durations  $T$ , and panels (b)–(f) collapsing of distributions for the following types of waiting times:  $T_{w,int}$ ,  $T_{w,ext}$ ,  $T_{w,ini}$ ,  $T_{w,end}$ , and  $T_{w,mid}$ , respectively. Original distributions are shown in the insets. This is Fig. 3 from [140]

In Figs. 56 and 57 we illustrate the effect of added noise for the case of uniform white noise (UWN), i.e., the noise with standard deviation  $\sigma$  and probability density  $p(x) = 2/\sqrt{3}\sigma$  for  $-\sqrt{3}\sigma/2 \leq x \leq \sqrt{3}\sigma/2$  and 0 elsewhere, and for the case of Gaussian white noise (GWN),  $p(x) = \exp(-x^2/2\sigma^2)/\sigma\sqrt{2\pi}$  with standard deviation  $\sigma$ . Left panels of Fig. 56 show how the distributions  $\langle S \rangle_T$  (of the average size of the avalanches having duration  $T$ ) are influenced by the added white (top row) and Gaussian (bottom row) noise having standard deviation  $\sigma$ . Additionally, in the main parts of the right panels of Fig. 56, the flow with threshold  $V_{th}$  of the values of exponent  $\gamma_{S/T}$  (pertaining to the power-law correlation  $\langle S \rangle_T \propto T^{\gamma_{S/T}}$ ) illustrate the influence of the added noise for several values of standard deviation  $\sigma$  quoted in legend, most importantly on the  $\gamma_{S/T}$  plateau values. Analogous influence is shown in the pertaining insets as a function of  $\sigma$  for the thresholds  $V_{th}$  in the insets' legend.

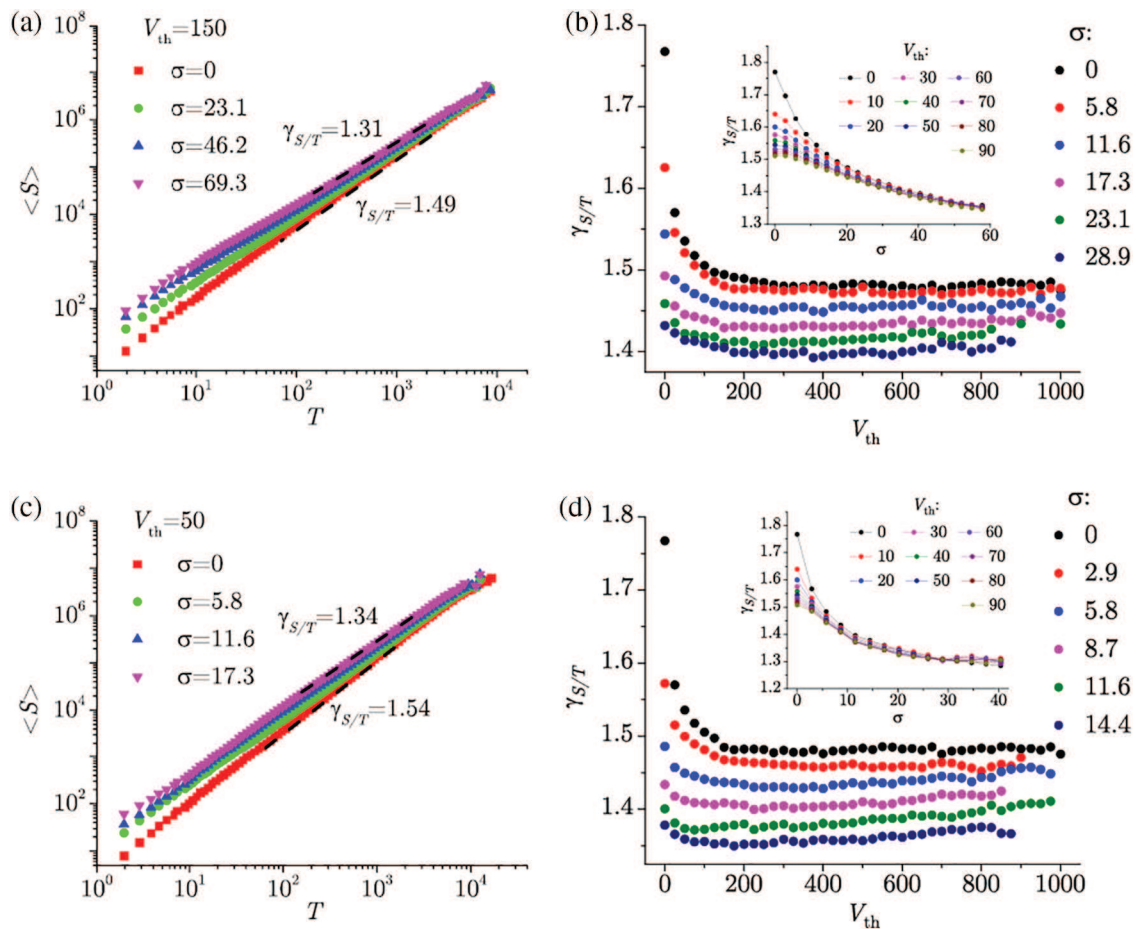


**Figure 56:** In this figure, combined are Figs. 2 and 4 from [141]: Left panels (a) and (c) show the average size  $\langle S \rangle_T$  of avalanches having duration  $T$  for the system of size  $1024 \times 1024 \times 1024$ , disorder  $R = 2.25$ , and the standard deviation  $\sigma$  given in legends. In the top left panel (a) presented is the UWN case for the threshold  $V_{th} = 150$ , while in the bottom left panel (c) shown is the Gaussian noise case for the  $V_{th} = 50$ . Right panels (b) and (d) present the flow of the values of the exponent  $\gamma_{S/T}$  against  $V_{th}$  in the main panel parts, and against standard deviation  $\sigma$  in insets, both in the UWN (top) and GWN (bottom) case and for the values of  $V_{th}$  and  $\sigma$  shown in legends

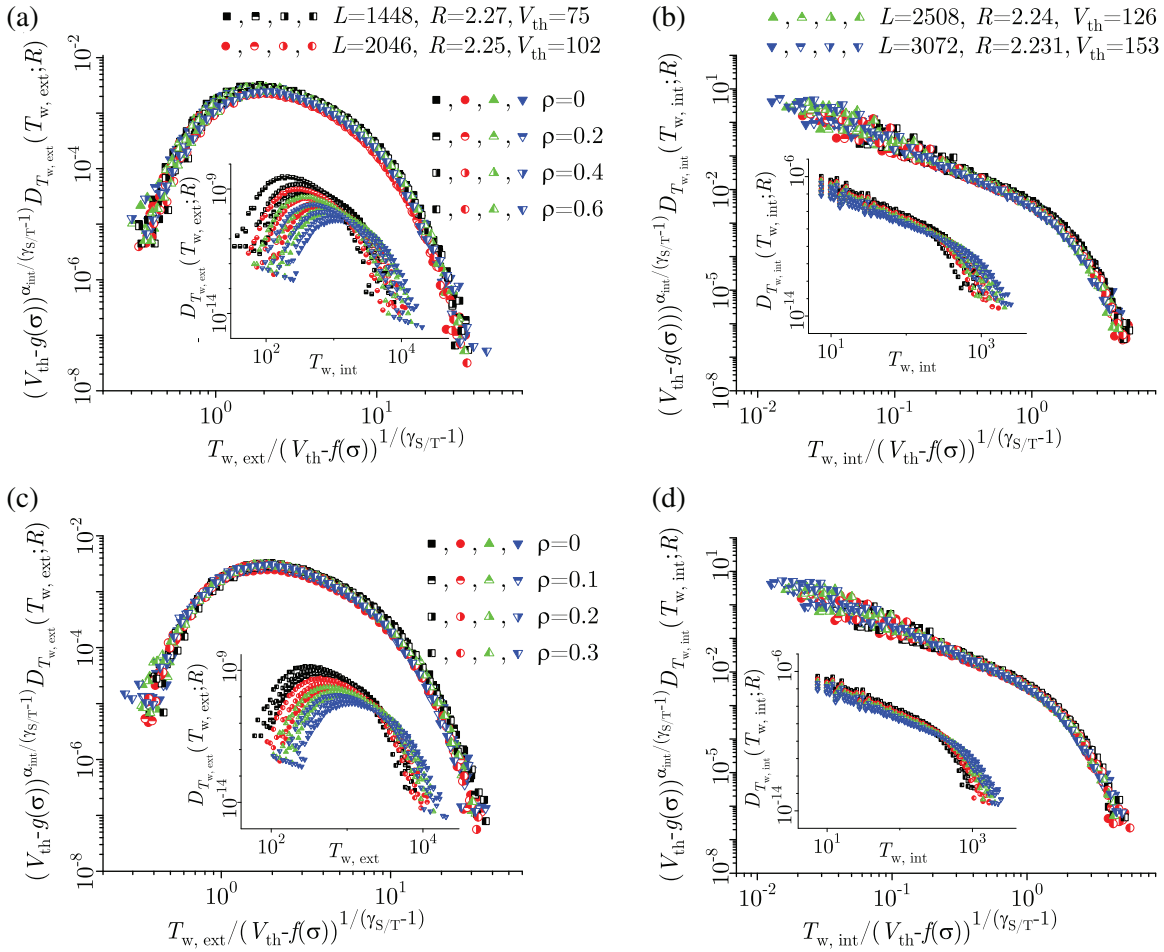


**Figure 57:** This is Fig. 13 from [141]. Graphs in main panels show the collapsing of the distributions of external waiting times (left column, (a) and (c) panels) and internal waiting times (right column, (b) and (d) panels) in the UWN case (top row, (a) and (b) panels) and GWN case (bottom row, (c) and (d) panels). These graphs correspond to the following four simulation parameters combinations  $\{L = 1448, R = 2.27, V_{th} = 75\}$ ,  $\{L = 2046, R = 2.25, V_{th} = 102\}$ ,  $\{L = 2508, R = 2.24, V_{th} = 126\}$ , and  $\{L = 3072, R = 2.231, V_{th} = 153\}$ , satisfying the compatibility conditions (cf. Eq. (6) in [141])  $V_{th}^{\sigma^2 \nu z / (\sigma^2 \nu z - 1)} r = \text{const}$ , and  $V_{th}^{\sigma^2 \nu z / (\sigma^2 \nu z - 1)} / L = \text{const}$ , where  $\sigma$  (aliased here by  $\sigma'$ ),  $\nu$ , and  $z$  are the standard 3D ZT NEQ RFIM exponents [28]; non-collapsed data is shown in insets. For the functions  $f(\sigma)$  and  $g(\sigma)$ , shifting  $V_{th}$  in the collapsing expressions, we route the reader to Fig. 12 from [141] presenting their values

The impact of added noise is also noticeable in the power spectrum, average avalanche shapes, and all distributions of avalanche parameters. Nevertheless, the impact is most pronounced in the distributions of various types of waiting time (e.g., external and internal), as is evidenced in Fig. 57.

## 9 Summary, Limitations and Future Work

Supported by the presented works, one can identify two significant computational approaches. Specifically, we distinguish the theoretical limit of adiabatically driven systems with zero-temperature critical dynamics on one side, and the critical dynamics under the influence of a myriad of interrelated factors, i.e., the temperature, demagnetizing fields, and finite driving rates, resembling experimental situations, on the other.

The simplicity of employing Ising spins as binary variables, enables efficient simulations of the adiabatically driven systems, tailored in the sorted-list and the bit-per-spin algorithms. By these (and related) algorithms, the efficiency of the originally proposed codes for numerical simulations has been greatly improved, especially regarding the execution time and memory resources, which in large-scale system studies pose a significant computational load and an actual challenge. The implemented code enhancements made it possible to perform large-scale simulations of systems having up to more than  $10^{10}$  spins and raised the standard by allowing the extensive statistical sampling of up to  $10^5$  different realizations of random magnetic field, considerably improving the accuracy of obtained data and subsequently the conclusions drawn from it. Additionally, the code improvements expanded the scope of underlying factors influencing the behavior of the systems that were considered, allowing for different driving protocols with different time profiles of driving field, the inclusion of demagnetizing and thermal effects, the analysis of systems with different geometry and lattice structures, down to the characterization at the level of individual crystal grains.

Streamlining the analysis, the systems being studied are regarded as ferromagnetic insulators, with magnetic walls indirectly defined as boundaries of cluster of spins with same orientation. The extended version of model allows for taking into consideration variable exchange couplings and anisotropy, and is open for inclusion of other types of magnetic interactions and external electromagnetic interference (EMI). It also enables the simulations of single and multilayered ferro/antiferromagnetic systems, accounting for lattice imperfections caused by vacancies and interstices, as well as simulations of amorphous systems. One of the limitations of the existing version of the model is that it does not consider the magneto-mechanical coupling, which leaves room for future development.

The relevance of conducted simulations is also verified quantitatively in comparison with the experimental data obtained in measurements of BHN. Used in numerous applications (e.g., as memory materials, thin films and nanowires), the disordered ferromagnetic materials are currently the subject of intensive ongoing research. In a complementary reciprocity, reliable and comprehensive experimental data is necessary for the development of adequate modeling tools, while simulation results can also serve as cornerstones and guidelines for experiments, calling for mutual advancements both in experimental techniques and optimizations of the employed algorithms. Beyond producing simulation results with practical applications, the future advancement might go along the lines of creating a more sophisticated and universal design technique, possibly applicable to other complex systems that exhibit an avalanche-like evolution, particularly those that like earthquakes could cause severe catastrophic consequences.

This article reviewed the developments and continuous progress in numerical modeling of the NEQ RFIM complementing the renormalization group theoretical investigations of out-of-equilibrium critical dynamics [37]. The preceding outlines highlight some of the potential difficulties and prospective avenues in this area of study, aiming to inspire motivation for future research and opportunities for further development. The corresponding main messages and some open questions are summarized below.

- $\Theta = 0$  *critical dynamics with the adiabatic driving* is a theoretically sound limit where one can identify the individual avalanches and their propagation in this type of driving. In analogy to self-organized criticality, this limiting case obeys the time-scale separation (between the driving and avalanche propagation), which enables a clear definition of the systems' activity avalanches at the mesoscopic scale and their statistics. It further allows the use of finite-size scaling analysis, which determines the value of the critical disorder and the critical field, related sets of scaling exponents, and the scaling functions. Interestingly, for three-dimensional systems, the associated critical exponents at the disorder-induced critical point are numerically close to the ones of the equilibrium phase transition temperature-driven; however, the scrutinized numerical analysis revealed the asymmetry of the scaling function, compatible with the non-equilibrium critical dynamics, in agreement with the renormalization group theory. Furthermore, the universality classes of the observed critical behavior were determined depending on the system's spatial dimensionality, shape, and thickness. These systems' properties also manifest in the multifractal spectra of the associated simulated BHN; thus, the multifractal analysis can be used as an appropriate quantitative measure. The presented research provides valuable insights into the universality of the out-of-equilibrium dynamics. It can be applied in various scientific investigations, such as critical dynamics in open quantum systems, particularly when the driving conditions satisfy the time-scale separation.
- $\Theta \gtrsim 0$  *dynamics with finite driving rates and demagnetizing fields* requires additional parameters but also adapting the simulation and driving rules. Moreover, the stochasticity of the reversal process increases, which requires extra care to separate the random noise and identify spin avalanches, similar to the procedures carried out in the analysis of the experimental BHN signals. At low temperatures, relative to the critical temperature  $\Theta/T_c$  and finite driving rate  $\Omega$ , guided by the zero-temperature dynamics theory, one can successfully identify the key features of the collective dynamics and determine their dependence on these physical parameters. The advantage is that the results can be compared to experiments, for example, in nanocrystalline samples and on bearing steel of different hardness levels. Such comparisons of the corresponding model simulations with experimental Barkhausen noise data emphasize the relevance of numerical simulations for broadening the view of underlying stochastic processes and the critical role of disorder-induced and thermal fluctuations. In particular, in [Section 7.1](#), remarkable agreements were demonstrated when systematically comparing the features extracted from the experiment on nanocrystalline samples and data simulated by RFIM on a large lattice and appropriate range of disorder and driving rates, confirming the non-equilibrium disorder-induced criticality of these samples. A similar comparison of experimental Barkhausen noise characteristics obtained on bearing steel of different hardness was made using classical Monte Carlo simulations of the Ising model, which are known to perform well near the thermal critical point.

Adding demagnetizing fields in the Hamiltonian induces a specific type of long-range interactions that counteract the driving field; they change the shape of the hysteresis loop and the properties of the BHN signal. These effects increase with the strength of the demagnetizing factor  $J_D$ , manifested in the multifractal features, the avalanche scaling and a potential shift in the critical disorder. This is in contrast to the RFIM with the short-range ferromagnetic interactions, studied above in [Sections 4, 5](#) and the related references, where the existence of the disorder-induced critical point  $R_c(L)$  for  $L \rightarrow \infty$  has been proved by the appropriate finite-size scaling analysis, in agreement with the renormalization-group theory. In the presence of demagnetizing fields, however, the system's dynamics at a global scale have an impact on the

driving force. Considering the thermodynamic limit, an open question is whether the nature of the disorder-induced critical behavior of NEQ RFIM at finite demagnetizing factors is altered and what the actual role of random field is in this case. Theoretically, the critical dynamics at the disorder-induced critical point might change to a self-organized critical behavior, which is not associated with any phase transition in analogy to the driving-induced crossover. Another example to mention in this context is the hysteresis behavior in the infinite-range spin glasses.

Among other open questions that remain for future work, we mention the demagnetizing effects in experimentally accessible antiferromagnetic-ferromagnetic bilayers, and the role of random fields in the hysteresis loop behaviour of antiferromagnetic materials and spin glasses (where the random field variance  $R$  appears as a field conjugate to a spin-glass order parameter). Furthermore, understanding the impact of more complex geometries, e.g., those that appear at a nanoscale suitably represented by nanonetworks, on spin ordering under the driving fields is a question of high interest due to the increasing use of the magnetic properties of nanoassemblies in modern technology applications. Theoretically, complex architectures of these assemblies support higher-order interactions; in conjunction with antiferromagnetic interactions among Ising spins, the topology of these assemblies appears as a decisive factor that shapes the hysteresis loop, thus altering the role of disorder as it is known in crystalline structures.

## 10 Conclusions

This review focuses on the hysteresis-loop criticality as a remarkable example of the out-of-equilibrium critical dynamics occurring during the magnetization reversal driven by the external field in disordered ferromagnetic materials. With the use of the nonequilibrium Random Field Ising Model as a paradigmatic model for theoretical investigations of disordered ferromagnets, we provide a comprehensive survey of mathematical modelling approaches to the simulations of spin-reversal processes for a variety of physical parameters and conditions motivated by theoretical requirements as well as the experimentally realizable situations. Concerning this matter, we present advanced computational techniques that are not just theoretical but also practical. By the results of several recent studies, we demonstrated the gain they led to in acquiring new physical insights into studied complex dynamical phenomena manifesting inherent scale invariance, finitesize scaling of the avalanche distributions, and the multifractal nature of the magnetization fluctuations in the Barkhausen nose time series near the disorder-induced critical point subject to additional physical parameters. The presented computational techniques utilizing the inherent scale-invariance of the hysteresis-loop criticality provide a deeper insight into magnetization reversal processes in disordered ferromagnetic systems, complementing the theoretical and experimental research. These powerful numerical methods can be adapted to study out-of-equilibrium dynamics in many-body quantum systems and other complex systems exhibiting nonequilibrium critical dynamics across the scales.

**Acknowledgement:** The authors are grateful to the journal editors for the invitation to write this review paper. The authors express their gratitude for the computing facilities provided by the Faculty of Physics in Belgrade, the Faculty of Science in Kragujevac, and the Scientific Computing Laboratory of the Institute of Physics in Belgrade. Having access to these high-performance computer clusters was essential to successfully carry out extensive numerical work in preparing the (here reviewed) authors' papers which greatly influenced the results and conclusions this study overviews.

**Funding Statement:** Djordje Spasojević and Svetislav Mijatović acknowledge the support from the Ministry of Science, Technological Development and Innovation of the Republic of Serbia (Agreement

No. 451-03-65/2024-03/200162), S.J. *ibid.* (Agreement No. 451-03-65/2024-03/200122), and Bosiljka Tadić from the Slovenian Research Agency (program P1-0044).

**Author Contributions:** The authors confirm contribution to the paper as follows. Regarding the review article: conception and design: Djordje Spasojević, Sanja Janičević, Svetislav Mijatović and Bosiljka Tadić; draft manuscript preparation: Djordje Spasojević, Sanja Janičević and Bosiljka Tadić. Regarding the author's original papers: software preparation: Djordje Spasojević and Bosiljka Tadić; data collection: Sanja Janičević and Svetislav Mijatović; analysis and interpretation of results: Djordje Spasojević, Sanja Janičević, Svetislav Mijatović and Bosiljka Tadić. All authors reviewed the results and approved the final version of the manuscript.

**Availability of Data and Materials:** All of the data from the authors' published studies presented in this review article are available upon reasonable request.

**Ethics Approval:** Not applicable.

**Conflicts of Interest:** The authors declare no conflicts of interest to report regarding the present study.

## References

1. Honkanen M, Lukinmaa H, Kaappa S, Santa-aho S, Kajan J, Savolainen S, et al. Magnetic domain wall dynamics studied by *in-situ* Lorentz microscopy with aid of custom-made Hall effect sensor holder. *Ultramicroscopy*. 2024;262:113979. doi:10.1016/j.ultramic.2024.113979.
2. Santa-aho S, Honkanen M, Kaappa S, Azzari R, Saren A, Ullakko K, et al. Multi-instrumental approach to domain walls and their movement in ferromagnetic steels-origin of barkhausen noise studied by microscopy techniques. *Mater Des*. 2023;234(1):112308. doi:10.1016/j.matdes.2023.112308.
3. Honkanen M, Santa-aho S, Laurson L, Eslahi N, Foi A, Vippola M. Mimicking Barkhausen noise measurement by *in-situ* transmission electron microscopy-effect of microstructural steel features on Barkhausen noise. *Acta Mater*. 2021;221:117378. doi:10.1016/j.actamat.2021.117378.
4. Papavasileiou AV, Menelaou M, Sarkar KJ, Sofer Z, Polavarapu L, Mourdikoudis S. Ferromagnetic elements in two-dimensional materials: 2D magnets and beyond. *Adv Funct Mater*. 2023;34(2):2309046. doi:10.1002/adfm.202309046.
5. Liang X, Dong C, Chen H, Wang J, Wei Y, Zaeimbashi M, et al. A review of thin-film magnetoelastic materials for magnetoelectric applications. *Sensors*. 2020;20(5):1532. doi:10.3390/s20051532.
6. Rasaili P, Sharma NK, Bhattarai A. Comparison of ferromagnetic materials: past work, recent trends, and applications. *Condens Matter*. 2022;7(1):12. doi:10.3390/condmat7010012.
7. Yao Y, Zhan X, Sendeku MG, Yu P, Dajan FT, Zhu C, et al. Recent progress on emergent two-dimensional magnets and heterostructures. *Nanotechnology*. 2021;32:472001.
8. Bertotti G. *Hysteresis in magnetism*. Boston: Academic Press; 1998.
9. Bertotti G, Mayergoyz ID. *The science of hysteresis, vol. II: physical modeling, micromagnetics, and magnetization dynamics*. Amsterdam: Academic Press; 2006.
10. Li P, Zhang J, Gao Y, Xia X, Weng GJ. Effect of magnetic field on macroscopic hysteresis and microscopic magnetic domains for different ferromagnetic materials. *J Mater Res Technol*. 2024;31:458–71.
11. Balakrishna AR. Rethinking hysteresis in magnetic materials. *MRS Commun*. 2024;14:835–45. doi:10.1557/s43579-024-00624-6.
12. Kovacs A, Exl L, Kornell A, Fischbacher J, Hovorka M, Gusenbauer M, et al. Image-based prediction and optimization of hysteresis properties of nanocrystalline permanent magnets using deep learning. *J Magn Mater*. 2024;596:171937. doi:10.1016/j.jmmm.2024.171937.

13. Schwarz A, Liebmann M, Kaiser U, Wiesendanger R, Noh TW, Kim DW. Visualization of the Barkhausen effect by magnetic force microscopy. *Phys Rev Lett.* 2004;92:077206.
14. Alessandro B, Beatrice C, Bertotti G, Montorsi A. Domain wall dynamics and Barkhausen effect in metallic ferromagnetic materials. *J Appl Phys.* 1990;68:2901.
15. Bertotti G, Durin G, Magni A. Scaling aspects of domain wall dynamics and Barkhausen effect in ferromagnetic materials. *J Appl Phys.* 1994;75:5490.
16. Durin G, Magni A, Bertotti G. Measurements of the Barkhausen effect in FeCoB amorphous alloys. *J Magnet Magnet Mater.* 1996;160:299–301.
17. Spasojević D, Bukvić S, Milošević S, Stanley HE. Barkhausen noise: elementary signals, power laws, and scaling relations. *Phys Rev E.* 1996;54:2531.
18. Lee WY, Choi BC, Xu YB, Bland JAC. Magnetization reversal dynamics in epitaxial Fe/GaAs(001) thin films. *Phys Rev B.* 1999;60(14):10216. doi:10.1103/PhysRevB.60.10216.
19. Moore TA, Rothman J, Xu YB, Bland JAC. Thickness-dependent dynamic hysteresis scaling behavior in epitaxial Fe/GaAs(001) and Fe/InAs(001) ultrathin films. *J Appl Phys.* 2001;89(11):7018. doi:10.1063/1.1357840.
20. Ryu KS, Akinaga H, Shin SC. Tunable scaling behaviour observed in Barkhausen criticality of a ferromagnetic film. *Nature Phys.* 2007;3(8):547–50. doi:10.1038/nphys659.
21. Estévez V, Laurson L. Magnetic domain-wall dynamics in wide permalloy strips. *Phys Rev B.* 2016;93(6):064403. doi:10.1103/PhysRevB.93.064403.
22. Dos Santos Lima GZ, Corso G, Correa MA, Sommer RL, Ivanov PC, Bohn F. Universal temporal characteristics and vanishing of multifractality in Barkhausen avalanches. *Phys Rev E.* 2017;96(2):022159. doi:10.1103/PhysRevE.96.022159.
23. Lee HS, Ryu KS, Jeon KR, Parkin SSP, Shin SC. Breakdown of Barkhausen critical-scaling behavior with increasing domain-wall pinning in ferromagnetic films. *Phys Rev B Condens Matt Mater Phy.* 2011;83(6):060410. doi:10.1103/PhysRevB.83.060410.
24. Krasnytska M, Berche B, Holovatch Y, Kenna R. Ising model with variable spin/agent strengths. *J Phy: Comp.* 2020;1(3):035008. doi:10.1088/2632-072X/abb654.
25. Vives E, Planes A. Avalanches in a fluctuationless first-order phase transition in a random-bond Ising model. *Phys Rev B.* 1994;50(6):3839–48. doi:10.1103/PhysRevB.50.3839.
26. Tadić B. Nonuniversal scaling behavior of Barkhausen noise. *Phys Rev Lett.* 1996;77(18):3843. doi:10.1103/PhysRevLett.77.3843.
27. Pérez-Reche FJ, Vives E. Finite-size scaling analysis of the avalanches in the three-dimensional Gaussian random-field Ising model with metastable dynamics. *Phys Rev B.* 2003;67(13):134421. doi:10.1103/PhysRevB.67.134421.
28. Sethna JP, Dahmen KA, Perković O. Random-field Ising models of hysteresis edited by Bertotti G and Mayergoyz I. *Sci Hysteres.* 2006;2:107–79.
29. Zapperi S, Cizeau P, Durin G, Stanley HE. Dynamics of a ferromagnetic domain wall: avalanches, depinning transition, and the Barkhausen effect. *Phys Rev B.* 1998;58:6353.
30. Tadić B. Dynamic criticality in driven disordered systems: role of depinning and driving rate in Barkhausen noise. *Phys A: Statist Mech Appl.* 1999;270:125–34.
31. Perković O, Dahmen KA, Sethna JP. Disorder-induced critical phenomena in hysteresis: numerical scaling in three and higher dimensions. *Phys Rev B.* 1999;59:6106.
32. Vives E, Planes A. Hysteresis and avalanches in disordered systems. *J Magnet Magnet Mater.* 2000;221:164–71.
33. Tadić B. Multifractal analysis of Barkhausen noise reveals the dynamic nature of criticality at hysteresis loop. *J Statist Mech.* 2016;6:063305.

34. Belanger DP, Nattermann T. Spin glasses and random fields edited by Young A. P. Series Direct Condens Matter Phys. 1998;12:251–98.
35. Dahmen KA, Sethna JP. Hysteresis loop critical exponents in  $6-\epsilon$  dimensions. Phys Rev Lett. 1993;71:3222. doi:10.1103/PhysRevLett.71.3222.
36. Fytas NG, Martin-Mayor V, Picco M, Surlas N. Phase transitions in disordered systems: The example of the random-field Ising model in four dimensions. Phys Rev Lett. 2016;16:227201.
37. Balog I, Tarjus G, Tissier M. Criticality of the random field Ising model in and out of equilibrium: a nonperturbative functional renormalization group description. Phys Rev B. 2018;97:094204.
38. Cardy J. Random-field effects in site-disordered Ising antiferromagnets. Phys Rev B. 1984;29:505.
39. Fishman S, Aharony A. Random field effects in disordered anisotropic antiferromagnets. J Phys C: Solid State Phys. 1979;12:L729.
40. Joshi DC, Nordblad P, Mathieu R. Random fields and apparent exchange bias in the dilute Ising antiferromagnet  $\text{Fe}_{0.6}\text{Zn}_{0.4}\text{F}_2$ . Sci Rep. 2020;10:14588.
41. Ghara S, Barts E, Vasin K, Kamenskyi D, Prodan L, Tsurkan V, et al. Magnetization reversal through an antiferromagnetic state. Nat Commun. 2023;14:5174.
42. Semenov YG, Wook Kim K. Modeling of antiferromagnetic dynamics: a brief review. IEEE Nanotechnol Mag. 2020;14:32.
43. Chen H, Liu L, Zhou X, Meng Z, Wang X, Duan Z, et al. Emerging antiferromagnets for spintronics. Adv Mater Deerfield. 2024;36:2310379.
44. Khatua J, Pregelj M, Elghandour A, Jagličić Z, Klingeler R, Zorko A, et al. Magnetic properties of the triangular-lattice antiferromagnets  $\text{Ba}_3\text{RB}_9\text{O}_{18}$  ( $R = \text{Yb}, \text{Er}$ ). Phys Rev B. 2022;106:104408.
45. EPJ B. Topical issue: 100 glorious years of the Ising model. Eur Phys J B. 2024.
46. Durin G, Zapperi S. Random-field Ising models of hysteresis. In: Bertotti G, Mayergoyz I, editors. The science of hysteresis, vol. II: physical modeling, micromagnetics, and magnetization dynamics. Amsterdam: Academic Press; 2006. p. 181–267.
47. Hristopoulos DT. Random fields for spatial data modeling—a primer for scientists and engineers. Springer Netherlands: Springer Dordrecht; 2020.
48. Sethna JP, Dahmen KA, Kartha S, Krumhansl JA, Roberts BW, Shore JD. Hysteresis and hierarchies: dynamics of disorder-driven first-order phase transformations. Phys Rev Lett. 1993;70:3347.
49. Uhl JT, Pathak S, Schorlemmer D, Liu X, Swindeman R, Brinkman BAW, et al. Universal quake statistics: from compressed nanocrystals to earthquakes. Sci Rep. 2015;5(1):16493.
50. Omori F. On aftershocks of earthquakes. J Coll Sci Imper Univ Tokyo. 1894;7:111–200.
51. Jagla EA, Landes FP, Rosso A. Viscoelastic effects in avalanche dynamics: a key to earthquake statistics. Phys Rev Lett. 2014;112:174301.
52. Davidsen J, Baiesi M. Self-similar aftershock rates. Phys Rev E. 2016;94(2):022314. doi:10.1103/PhysRevE.94.022314.
53. Bizzarri A, Petri A, Baldassarri A. Earthquake dynamics constrained from laboratory experiments: new insights from granular materials. Ann Geophys. 2021;64(4):SE441. doi:10.4401/ag-8613.
54. Fisher DS. Collective transport in random media: from superconductors to earthquakes. Phys Rep. 1998;301(1–3):113. doi:10.1016/S0370-1573(98)00008-8.
55. Laurson L, Santucci S, Zapperi S. Avalanches and clusters in planar crack front propagation. Phys Rev E. 2010;81(4):046116. doi:10.1103/PhysRevE.81.046116.
56. Baró J, Corral A, Illa X, Planes A, Salje EKH, Schranz W, et al. Statistical similarity between the compression of a porous material and earthquakes. Phys Rev Lett. 2013;110(8):088702. doi:10.1103/PhysRevLett.110.088702.
57. Savolainen J, Laurson L, Alava MJ. Effect of thresholding on avalanches and their clustering for interfaces with long-range elasticity. Phys Rev E. 2022;105:054152.

58. Salje EKH, Jiang X. Crackling noise and avalanches in minerals. *Phys Chem Miner.* 2021;48:22.
59. Lombardi F, Herrmann HJ, Plenz D, de Arcangelis L. Temporal correlations in neuronal avalanche occurrence. *Sci Rep.* 2016;6:24690.
60. Miller SR, Yu S, Plenz D. The scale-invariant, temporal profile of neuronal avalanches in relation to cortical  $\gamma$ -oscillations. *Sci Rep.* 2019;9:16403. doi:10.1038/s41598-019-52326-y.
61. Friedman N, Ito S, Brinkman BAW, Shimono M, DeVille REL, Dahmen KA, et al. Universal critical dynamics in high resolution neuronal avalanche data. *Phys Rev Lett.* 2012;108:208102.
62. Bédard C, Kroger H, Destexhe A. Does the  $1/f$  frequency scaling of brain signals reflect self-organized critical states? *Phys Rev Lett.* 2006;97:118102. doi:10.1103/PhysRevLett.97.118102.
63. Alava MJ, Laurson L, Zapperi S. Crackling noise in plasticity. *Eur Phys J Spec Top.* 2014;223:2353–67.
64. Janičević S, Ovaska M, Alava MJ, Laurson L. Avalanches in 2D dislocation systems without applied stresses. *J Statist Mech.* 2015;2015:P07016.
65. Ispánovity PD, Ugi D, Péterffy G, Knapek M, Kalácska S, Tüzes D, et al. Dislocation avalanches are like earthquakes on the micron scale. *Nat Commun.* 2022;13:1975.
66. Ispánovity PD, Laurson L, Zeiser M, Groma I, Zapperi S, Alava MJ. Avalanches in 2D dislocation systems: plastic yielding is not depinning. *Phys Rev Lett.* 2014;112:235501.
67. Planet R, Santucci S, Zeiser M, Ortín J. Avalanches and non-gaussian fluctuations of the global velocity of imbibition fronts. *Phys Rev Lett.* 2009;102:094502.
68. Nataf GF, Castillo-Villa PO, Baró J, Illa X, Vives E, Planes A, et al. Avalanches in compressed porous SiO<sub>2</sub>-based materials. *Phys Rev E.* 2014;90:022405. doi:10.1103/PhysRevE.90.022405.
69. Mäkinen T, Miksic A, Ovaska MJA. Avalanches in wood compression. *Phys Rev Lett.* 2015;115:055501.
70. Bouchaud JP. Crises and collective socio-economic phenomena: simple models and challenges. *J Statist Phys.* 2013;151:567–606.
71. Pinto OA, Muñoz MA. Quasi-neutral theory of epidemic outbreaks. *PLoS One.* 2011;6:e21946.
72. Mijatović S, Graovac S, Spasojević D, Tadić B. Tuneable hysteresis loop and multifractal oscillations of magnetisation in weakly disordered antiferromagnetic-ferromagnetic bilayers. *Phys E: Low-Dimens Syst Nanostruct.* 2022;142:115319.
73. Chen G, Collette D, Urazhdin S. Experimental demonstration and analysis of random field effects in ferromagnet/antiferromagnet bilayers. *Phys Rev B.* 2020;101:144427.
74. Liu S, Li MR, Zhang SX, Jian SK, Yao H. Universal Kardar-Parisi-Zhang scaling in noisy hybrid quantum circuits. *Phys Rev B.* 2023;107:L201113.
75. Ren J, Li Q, Li W, Cai Z, Wang X. Noise-driven universal dynamics towards an infinite temperature state. *Phys Rev Lett.* 2020;124:130602.
76. King AD, Raymond J, Lanting T, Harris R, Zucca A, Altomare F, et al. Quantum critical dynamics in a 5,000-qubit programmable spin glass. *Nature.* 2023;617:61–6.
77. Živković J, Tadić B. Nanonetworks: the graph theory framework for modeling nanoscale systems. *Nanoscale Syst: Math Model, Theory Appl.* 2013;2:30–48.
78. Tadić B, Melnik R. Fundamental interactions in self-organised critical dynamics on higher order networks. *Eur Phys J B.* 2024;97(6):68. doi:10.1140/epjb/s10051-024-00705-4.
79. Adeyeye AO, Singh N. Large area patterned magnetic nanostructures. *J Phys D: Appl Phys.* 2008;41(15):153001. doi:10.1088/0022-3727/41/15/153001.
80. Li J, Li G, Lu X, Wang S, Leng M, Yang S, et al. Magnetically responsive optical modulation: from anisotropic nanostructures to emerging applications. *Adv Funct Mater.* 2024;34(3):2308293. doi:10.1002/adfm.202308293.
81. Tadić B, Andjelković M, Šuvakov M, Rodgers GJ. Magnetisation processes in geometrically frustrated spin networks with self-assembled cliques. *Entropy.* 2020;22(3):336. doi:10.3390/e22030336.

82. Hang C, Liu W, Dobmann G, Wu Y, Chen W, Wang P. Ising model simulation and empirical research of Barkhausen noise. *J Nondestruct Eval.* 2024;43(1):20. doi:10.1007/s10921-023-01037-6.
83. Mijatović S, Jovković D, Janičević S, Graovac S, Spasojević D. A tool for identifying the criticality in the disordered systems with metastable dynamics. *Phys A: Statist Mech Appl.* 2021;572:125883.
84. Dahmen KA, Sethna JP. Hysteresis, avalanches, and disorder-induced critical scaling: a renormalization-group approach. *Phys Rev B.* 1996;53:14872.
85. Spasojević D, Janičević S, Knežević M. Exact results for mean-field zero-temperature random-field Ising model. *Europhys Lett.* 2006;76:912.
86. Vives E, Rosinberg ML, Tarjus G. Hysteresis and avalanches in the  $T = 0$  random-field Ising model with two-spin-flip dynamics. *Phys Rev B.* 2005;71:134424.
87. Liu Y, Dahmen KA. Random-field Ising model in and out of equilibrium. *Europhys Lett.* 2009;86:56003.
88. Liu Y, Dahmen KA. Unexpected universality in static and dynamic avalanches. *Phys Rev E.* 2009;79(6):061124. doi:10.1103/PhysRevE.79.061124.
89. Spasojević D, Janičević S, Knežević M. Numerical evidence for critical behavior of the two-dimensional nonequilibrium zero-temperature random field Ising model. *Phys Rev Lett.* 2011;106(17):175701. doi:10.1103/PhysRevLett.106.175701.
90. Spasojević D, Janičević S, Knežević M. Avalanche distributions in the two-dimensional nonequilibrium zero-temperature random field Ising model. *Phys Rev E.* 2011;84(5):051119. doi:10.1103/PhysRevE.84.051119.
91. Aizenman M, Wehr J. Rounding of first-order phase transitions in systems with quenched disorder. *Phys Rev Lett.* 1989;62(21):2503. doi:10.1103/PhysRevLett.62.2503.
92. Bricmont J, Kupiainen A. Lower critical dimension for the random-field Ising model. *Phys Rev Lett.* 1987;59(16):1829. doi:10.1103/PhysRevLett.59.1829.
93. Southern BW, Young AP. Real space rescaling study of spin glass behaviour in three dimensions. *J Phys C: Solid State Phys.* 1977;10:2179.
94. Parisi G, Sourlas N. Random magnetic fields, supersymmetry, and negative dimensions. *Phys Rev Lett.* 1979;43:744.
95. Parisi G, Sourlas N. Scale invariance in disordered systems: the example of the random-field Ising model. *Phys Rev Lett.* 2002;89:257204.
96. Tissier M, Tarjus G. Supersymmetry and its spontaneous breaking in the random field Ising model. *Phys Rev Lett.* 2011;107:041601.
97. Fytas NG, Martin-Mayor V. Universality in the three-dimensional random-field Ising model. *Phys Rev Lett.* 2013;110:227201.
98. Fytas NG, Martin-Mayor V, Picco M, Sourlas N. Restoration of dimensional reduction in the random-field Ising model at five dimensions. *Phys Rev E.* 2017;95:042117.
99. Fytas NG, Martin-Mayor V, Parisi G, Picco M, Sourlas N. Evidence for supersymmetry in the random-field Ising model at  $d = 5$ . *Phys Rev Lett.* 2019;122:240603.
100. Janičević S, Mijatović S, Spasojević D. Critical behavior of the two-dimensional nonequilibrium zero-temperature random field Ising model on a triangular lattice. *Phys Rev E.* 2017;95:042131.
101. Tadić B. Dynamical implications of sample shape for avalanches in 2-dimensional random-field Ising model with saw-tooth domain wall. *Phys A: Statist Mech Appl.* 2018;493:330–41.
102. Kurbah L, Thongjaomayum D, Shukla P. Nonequilibrium random-field Ising model on a diluted triangular lattice. *Phys Rev E.* 2015;91:012131.
103. Mijatović S, Jovković D, Spasojević D. Nonequilibrium athermal random-field Ising model on hexagonal lattices. *Phys Rev E.* 2021;103:032147.
104. Chen YJ, Papanikolaou S, Sethna JP, Zapperi S, Durin G. Avalanche spatial structure and multivariable scaling functions: sizes, heights, widths, and views through windows. *Phys Rev E.* 2011;84:061103.

105. Brinkman BAW, Dahmen KA. Tuning coupling: discrete changes in runaway avalanche sizes in disordered media. *Phys Rev E*. 2011;84:041129.
106. Pérez-Reche FJ, Vives E. Spanning avalanches in the three-dimensional Gaussian random-field Ising model with metastable dynamics: field dependence and geometrical properties. *Phys Rev B*. 2004;70:214422.
107. Spasojević D, Janičević S, Knežević M. Analysis of spanning avalanches in the two-dimensional nonequilibrium zero-temperature random-field Ising model. *Phys Rev E*. 2014;89:012118.
108. Janičević S, Knežević D, Mijatović S, Spasojević D. Scaling domains in the nonequilibrium athermal random field Ising model of finite systems. *J Statist Mech*. 2021;2021(1):013202. doi:10.1088/1742-5468/abcd32.
109. Navas-Portella V, Vives E. Influence of the aspect ratio and boundary conditions on universal finite-size scaling functions in the athermal metastable two-dimensional random field Ising model. *Phys Rev E*. 2016;93(2):022129. doi:10.1103/PhysRevE.93.022129.
110. Spasojević D, Mijatović S, Navas-Portella V, Vives E. Crossover from three-dimensional to two-dimensional systems in the nonequilibrium zero-temperature random-field Ising model. *Phys Rev E*. 2018;97(1):012109. doi:10.1103/PhysRevE.97.012109.
111. Tadić B, Mijatović S, Janičević S, Spasojević D, Rodgers GJ. The critical Barkhausen avalanches in thin random-field ferromagnets with an open boundary. *Sci Rep*. 2019;9(1):6349. doi:10.1038/s41598-019-42802-w.
112. Mijatović S, Jovković D, Janičević S, Spasojević D. Critical disorder and critical magnetic field of the nonequilibrium athermal random-field Ising model in thin systems. *Phys Rev E*. 2019;100(3):032113. doi:10.1103/PhysRevE.100.032113.
113. Laurson L, Durin G, Zapperi S. Universality classes and crossover scaling of Barkhausen noise in thin films. *Phys Rev B*. 2014;89(10):104402. doi:10.1103/PhysRevB.89.104402.
114. Bohn F, Durin G, Correa MA, Machado NR, Della Pace RD, Chesman C, et al. Playing with universality classes of Barkhausen avalanches. *Sci Rep*. 2018;8(1):11294. doi:10.1038/s41598-018-29576-3.
115. Dhar D, Shukla P, Sethna JP. Zero-temperature hysteresis in the random-field Ising model on a Bethe lattice. *J Phys A: Mathemat Gen*. 1997;30(15):5259. doi:10.1088/0305-4470/30/15/013.
116. Tadić B, Malarz K, Kułakowski K. Magnetization reversal in spin patterns with complex geometry. *Phys Rev Lett*. 2005;94(13):137204. doi:10.1103/PhysRevLett.94.137204.
117. Kim DH, Rodgers GJ, Kahng B, Kim D. Spin-glass phase transition on scale-free networks. *Phys Rev E*. 2005;71(5):056115. doi:10.1103/PhysRevE.71.056115.
118. Dorogovtsev SN, Goltsev AV, Mendes JFF. Critical phenomena in complex networks. *Rev Mod Phys*. 2008;80(4):1275. doi:10.1103/RevModPhys.80.1275.
119. Puppini E. Statistical properties of Barkhausen noise in Thin Fe films. *Phys Rev Lett*. 2000;84(23):5415. doi:10.1103/PhysRevLett.84.5415.
120. Shin SC, Ryu KS, Kim DH, Akinaga H. Two-dimensional critical scaling behavior of Barkhausen avalanches. *J Appl Phys*. 2008;103(7):07D907. doi:10.1063/1.2830967.
121. Merazzo K, Leitao D, Jiménez E, Araujo J, Camarero J, del Real RP, et al. Geometry-dependent magnetization reversal mechanism in ordered Py antidot arrays. *J Phys D: Appl Phys*. 2011;44(50):505001. doi:10.1088/0022-3727/44/50/505001.
122. Lee HS, Ryu KS, You CY, Jeon KR, Yang SY, Parkin SSP, et al. Asymmetric magnetic disorder observed in thermally activated magnetization reversal of exchange-biased IrMn/CoFe films. *J Magn Magn Mater*. 2013;325:13. doi:10.1016/j.jmmm.2012.07.038.
123. Parkin SSP, Hayashi M, Thomas L. Magnetic domain-wall racetrack memory. *Science*. 2008;320:190.
124. McGilly IJ, Yudin P, Feigl I, Tagantsev AK, Setter N. Controlling domain wall motion in ferroelectric thin films. *Nat Nanotechnol*. 2015;10:145.

125. Savel'ev S, Rakhmanov A, Nori F. Experimentally realizable devices for domain wall motion control. *New J Phys.* 2005;7:82.
126. Garg C, Yang SH, Phung T, Pushp A, Parkin S. Dramatic influence of curvature of nanowire on chiral domain wall velocity. *Sci Adv.* 2017;3:e1602804.
127. Lee HS, Ryu KS, Kang IS, Shin SC. Universal Barkhausen critical scaling behavior observed in  $Ni_xFe_{1-x}$  ( $x = 0 - 0.5$ ) films. *J Appl Phys.* 2011;109:07E101.
128. Berger A, Inomata A, Jiang JS, Pearson JE, Bader SD. Experimental observation of disorder-driven hysteresis-loop criticality. *Phys Rev Lett.* 2000;85(19):4176. doi:10.1103/PhysRevLett.85.4176.
129. Yang S, Erskine JL. Domain wall dynamics and Barkhausen jumps in thin-film permalloy microstructures. *Phys Rev B.* 2005;72(6):064433. doi:10.1103/PhysRevB.72.064433.
130. Radić S, Janičević S, Jovković D, Spasojević D. The effect of finite driving rate on avalanche distributions. *J Statist Mech.* 2021;2021(9):093301. doi:10.1088/1742-5468/ac1f12.
131. Mijatović S, Branković M, Graovac S, Spasojević D. Avalanche properties in striplike ferromagnetic systems. *Phys Rev E.* 2020;102(2):022124. doi:10.1103/PhysRevE.102.022124.
132. Skaugen A, Laurson L. Depinning exponents of thin film domain walls depend on disorder strength. *Phys Rev Lett.* 2022;128(9):097202. doi:10.1103/PhysRevLett.128.097202.
133. Durin G, Zapperi S. Scaling exponents for barkhausen avalanches in polycrystalline and amorphous ferromagnets. *Phys Rev Lett.* 2000;84(20):4705. doi:10.1103/PhysRevLett.84.4705.
134. Shukla P, Thongjaomayum D. Hysteresis in random-field Ising model on a Bethe lattice with a mixed coordination number. *J Phys A: Math Theor.* 2016;49(23):235001. doi:10.1088/1751-8113/49/23/235001.
135. Thongjaomayum D, Shukla P. Non-mean-field behavior of critical wetting transition for short-range forces. *Phys Rev E.* 2013;88(4):042138. doi:10.1103/PhysRevE.88.042138.
136. Thongjaomayum D, Shukla P. Critical hysteresis on dilute triangular lattice. *Phys Rev E.* 2019;99(6):062136. doi:10.1103/PhysRevE.99.062136.
137. de Sousa IP, dos Santos Lima GZ, Correa MA, Sommer RL, Corso G, Bohn F. Waiting-time statistics in magnetic systems. *Sci Rep.* 2020;10(1):9692. doi:10.1038/s41598-020-66727-x.
138. Laurson L, Illa X, Alava MJ. The effect of thresholding on temporal avalanche statistics. *J Statist Mech.* 2009;2009(1):P01019. doi:10.1088/1742-5468/2009/01/P01019.
139. Font-Clos F, Pruessner G, Moloney NR, Deluca A. The perils of thresholding. *New J Phys.* 2015;17(4):043066. doi:10.1088/1367-2630/17/4/043066.
140. Janičević S, Jovković D, Laurson L, Spasojević D. Threshold-induced correlations in the Random Field Ising Model. *Sci Rep.* 2018;8(1):2571. doi:10.1038/s41598-018-20759-6.
141. Jovković D, Janičević S, Mijatović S, Laurson L, Spasojević D. Effects of external noise on threshold-induced correlations in ferromagnetic systems. *Phys Rev E.* 2021;103(6):062114. doi:10.1103/PhysRevE.103.062114.
142. Barés J, Bonamy D, Rosso A. Seismiclike organization of avalanches in a driven long-range elastic string as a paradigm of brittle cracks. *Phys Rev E.* 2019;100(2):023001. doi:10.1103/PhysRevE.100.023001.
143. Janičević S, Laurson L, Måløy KJ, Santucci S, Alava MJ. Interevent correlations from avalanches hiding below the detection threshold. *Phys Rev Lett.* 2016;117:230601.
144. Janičević S, Laurson L, Måløy KJ, Santucci S, Alava MJ, Janičević, et al. Reply. *Phys Rev Lett.* 2017;119:188901.
145. Post RAJ, Michels MAJ, Ampuero JP, Candela T, Fokker PA, van Wees JD, et al. Interevent-time distribution and aftershock frequency in non-stationary induced seismicity. *Sci Rep.* 2021;11:1–10.
146. Radiguet M, Perfettini H, Cotte N, Gualandi A, Valette B, Kostoglodov V, et al. Triggering of the 2014  $M_w$ 7.3 Papanoa earthquake by a slow slip event in Guerrero, Mexico. *Nat Geosci.* 2016;9:829–33. doi:10.1038/ngeo2817.

147. Spasojević D, Graovac S, Janičević S. Interplay of disorder and type of driving in disordered ferromagnetic systems. *Phys Rev E*. 2022;106:044107.
148. Spasojević D, Radić S, Jovković D, Janičević S. Spin activity correlations in driven disordered systems. *J Statist Mech*. 2022;2022(6):063302. doi:10.1088/1742-5468/ac72a2.
149. Spasojević D, Janičević S. Two-dimensional ferromagnetic systems with finite driving. *Chaos Solit Fract*. 2022;158:112033. doi:10.1016/j.chaos.2022.112033.
150. White RA, Dahmen KA. Driving rate effects on crackling noise. *Phys Rev Lett*. 2003;91(8):085702. doi:10.1103/PhysRevLett.91.085702.
151. Travesset A, White RA, Dahmen KA. Crackling noise, power spectra, and disorder-induced critical scaling. *Phys Rev B*. 2002;66(2):024430. doi:10.1103/PhysRevB.66.024430.
152. Perez-Reche F, Tadić B, Manosa L, Planes A, Vives E. Driving rate effects in avalanche-mediated first-order phase transitions. *Phys Rev Lett*. 2004;93(19):195701. doi:10.1103/PhysRevLett.93.195701.
153. de Queiroz SLA, Bahiana M. Finite driving rates in interface models of Barkhausen noise. *Phys Rev E*. 2001;64(6):066127. doi:10.1103/PhysRevE.64.066127.
154. Hoffman GR, Turner JA. Variation of coercivity of magnetic materials with driving field. *J Appl Phys*. 1963;34(9):2708. doi:10.1063/1.1729796.
155. Moore TA, Bland JAC. Mesofrequency dynamic hysteresis in thin ferromagnetic films. *J Phys: Condens Matt*. 2004;16(46):R1369. doi:10.1088/0953-8984/16/46/R03.
156. Ruiz-Feal I, Moore TA, Lopez-Diaz L, Bland JAC. Model for reversal dynamics of ultrathin ferromagnetic films. *Phys Rev B*. 2002;65(5):054409. doi:10.1103/PhysRevB.65.054409.
157. Barés J, Dubois A, Hattali L, Dalmas D, Bonamy D. Aftershock sequences and seismic-like organization of acoustic events produced by a single propagating crack. *Nat Commun*. 2018;9:1253.
158. Stojanova M, Santucci S, Vanel L, Ramos O. High frequency monitoring reveals aftershocks in subcritical crack growth. *Phys Rev Lett*. 2014;112(11):115502. doi:10.1103/PhysRevLett.112.115502.
159. Ribeiro HV, Costa LS, Alves LGA, Santoro PA, Picoli S, Lenzi EK, et al. Analogies between the cracking noise of ethanol-dampened charcoal and earthquakes. *Phys Rev Lett*. 2015;115(2):025503. doi:10.1103/PhysRevLett.115.025503.
160. Piegari E, Cataudella V, Di Maio R, Milano L, Nicodemi M. Finite driving rate and anisotropy effects in landslide modeling. *Phys Rev E*. 2006;73(2):026123. doi:10.1103/PhysRevE.73.026123.
161. Kun F, Varga I, Lennartz-Sassinek S, Main IG. Rupture cascades in a discrete element model of a porous sedimentary rock. *Phys Rev Lett*. 2014;112(6):065501. doi:10.1103/PhysRevLett.112.065501.
162. Sultan NH, Karimi K, Davidsen J. Sheared granular matter and the empirical relations of seismicity. *Phys Rev E*. 2022;105(2):024901. doi:10.1103/PhysRevE.105.024901.
163. Girard L, Weiss J, Amitrano D. Damage-cluster distributions and size effect on strength in compressive failure. *Phys Rev Lett*. 2012;108:225502.
164. Spasojević D, Janičević S, Tadić B. Hysteresis-loop phenomena in disordered ferromagnets with demagnetizing field and finite temperature. *Phys Rev E*. 2024;110:014133.
165. Spasojević D, Janičević S. The impact of crystal grain size on the behavior of disordered ferromagnetic systems: from thin to bulk geometry. *J Statist Mech*. 2024;8:083303.
166. Yao L, Jack RL. Thermal vestiges of avalanches in the driven random field Ising model. *J Statist Mech*. 2023;2:023303.
167. Kuntz MC, Sethna JP. Noise in disordered systems: the power spectrum and dynamic exponents in avalanche models. *Phys Rev B*. 2000;62:11699.
168. Spasojević D, Marinković M, Jovković D, Janičević S, Laurson L, Djordjević A. Barkhausen noise in disordered strip-like ferromagnets: experiment versus simulations. *Phys Rev E*. 2024;109(2):024110. doi:10.1103/PhysRevE.109.024110.

169. Kuntz M, Perković O, Dahmen KA, Roberts BW, Sethna JP. Hysteresis, avalanches, and noise. *Comput Sci Eng.* 1999;1(4):73. doi:10.1109/5992.774844.
170. Perković O, Dahmen K, Sethna JP. Barkhausen noise, and plain old criticality. *Phys Rev Lett.* 1995;75(24):4528. doi:10.1103/PhysRevLett.75.4528.
171. Spasojević D, Mijatović S, Janičević S. Dimensional crossover in driving-rate induced criticality on the hysteresis-loop of disordered ferromagnetic systems. *J Statist Mech.* 2023;2023(3):033210. doi:10.1088/1742-5468/acc4b0.
172. Janičević S, Mijatović S, Spasojević D. Finite driving rate effects in the nonequilibrium athermal random field Ising model of thin systems. *Phys A: Statist Mech Appl.* 2023;614(3):128553. doi:10.1016/j.physa.2023.128553.
173. Graovac S, Mijatović S, Spasojević D. Mechanism of subcritical avalanche propagation in three-dimensional disordered systems. *Phys Rev E.* 2021;103:062123.
174. Mermin ND, H. W. Absence of ferromagnetism or antiferromagnetism in one- or two-dimensional isotropic Heisenberg models. *Phys Rev Lett.* 1966;17:1133.
175. Kennedy T, Nachtergaele B. The heisenberg model—a bibliography. 1995. Available from: <https://www.math.ucdavis.edu/bxn/qshtml>. [Accessed 2024].
176. Aizenman M, Wehr J. Rounding of first-order phase transitions in systems with quenched disorder. *Commun Math Phys.* 1990;130:3.
177. Maritan A, Cieplak M, Swift MR, Banavar JR. Spin-flip avalanches and dynamics of first order phase transitions. *Phys Rev Lett.* 1994;72:946.
178. Frontera C, Vives E. Numerical signs for a transition in the two-dimensional random field Ising model at  $T = 0$ . *Phys Rev E.* 1999;59:R1295.
179. Frontera C, Vives E. Studying avalanches in the ground state of the two-dimensional random-field Ising model driven by an external field. *Phys Rev E.* 2000;62(5):7470. doi:10.1103/PhysRevE.62.7470.
180. Hartmann AK. Critical exponents of four-dimensional random-field Ising systems. *Phys Rev B.* 2002;65(17):174427. doi:10.1103/PhysRevB.65.174427.
181. Ahrens B, Hartmann AK. Critical behavior of the random-field Ising model at and beyond the upper critical dimension. *Phys Rev B.* 2011;83(1):014205. doi:10.1103/PhysRevB.83.014205.
182. Fytas NG, Martín-Mayor V, Parisi G, Picco M, Sourlas N. Finite-size scaling of the random-field Ising model above the upper critical dimension. *Phys Rev E.* 2023;108(4):044146. doi:10.1103/PhysRevE.108.044146.
183. Seppälä ET, Petäjä V, Alava MJ. Disorder, order, and domain wall roughening in the two-dimensional random field Ising model. *Phys Rev E.* 1998;58(5):R5217. doi:10.1103/PhysRevE.58.R5217.
184. Gong C, Li L, Li Z, Ji H, Stern A, Xia Y, et al. Discovery of intrinsic ferromagnetism in two-dimensional van der Waals crystals. *Nature.* 2017;546:265–9.
185. Huang B, Clark G, Navarro-Moratalla E, Klein DR, Cheng R, Seyler KL, et al. Layer-dependent ferromagnetism in a van der Waals crystal down to the monolayer limit. *Nature.* 2017;546:270–3.
186. Dahmen KA, Sethna JP. Disorder-induced critical phenomena in hysteresis: a numerical scaling analysis. *arXiv:condmat/9609072v1.* 1996.
187. Press WH, Teukolsky SA, Vetterling WT, Flannery BP. *Numerical recipes: the art of scientific computing.* 3rd ed. Cambridge: Cambridge University Press; 2007.
188. Huang F, Kief MT, Mankey GJ, Willis RF. Magnetism in the few-monolayers limit: a surface magneto-optic Kerr-effect study of the magnetic behavior of ultrathin films of Co, Ni, and Co-Ni alloys on Cu(100) and Cu(111). *Phys Rev B.* 1994;49:3962.
189. Liu LL, Stanley HE. Some results concerning the crossover behavior of quasi-two-dimensional and quasi-one-dimensional systems. *Phys Rev Lett.* 1972;29:927.

190. Kaneda K, Okabe Y, Kikuchi M. Shape effects of finite-size scaling functions for anisotropic three-dimensional Ising models. *J Phys A: Mathemat Gen.* 1999;32:7263.
191. Lee KW. Dimensional crossover in the anisotropic 3D Ising model: a Monte Carlo study. *J Korean Phys Soc.* 2002;40:L398.
192. Lee KW, Lee CE. Size-driven dimensional crossover in the quasi-one-dimensional Heisenberg model. *Phys Rev B.* 2004;69:094428.
193. Laurson L, Illa X, Santucci S, Tallakstad KT, Måløy KJ, Alava MJ. Evolution of the average avalanche shape with the universality class. *Nat Commun.* 2013;4:2927.
194. Binder K. Monte Carlo study of thin magnetic Ising films. *Thin Solid Films.* 1974;20:367.
195. Laosiritaworn Y, Poulter J, Staunton JB. Magnetic properties of Ising thin films with cubic lattices. *Phys Rev B.* 2004;70:104413.
196. Spasojević D, Janičević S. Disordered ferromagnetic systems with stochastic driving. *Chaos, Solit Fract.* 2023;169:113327.
197. Tadić B, Melnik R. Self-organised critical dynamics as a key to fundamental features of complexity in physical, biological, and social networks. *Dynamics.* 2021;1:181–97.
198. Pérez-Reche FJ, Truskinovsky L, Zanzotto G. Driving-induced crossover: from classical criticality to self-organized criticality. *Phys Rev Lett.* 2008;101:230601.
199. Pázmándi F, Zaránd G, Zimányi GT. Self-organized criticality in the hysteresis of the sherrington-kirkpatrick model. *Phys Rev Lett.* 1999;83:1034–7.
200. Knuth DE. *The art of computer programming, volume II: seminumerical Algorithms.* 3rd Edition. Massachusetts: Addison-Wesley, 1998.
201. Benassi A, Zapperi S. Barkhausen instabilities from labyrinthine magnetic domains. *Phys Rev B.* 2011;84:214441.
202. Pavlos GP, Karakatsanis LP, Xenakis MN, Pavlos EG, Iliopoulos AC, Sarafopoulos DV. Universality of non-extensive Tsallis statistics and time series analysis: theory and applications. *Phys A: Statist Mech Appl.* 2014;395:58–95.
203. Kaappa S, Laurson L. Barkhausen noise from formation of 360° domain walls in disordered permalloy thin films. *Phys Rev Res.* 2023;5:L022006.
204. Pavlov AN, Anishchenko VS. Multifractal analysis of complex signals. *Phys Uspekhi.* 2007;50:819–34.
205. Kantelhardt JW, Zschiegner SA, Koscielny-Bunde E, Havlin S, Bunde A, Stanley HE. Multifractal detrended fluctuation analysis of nonstationary time series. *Phys A Stat Mech Appl.* 2002;316:87–114.
206. Gell-Mann M, Tsallis C. *Nonextensive entropy: interdisciplinary applications.* New York: Oxford University Press; 2004.
207. Rodríguez A, Pluchino A, Tirnakli U, Rapisarda A, Tsallis C. Nonextensive footprints in dissipative and conservative dynamical system. *Symmetry.* 2023;15(2):444.
208. Yüksel Y. Dynamic phase transition properties and metamagnetic anomalies of kinetic Ising model in the presence of additive white noise. *Phys A: Statist Mech Appl.* 2021;580:126172. doi:10.1016/j.physa.2021.126172.